

POTENTIAL SINGULARITY FORMATION OF 3D AXISYMMETRIC NAVIER–STOKES EQUATIONS WITH DEGENERATE VARIABLE DIFFUSION COEFFICIENTS

THOMAS Y. HOU AND DE HUANG

ABSTRACT. In this paper, we present strong numerical evidences that the 3D axisymmetric Navier–Stokes equations with degenerate variable diffusion coefficients and smooth initial data of finite energy develop a potential finite time locally self-similar singularity at the origin. An important feature of this potential singularity is that the solution develops a two-scale traveling wave that travels towards the origin. The two-scale feature is characterized by the property that the center of the traveling wave approaches to the origin at a slower rate than the rate of the collapse of the singularity. The driving mechanism for this potential singularity is due to two antisymmetric vortex dipoles that generate a strong shearing layer in both the radial and axial velocity fields, which transport the solution first towards $z = 0$ and then towards the symmetry axis $r = 0$. The initial condition is designed in such a way that it generates a positive feedback loop that enforces a strong nonlinear alignment of vortex stretching, leading to a stable locally self-similar blowup at the origin. We perform careful resolution study and asymptotic scaling analysis to provide further support of the potential finite time locally self-similar blowup.

1. INTRODUCTION

The three-dimensional (3D) incompressible Navier–Stokes equations in fluid dynamics describe the motion of viscous incompressible flows. It has been used to model ocean currents, weather patterns, and other fluids related phenomena. Despite their wide range of applications, the question regarding the global regularity of the 3D Navier–Stokes equations with smooth initial data of finite energy has remained open and is one of the seven Millennium Problems posted by the Clay Mathematics Institute [Fef06]. The main difficulty associated with the global regularity of the 3D Navier–Stokes equations is the presence of vortex stretching, which is absent in the corresponding 2D problem. A closely related problem is the global regularity of the 3D incompressible Euler equations [MB02]. In 2014, Luo and Hou [LH14a, LH14b] presented strong numerical evidences that the 3D axisymmetric Euler equations with smooth initial data and boundary develop potential finite time singular solutions at the boundary. The presence of the boundary, the sign conditions and the symmetry properties of the initial data seem to play a crucial role in generating a sustainable finite time singularity of the 3D Euler equations.

1.1. The setup of the problem. In this paper, we study the potential singularity formation of the 3D incompressible axisymmetric Navier–Stokes equations with smooth degenerate variable diffusion coefficients and smooth initial data of finite energy. The physical domain is a periodic cylinder as in [LH14a, LH14b]. We impose a no-slip and no-flow boundary condition at $r = 1$ and a periodic boundary condition in the axial variable z . Unlike the Hou–Luo blowup scenario for the axisymmetric Euler equations, the potential singularity that we consider for the Navier–Stokes equations with variable diffusion coefficients occurs at the origin along the symmetry axis $r = 0$. The boundary at $r = 1$ does not play an essential role in generating this potential locally self-similar singularity.

Let u^θ , ω^θ , and ψ^θ be the angular components of the velocity, the vorticity, and the vector stream function, respectively. According to [LWo6], u^θ , ω^θ , and ψ^θ must be an odd function of r if the solution of the Navier–Stokes equations is smooth. In [HLo8a], Hou and Li introduced the variables

$$u_1 = u^\theta/r, \quad \omega_1 = \omega^\theta/r, \quad \psi_1 = \psi^\theta/r,$$

and transformed the Navier–Stokes equations into the form

$$u_{1,t} + u^r u_{1,r} + u^z u_{1,z} = 2u_1 \psi_{1,z} + f_{u_1}, \quad (1.1a)$$

$$\omega_{1,t} + u^r \omega_{1,r} + u^z \omega_{1,z} = 2u_1 u_{1,z} + f_{\omega_1}, \quad (1.1b)$$

$$-\left(\partial_r^2 + \frac{3}{r}\partial_r + \partial_z^2\right)\psi_1 = \omega_1, \quad (1.1c)$$

where $u^r = -r\psi_{1,z}$, $u^z = 2\psi_1 + r\psi_{1,r}$, the diffusion terms f_{u_1}, f_{ω_1} are defined in (2.4). We choose the axisymmetric variable diffusion coefficients to be the sum of a space-dependent part and a time-dependent part. The space-dependent parts of the viscosity are very small (below 10^{-7}) on the whole domain and of order $O(r^2) + O(z^2)$ for $r \leq 10^{-4}$ and $|z| \leq 10^{-5}$. The time-dependent part of the viscosity is equal to $0.025/\|\omega^\theta\|_{L^\infty}$ and below 4×10^{-7} initially. It is introduced to regularize the sharp fronts in the early stage of the computation. Since $\|\omega^\theta\|_{L^\infty}$ grows rapidly in time, the time dependent part of the viscosity decreases rapidly in time and becomes negligibly small within a short time.

The initial condition that we construct analytically is inspired by our computational experiments performed earlier. It has several important features. The first one is that u_1 , ω_1 and ψ_1 are odd functions of z and even in r . Secondly, the maximum location of ω_1 for $z > 0$ is slightly below the maximum location of u_1 where $u_{1,z}$ is large and has a proper sign. Thirdly, the angular vorticity generates two antisymmetric (with respect to z) vortex dipoles. The antisymmetric vortex dipoles induce a strong shear layer for the axial and radial velocities that first transport the solution towards $z = 0$ rapidly, then pushes solution towards $r = 0$, leading to a potential singularity at the origin.

1.2. Major features of the potential blowup and the blowup mechanism. One of the important features of the potential blowup solution is that it develops a two-scale traveling solution approaching the origin. The two-scale traveling wave solution is characterized by the property that the center of the traveling wave, located at $(R(t), Z(t))$ with $R(t) = O((T - t)^{1/2})$, approaches to the origin at a slower rate than the rate of the collapse of the singularity, which is $Z(t) = O(T - t)$. Another important feature is that the odd symmetry (in z) of the initial data of ω_1 constitutes to a dipole structure of the angular vorticity ω^θ , which then induces an antisymmetric local convective circulation. This convective circulation is the cornerstone of our blowup scenario, as it has the desirable property of pushing the solution near $z = 0$ towards the symmetry axis $r = 0$.

An important guiding principle for constructing our initial data is to enforce a strong nonlinear alignment of vortex stretching. First of all, the vortex dipoles induce a negative radial velocity near $z = 0$, i.e. $u^r = -r\psi_{1,z} < 0$, which implies $\psi_{1,z} > 0$. Moreover, $\psi_{1,z}(R(t), z, t)$ is a monotonically decreasing function of z and is relatively flat near $z = 0$. Through the vortex stretching term $2\psi_{1,z}u_1$ in (1.1a), the large value of $\psi_{1,z}$ near $z = 0$ induces a traveling wave for u_1 that approaches $z = 0$ rapidly. The strong nonlinear alignment in vortex stretching overcomes the stabilizing effect of advection in the upward z direction (see e.g. [HLo8a, HLo9]). The oddness of u_1 in z then generates a large positive gradient $u_{1,z}$, which contributes positively to the rapidly growth of ω_1 through the vortex stretching term $2u_1 u_{1,z}$ in (1.1b). The rapid growth of ω_1 in turn feeds back to the rapid growth of $\psi_{1,z}$. The whole coupling mechanism described above forms a positive feedback loop.

Moreover, we observe that the 2D velocity field $(u^r(t), u^z(t))$ in the rz -plane forms a closed circle right above $(R(t), Z(t))$. The corresponding streamline is then trapped in the circle region in the rz -plane. This local circle structure of the 2D velocity field is critical in stabilizing the blowup process, as it keeps the main parts of the u_1, ω_1 profiles traveling towards the origin instead of being pushed upward. The strong shear layer in u^r and u^z generates a sharp front for u_1 in both r and z directions.

1.3. The dynamic formation of a vacuum region and a tornado singularity. Another important feature of our initial data is that it generates a local hyperbolic flow in the rz -plane (note that the 2D velocity field (u^r, u^θ) can be extended to the negative r plane as an even function of r). One the one

hand, this hyperbolic flow generates a strong negative radial velocity field that pushes the flow to travel towards $r = 0$ in the region near $z = 0$. On the other hand, as the flow gets very close to $r = 0$, the strong upward axial velocity u^z near $r = 0$ transports u_1 from the region near $z = 0$ upward along the z direction. Due to the odd symmetry of u_1 , u_1 is almost zero in the region near $z = 0$. As a result, the flow dynamically develops a vacuum region between the sharp front of u_1 and the symmetry axis $r = 0$. The boundary of the vacuum region also plays the role of a “moving boundary” for the flow.

The vacuum region separates the flow into a local “two-phase” flow and the “moving boundary” plays the role of a “free interface”. To gain further insight, we focus our attention near the center of the traveling wave, which is asymptotically far from the symmetry axis $r = 0$ since $R(t)/Z(t) \rightarrow \infty$ as $t \rightarrow T$. Thus we may approximate the 3D Navier–Stokes equations by the 2D Boussinesq equations in the rz -plane by treating u_1 as the density. Since u_1 experiences a big jump from almost zero to a large value across the “free interface”, we may formally treat the flow as a “two-phase” flow locally. We also observe that ω_1 behaves like a regularized 1D delta function supported along the “free interface”. This is another indication that the solution dynamically develops into a “two-phase” flow locally.

Within the vacuum region, the angular velocity $u^\theta = ru_1$ is almost zero, which implies that there is almost no spinning around the symmetry axis. The flow effectively travels upward along the vertical direction inside the vacuum region. Thus, the vacuum region resembles the calm eye of a tornado. Across the “moving boundary”, u_1 becomes very large and grows rapidly in time. As a result, the flow spins rapidly around the symmetry axis. Moreover, the streamlines induced by the velocity field travel upward along the vertical direction and then move outward along the radial direction. The local blowup solution resembles the structure of a tornado. For this reason, we also call the potential singularity of the Navier–Stokes equations with variable diffusion coefficients “a tornado singularity”.

We remark that although u_1 and ω_1 develop sharp fronts in the r direction and large gradients in the z direction and ω_1 develops a thin structure, they are actually isotropic with respect to the rescaled coordinates: $\eta = (r - R(t))/Z(t)$ and $\xi = z/Z(t)$. Moreover, u_1 and ω_1 develop a locally self-similar profile thanks to the regularizing effect of the degenerate variable diffusion coefficients.

1.4. Computational challenges. The two-scale nature of the potential singular solution presents considerable challenges in obtaining a well-resolved numerical solution for the Navier–Stokes equations with variable diffusion coefficients. To resolve this potential two-scale singular solution, we design an adaptive mesh by constructing two adaptive mesh maps for r and z explicitly. More specifically, we construct our mapping densities in the near field (phase 1: resolving the $Z(t)$ scale), the intermediate field (phase 2: resolving the $R(t)$ scale), and the far field (phase 3: resolving the $O(1)$ scale) with a transition phase in between. We then allocate a fixed number of grid points in each phase and update the mesh maps dynamically according to some criteria. This adaptive mesh strategy achieves a highly adaptive mesh with the smallest mesh size of order $O(10^{-10})$.

Another difficulty is that the strong shearing flow near “moving boundary” generates vortex shedding that propagates downstream. At a result, the solution generates some mild oscillations in the tail region. These mild oscillations have only very weak coupling to the solution in the most singular region and do not affect the driving mechanism for the potential finite time blowup. On the other hand, since we place a significant number of grid points in the most singular region, we have a relatively small number of grid points in the tail region. If we do not control these oscillations, it could affect the nonlinear alignment of vortex stretching in the most singular region. To alleviate this difficulty, we design a second order filtering scheme to control these oscillations in the tail region. We will demonstrate that this filtering scheme is very effective in controlling the oscillations in the tail region and the potential singular solution seems insensitive to the way we perform this filtering.

We use a second order finite difference method to discretize the spatial derivatives, and a second order explicit Runge–Kutta method to discretize in time. We adopt the second order B-spline based Galerkin method developed in [LH14a, LH14b] to solve the Poisson equation for the stream function.

The overall method is second order accurate. We have performed careful resolution study which confirms that our method indeed gives second order accuracy in the maximum norm.

1.5. Asymptotic scaling analysis. To confirm that the potential singular solution develops a locally self-similar blowup, we perform numerical fitting of the growth rates for several physical quantities. Our study shows that the maximum of the vorticity vector grows like $O((T-t)^{-3/2})$, and $R(t) = O(T-t)^{1/2}$, $Z(t) = O(T-t)$. The fact that $\|\nabla \mathbf{u}\|_{L^\infty} \geq \|\nabla \boldsymbol{\omega}\|_{L^\infty} \geq C_0(T-t)^{-3/2}$ gives that $\int_0^T \|\nabla \mathbf{u}(t)\|_{L^\infty} dt = \infty$, which implies that the solution could potentially develop a finite time singularity [MB02].

We have also performed an asymptotic scaling analysis to study the scaling properties of potential locally self-similar blowup solution. By balancing the scales in various terms, we show that u_1 and $\psi_{1,z}$ must blow up with the rate $O(1/(T-t))$ if there is a locally self-similar blowup. Due to the conservation of total circulation $\Gamma = r^2 u_1$ and the degeneracy of the diffusion coefficients, we show that Γ remains $O(1)$ at $(R(t), Z(t))$. This property and the scaling property that $u_1 = O(1/(T-t))$ imply that $R(t) = O((T-t)^{1/2})$. Moreover, the balance between the vortex stretching term and the degenerate diffusion term suggests that $Z(t) = O(T-t)$. Similarly, we can show that ω_1 blows up like $O(1/(T-t)^2)$. In terms of the original physical variables, the vorticity vector blows up like $O(1/(T-t)^{3/2})$ and the velocity field blows up like $O(1/(T-t)^{1/2})$. The results obtained by our scaling analysis are consistent with our numerical fitting of the blowup rates for various quantities.

The two-scale traveling wave introduces an additional large advection term due to the fact that $R(t)$ approaches to zero at a slower rate than $Z(t)$. This large advection term enforces an interfacial condition that the velocity field should be tangent to the “moving boundary” locally. Our asymptotic scaling analysis also reveals that there are two hyperbolic points in the rescaled radial velocity; the left one is a compression point, while the right one is a rarefaction point. The compression point induces a shock like profile which explains why u_1 develops a sharp front to the left of its maximum location in the r direction. The rarefaction point induces a rarefaction wave, which explains why the local profile of u_1 is relatively flat on the right side of its maximum location in the r direction.

1.6. Comparison study with the Navier–Stokes equations with constant diffusion coefficient. Due to the two-scale solution structure in our potential singular solutions, it is essential that the variable diffusion coefficients degenerate at the origin. If we use non-degenerate diffusion coefficients, it will regularize the smaller scale $Z(t)$ and we will only have a single scale solution associated with $R(t) = O((T-t)^{1/2})$. We will present convincing numerical evidences which show that the Navier–Stokes equations with a constant diffusion coefficient and the same initial data indeed regularize the smaller scale and destroy the two-scale travel wave solution. The solution behaves completely differently in the late stage and does not seem to develop a finite time singularity.

1.7. Review of previous works. One of the best known results for the 3D Euler equations is the Beale–Kato–Majda non blowup criteria [MB02], which states that the smooth solution of the 3D Euler equations ceases to be regular at some finite time T if and only if $\int_0^T \|\nabla \boldsymbol{\omega}\|_{L^\infty} dt = \infty$. In [CFM96], Constantin–Fefferman–Majda showed that the local geometric regularity of the vorticity vector near the region of maximum vorticity could lead to the dynamic depletion of vortex stretching, thus preventing a potential finite time singularity (see also [DHY05]). An exciting recent development is the work by Elgindi [Elg19] (see also [EGM19]) who proved that the 3D axisymmetric Euler equations develop a finite time singularity for a class of $C^{1,\alpha}$ initial velocity with no swirl. There have been a number of very interesting results inspired by the Hou–Lou blowup scenario [LH14a, LH14b], see e.g. [KS14, CHK⁺17, KRYZ16, CH19, CHH19] and the excellent survey article [Kis18].

For the 3D Navier–Stokes equations, one of the best known results is the partial regularity result by Caffarelli–Kohn–Nirenberg [CKN82] (see also [Lin98]), which states that the one-dimensional Hausdorff measure of the singularity set is zero. This implies that any potential singularity of the axisymmetric Navier–Stokes equations must occur on the symmetry axis. In the case of axisymmetric

Navier-Stokes equations, there have been some very interesting theoretical developments regarding the lower bound on the blow-up rate, see e.g. [CSYTo8, CSTYo9, KNSSo9]. There has been also some interesting recent work on the criticality of the axisymmetric Navier–Stokes equations, see e.g. [LZ17]. In [Tao16], Tao proposed an averaged three-dimensional Navier–Stokes equation that preserves the energy identity for the Navier–Stokes equations, but blows up in finite time.

There has been a number of previous attempts to search for potential Euler singularities numerically. In [GS91], Grauer–Sideris presented numerical evidences that the 3D axisymmetric Euler equations with a smooth initial condition could develop a potential finite time singularity away from the symmetry axis. In [ES94], E and Shu studied the potential development of finite-time singularities in the 2D Boussinesq equations, with initial data completely analogous to those of [GS91, PS92] and found no evidence for singular solutions. Another well-known work on potential Euler singularity is the two anti-parallel vortex tube computation by Kerr in [Ker93]. In [HLo6], Hou and Li repeated the computation of [Ker93] with higher resolutions and only observed double exponential growth of the maximum vorticity in time. In [BHP16], Brenner–Hormoz–Pumir considered an iterative mechanism for potential singularity formation of the 3D Euler equations based on the transformation of vortex filaments into sheets and their subsequent instability back into filaments.

There have been relatively fewer works on singularity formation of the 3D incompressible Navier–Stokes equations. In [BP94], Boratav and Pelz presented computational results for the 3D incompressible Navier–Stokes equations with a sequence of increasing Reynolds numbers. Based on their computational results, they conjectured that the Euler equations with Kida’s high-symmetry initial data would develop a finite time singularity. In [HLo8b], Hou and Li also repeated the computation of [BP94] and found that the singularity reported in [BP94] is likely an artifact due to under-resolution. We refer to a recent review article [Gibo8] for a more comprehensive list of other numerical results related to potential Euler singularities.

The rest of the paper is organized as follows. In Section 2, we describe the setup of the problem in some detail, including the analytic construction of our initial data and the variable diffusion coefficients. In Section 3, we report the major findings of our numerical results, including the first sign of singularity and the main features of the potentially singular solution. Section 4 is devoted to numerical resolution study. In Section 5, we present a comparison study with the standard Navier–Stokes equations with constant diffusion coefficient. In Section 6, we investigate the asymptotic blowup scaling both numerically and by asymptotic scaling analysis. Some concluding remarks are made in Section 7. The detailed description of our numerical methods including the construction of our adaptive mesh and the filtering scheme will be deferred to the Appendix.

2. DESCRIPTION OF THE PROBLEM

In this paper, we study the 3D incompressible Navier–Stokes equations with variable diffusion coefficients:

$$\begin{aligned} \mathbf{u}_t + \mathbf{u} \cdot \nabla \mathbf{u} &= -\nabla p + \nabla \cdot (\nu \nabla \mathbf{u}) \\ \nabla \cdot \mathbf{u} &= 0, \end{aligned} \tag{2.1}$$

where $\mathbf{u} = (u^x, u^y, u^z)^T : \mathbb{R}^3 \mapsto \mathbb{R}^3$ is the 3D velocity vector, $p : \mathbb{R}^3 \mapsto \mathbb{R}$ is the scalar pressure, $\nabla = (\partial_x, \partial_y, \partial_z)^T$ is the gradient operator in \mathbb{R}^3 , and $\nu : \mathbb{R}^3 \mapsto \mathbb{R}^{3 \times 3}$ is the variable diffusion tensor. By taking the curl on both sides, the equations can be rewritten in the equivalent vorticity form

$$\omega_t + \mathbf{u} \cdot \nabla \omega = \omega \cdot \nabla \mathbf{u} + \nabla \times (\nabla \cdot (\nu \nabla \mathbf{u})),$$

where $\omega = \nabla \times \mathbf{u}$ is the 3D vorticity vector. The velocity \mathbf{u} is related to the vorticity via the vector-valued stream function ψ :

$$-\Delta \psi = \omega, \quad \mathbf{u} = \nabla \times \psi.$$

2.1. Axisymmetric Navier–Stokes equations. We will study the potential singularity formulation for 3D axisymmetric Navier–Stokes equations. In the axisymmetric scenario, it is convenient to rewrite equations (2.1) in cylindrical coordinates. Consider the the change of variables

$$x = r \cos \theta, \quad y = r \sin \theta, \quad z = z,$$

and the decomposition

$$\begin{aligned} \mathbf{v}(r, z) &= v^r(r, z)\mathbf{e}_r + v^\theta(r, z)\mathbf{e}_\theta + v^z(r, z)\mathbf{e}_z, \\ \mathbf{e}_r &= \frac{1}{r}(x, y, 0)^T, \quad \mathbf{e}_\theta = \frac{1}{r}(-y, x, 0)^T, \quad \mathbf{e}_z = (0, 0, 1)^T, \end{aligned}$$

for radially symmetric vector-valued functions $\mathbf{v}(r, z)$. The 3D Navier–Stokes equations (2.1) can be rewritten in the axisymmetric form:

$$u_t^\theta + u^r u_r^\theta + u^z u_z^\theta = -\frac{1}{r} u^r u^\theta + f_u, \quad (2.2a)$$

$$\omega_t^\theta + u^r \omega_r^\theta + u^z \omega_z^\theta = \frac{2}{r} u^\theta u_z^\theta + \frac{1}{r} u^r \omega^\theta + f_\omega, \quad (2.2b)$$

$$-\left(\Delta - \frac{1}{r^2}\right) \psi^\theta = \omega^\theta, \quad (2.2c)$$

$$u^r = -\psi_z^\theta, \quad u^z = \frac{1}{r}(r\psi^\theta)_r, \quad (2.2d)$$

where f_u and f_ω are the diffusion terms. The incompressibility condition

$$\frac{1}{r}(ru^r)_r + u_z^z = 0$$

is automatically satisfied owing to equations (2.2d). Equations (2.2), together with appropriate initial and boundary conditions, completely determine the evolution of 3D axisymmetric Navier–Stokes flows.

To determine the diffusion terms, we choose the variable diffusion tensor such that

$$\nu = \text{diag}(\nu^r, \nu^\theta, \nu^z)$$

in the cylindrical coordinates, where $\nu^r = \nu^r(r, z)$, $\nu^z = \nu^z(r, z)$ are functions of (r, z) . We remark that this is equivalent to choosing $\nu = \text{diag}(\nu^x, \nu^y, \nu^z)$ with $\nu^x = \nu^y = \nu^r$ in the Euclidean coordinates $(x, y, z) = (r \cos \theta, r \sin \theta, z)$. In order for ν to be a smooth function in the primitive coordinates (x, y, z) , we require that $\nu^r(r, z)$, $\nu^z(r, z)$ are even functions of r with respect to $r = 0$. With this choice of the variable diffusion coefficients, f_u and f_ω have the expressions

$$\begin{aligned} f_u &= \nu^r \left(u_{rr}^\theta + \frac{1}{r} u_r^\theta - \frac{1}{r^2} u^\theta \right) + \nu^z u_{zz}^\theta + \nu_r^r u_r^\theta + \nu_z^z u_z^\theta, \\ f_\omega &= \nu^r \left(\omega_{rr}^\theta + \frac{1}{r} \omega_r^\theta - \frac{1}{r^2} \omega^\theta \right) + \nu^z \omega_{zz}^\theta + \nu_r^r \omega_r^\theta + \nu_z^z \omega_z^\theta \\ &\quad + \nu_z^r \left(u_{rr}^r + \frac{1}{r} u_r^r - \frac{1}{r^2} u^r \right) + \nu_z^z u_{zz}^r - \nu_r^r \left(u_{rr}^z + \frac{1}{r} u_r^z \right) - \nu_r^z u_{zz}^z \\ &\quad + \nu_{rz}^r u_r^r + \nu_{zz}^z u_z^r - \nu_{rr}^r u_z^r - \nu_{rz}^z u_z^z. \end{aligned}$$

The axisymmetric Navier–Stokes equations (2.2) have a formal singularity at $r = 0$, which sometimes is inconvenient to work with. To remove the singularity, Hou and Li [HLo8a] introduced the variables

$$u_1 = u_\theta/r, \quad \omega_1 = \omega^\theta/r, \quad \psi_1 = \psi_\theta/r$$

and transform equations (2.2) into the form

$$u_{1,t} + u^r u_{1,r} + u^z u_{1,z} = 2u_1 \psi_{1,z} + f_{u_1}, \quad (2.3a)$$

$$\omega_{1,t} + u^r \omega_{1,r} + u^z \omega_{1,z} = 2u_1 u_{1,z} + f_{\omega_1}, \quad (2.3b)$$

$$-\left(\partial_r^2 + \frac{3}{r} \partial_r + \partial_z^2\right) \psi_1 = \omega_1, \quad (2.3c)$$

$$u^r = -r\psi_{1,z}, \quad u^z = 2\psi_1 + r\psi_{1,r}, \quad (2.3d)$$

where the diffusion terms f_{u_1}, f_{ω_1} are given by

$$f_{u_1} = \frac{1}{r} f_u = \nu^r \left(u_{1,rr} + \frac{3}{r} u_{1,r} \right) + \nu^z u_{1,zz} + \frac{1}{r} \nu_r^r u_1 + \nu_r^r u_{1,r} + \nu_z^z u_{1,z}, \quad (2.4a)$$

$$\begin{aligned} f_{\omega_1} = \frac{1}{r} f_\omega = & \nu^r \left(\omega_{1,rr} + \frac{3}{r} \omega_{1,r} \right) + \nu^z \omega_{1,zz} + \frac{1}{r} \nu_r^r \omega_1 + \nu_r^r \omega_{1,r} + \nu_z^z \omega_{1,z} \\ & + \frac{1}{r} \left(\nu_z^r \left(u_{1,rr}^r + \frac{1}{r} u_{1,r}^r - \frac{1}{r^2} u_{1,r}^r \right) + \nu_z^z u_{1,zz}^r - \nu_r^r \left(u_{1,rr}^z + \frac{1}{r} u_{1,r}^z \right) - \nu_r^z u_{1,zz}^r \right) \\ & + \frac{1}{r} \left(\nu_{rz}^r u_{1,r}^r + \nu_{zz}^z u_{1,r}^r - \nu_{rr}^r u_{1,z}^z - \nu_{rz}^z u_{1,z}^z \right). \end{aligned} \quad (2.4b)$$

Note that f_u, f_ω are even functions of r , thus f_{u_1}, f_{ω_1} are well defined as long as f_u, f_ω are smooth. Therefore, u_1, ω_1 , and ψ_1 are well defined as long as the corresponding solution to equations (2.2) remains smooth.

2.2. Settings of the solution. We will solve the transformed equations (2.3) in the cylinder region

$$\mathcal{D} = \{(r, z) : 0 \leq r \leq 1\}.$$

In particular, we will enforce the following properties of the solution:

- (1) u_1, ω_1, ψ_1 are periodic in z with period 1:

$$\begin{aligned} u_1(r, z, t) &= u_1(r, z+1, t), \quad \omega_1(r, z, t) = \omega_1(r, z+1, t), \\ \text{and } \psi_1(r, z, t) &= \psi_1(r, z+1, t) \quad \text{for all } (r, z) \in \mathcal{D}. \end{aligned} \quad (2.5a)$$

- (2) u_1, ω_1, ψ_1 are odd functions of z at $z = 0$:

$$\begin{aligned} u_1(r, z, t) &= -u_1(r, -z, t), \quad \omega_1(r, z, t) = -\omega_1(r, -z, t), \\ \text{and } \psi_1(r, z, t) &= -\psi_1(r, -z, t) \quad \text{for all } (r, z) \in \mathcal{D}. \end{aligned} \quad (2.5b)$$

- (3) The smoothness of the solution in the Cartesian coordinates implies that $u^\theta, \omega^\theta, \psi^\theta$ must be an odd function of r [LW06]. Consequently, u_1, ω_1, ψ_1 must be even functions of r at $r = 0$, which imposes the pole conditions:

$$u_{1,r}(0, z) = \omega_{1,r}(0, z) = \psi_{1,r}(0, z) = 0. \quad (2.5c)$$

- (4) The velocity satisfies a no-flow boundary condition on the solid boundary $r = 1$:

$$\psi_1(1, z, t) = 0 \quad \text{for all } z. \quad (2.5d)$$

- (5) Due to the existence of non-degenerate viscosity at $r = 1$, the tangent flows on the solid boundary should satisfy a no-slip boundary condition:

$$u^\theta(1, z, t) = u^z(1, z, t) = 0, \quad \text{for all } z. \quad (2.5e)$$

In view of (2.3d) and (2.5d), this further leads to $\psi_{1,r}(1, z, t) = 0$. Therefore, the no-slip boundary in terms of the new variables u_1, ω_1, ψ_1 reads

$$u_1(1, z, t) = 0, \quad \omega_1(1, z, t) = -\psi_{1,rr}(1, z, t), \quad \text{for all } z. \quad (2.5f)$$

In fact, equations (2.3) automatically preserve properties (1)–(4) of the solution for all time $t \geq 0$ if the initial data satisfy these properties and if the variable diffusion coefficients ν^r, ν^z satisfy

- (i) v^r, v^z are periodic in z with period 1.
- (ii) v^r, v^z are even functions of z at $z = 0$.
- (iii) v^r, v^z are even functions of r at $r = 0$.

The no-slip boundary condition (5) will be enforced numerically. By the periodicity and the odd symmetry of the solution, we only need to solve equations (2.3) in the half-period domain

$$\mathcal{D}_1 = \{(r, z) : 0 \leq r \leq 1, 0 \leq z \leq 1/2\}.$$

Note that the properties (2.5a) and (2.5b) together imply that u_1, ω_1, ψ_1 are also odd functions of z at $z = 1/2$. The boundaries of \mathcal{D}_1 then behave like “impermeable walls” since

$$u^r = -r\psi_{1,z} = 0 \quad \text{on } r = 1 \quad \text{and} \quad u^z = 2\psi_1 + r\psi_{1,r} = 0 \quad \text{on } z = 0, 1/2.$$

2.3. Initial data. We construct the initial data based on our empirical insights and understanding of the potential blowup scenario that we shall explain later. The initial data are given by

$$u_1^0(r, z) = m_u^{(1)} \frac{u_1^{(1)}(r, z)}{\|u_1^{(1)}\|_{L^\infty}} + m_u^{(2)} u_1^{(2)}(r, z), \quad \omega_1^0(r, z) = m_\omega^{(1)} \frac{\omega_1^{(1)}(r, z)}{\|\omega_1^{(1)}\|_{L^\infty}} + m_\omega^{(2)} \omega_1^{(2)}(r, z), \quad (2.6)$$

where

$$\begin{aligned} u_1^{(1)} &= \frac{\sin(2\pi z)}{1 + (\sin(\pi z)/a_{z1})^2 + (\sin(\pi z)/a_{z2})^4} \cdot \frac{r^8(1-r^2)}{1 + (r/a_{r1})^{10} + (r/a_{r2})^{14}}, \\ u_1^{(2)} &= \sin(2\pi z) \cdot r^2(1-r^2), \\ \omega_1^{(1)} &= g(r, z) \cdot \frac{\sin(2\pi z)}{1 + (\sin(\pi z)/b_{z1})^2 + (\sin(\pi z)/b_{z2})^4} \cdot \frac{r^8(1-r^2)}{1 + (r/b_{r1})^{10} + (r/b_{r2})^{14}}, \\ \text{and } \omega_1^{(2)} &= \sin(2\pi z) \cdot r^2(1-r^2). \end{aligned}$$

The parameters are chosen as follows:

$$\begin{aligned} m_u^{(1)} &= 7.6 \times 10^3, \quad m_u^{(2)} = 50, \quad m_\omega^{(1)} = 8.6 \times 10^7, \quad m_\omega^{(2)} = 50, \\ a_{z1} &= (1.2 \times 10^{-4})\pi, \quad a_{z2} = (2.5 \times 10^{-4})\pi, \quad a_{r1} = 9 \times 10^{-4}, \quad a_{r2} = 5 \times 10^{-3}, \\ b_{z1} &= (1 \times 10^{-4})\pi, \quad b_{z2} = (1.5 \times 10^{-4})\pi, \quad b_{r1} = 9 \times 10^{-4}, \quad a_{r2} = 3 \times 10^{-3}. \end{aligned}$$

The function $g(r, z)$ is defined through a soft-cutoff function, and it forces the profile of ω_1^0 to have a smooth “corner” shape. Define the soft-cutoff function

$$f_{sc}(x; a, b) = \frac{e^{(x-a)/b}}{e^{(x-a)/b} + e^{-(x-a)/b}}. \quad (2.7)$$

Then $g(r, z)$ is given by the formula

$$\begin{aligned} g(r, z) &= (1 - f_{sc}(\sin(\pi z)/\pi; 0.7b_{z1}, 0.5b_{z1})) \cdot f_{sc}(r; b_{r1} + 0.5b_{z1}, b_{z1}) \\ &\quad \times (1 - f_{sc}(-\sin(\pi z)/\pi; 0.7b_{z1}, 0.5b_{z1})) \cdot f_{sc}(r; b_{r1} + 0.5b_{z1}, b_{z1}). \end{aligned}$$

Moreover, the initial stream function ψ_1^0 is obtained from ω_1^0 via the Poisson equation

$$-\left(\partial_r^2 + \frac{3}{r}\partial_r + \partial_z^2\right)\psi_1^0(r, z) = \omega_1^0(r, z) \quad \text{for } (r, z) \in \mathcal{D}_1,$$

subject to the homogeneous boundary conditions

$$\psi_{1,r}^0(0, z) = \psi_1^0(1, z) = \psi_1^0(r, 0) = \psi_1^0(r, 1/2) = 0.$$

It is not hard to check that the initial data $u_1^0, \omega_1^0, \psi_1^0$ satisfy all the conditions (1)–(4). Figure 2.1 shows the profiles and contours of the initial data u_1^0 and ω_1^0 .

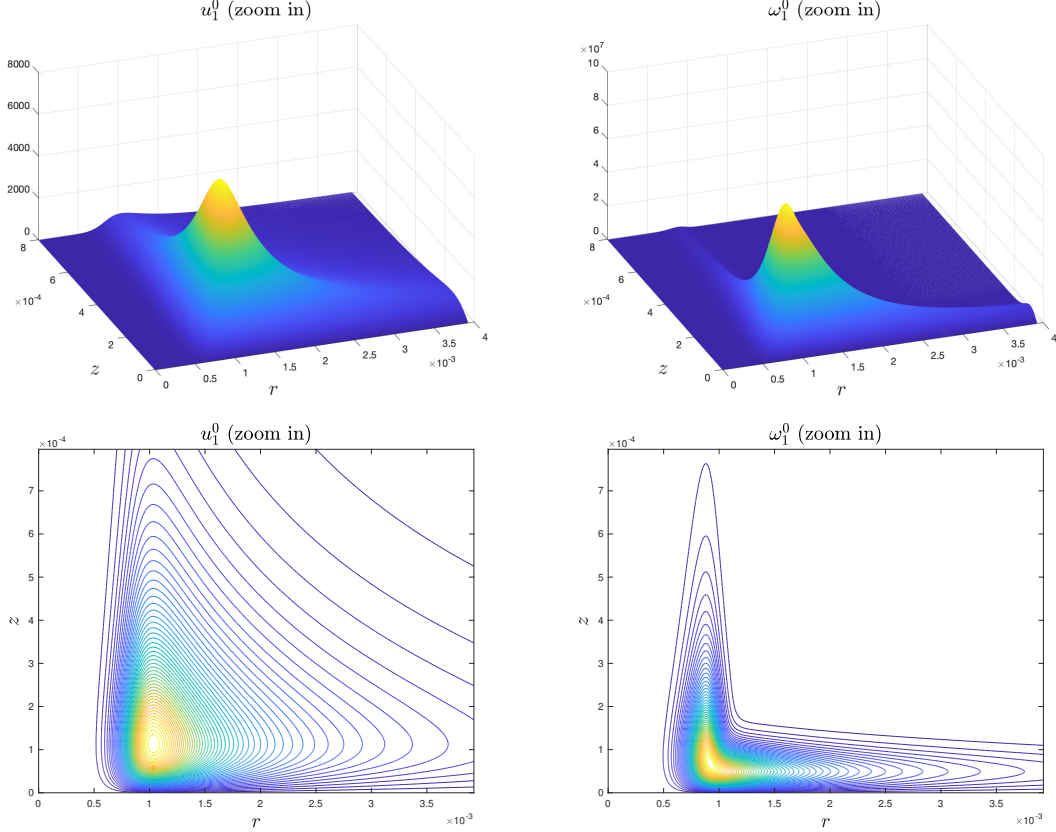


Figure 2.1: Profiles (first row) and contours (second row) of the initial data u_1^0 and ω_1^0 on a zoom-in domain $(r, z) \in [0, 4 \times 10^{-3}] \times [0, 8 \times 10^{-4}]$.

As we will see in Section 3, the solution to the initial-boundary problem (2.3)–(2.6) develops a potential finite singularity that is focusing at the origin $(r, z) = (0, 0)$ and has two separated spatial scales. The sustainability and stability of this two-scale singularity crucially rely on a coupling blowup mechanism that will be discussed in details in Section 3.5. Our construction of the initial data serves to trigger this blowup mechanism, owing to the following principles:

- ω_1^0 is chosen to be an odd function of z at $z = 0$, so that the angular vorticity $\omega^\theta = r\omega_1$ has a dipole structure on the whole period $\{(r, z) : r \in [0, 1], z \in [-1/2, 1/2]\}$ that induces a strong inward radial flow near the symmetry plane $z = 0$ (see Figure (3.11)). This flow structure has the desirable property that pushes the critical part of the solution towards the symmetry axis.
- u_1^0 is also chosen to be odd in z at $z = 0$, so that the gradient $u_{1,z}^0$ is non-trivial and has the desirable sign between the maximum location of u_1^0 and $z = 0$. As a result, the forcing term $2u_1u_{1,z}$ in the ω_1 equation (2.3b) is positive and large near $z = 0$, which contributes to the rapid growth of ω_1 .
- For u_1 and ω_1 to have a good initial alignment, we manipulate the initial data so that the maximum location of ω_1^0 is slightly below the maximum location of u_1^0 , where $u_{1,z}^0$ large and has the proper sign.

- We scale the magnitude of u_1^0 and ω_1^0 so that $\|\omega_1^0\|_{L^\infty} \approx \|u_1^0\|_{L^\infty}^2$. This is because we have observed the blowup scaling property that $\|\omega_1(t)\|_{L^\infty} \sim \|u_1(t)\|_{L^\infty}^2$ in our computations. The reason behind this blowup scaling property will be made clear in Section 6.

These principles are critical for the solution to trigger a positive feed back mechanism that leads to a sustainable focusing blowup. We will have more discussions on the understanding of this mechanism in Section 3.5. We remark that the potential blowup is robust under relatively small perturbation in the initial data. In fact, we have observed similar two-scale blowup phenomena from a family of initial data that satisfy the above properties.

2.4. Variable diffusion coefficients. In our main cases of computation, we choose the variable diffusion coefficients ν^r, ν^z to be the sum of a space-dependent part and a time-dependent part:

$$\nu^r(r, z, t) = \frac{10r^2}{1 + 10^8 r^2} + \frac{10^2(\sin(\pi z)/\pi)^2}{1 + 10^{11}(\sin(\pi z)/\pi)^2} + \frac{2.5 \times 10^{-2}}{\|\omega^\theta(t)\|_{L^\infty}}, \quad (2.8a)$$

$$\nu^z(r, z, t) = \frac{10^{-1}r^2}{1 + 10^8 r^2} + \frac{10^4(\sin(\pi z)/\pi)^2}{1 + 10^{11}(\sin(\pi z)/\pi)^2} + \frac{2.5 \times 10^{-2}}{\|\omega^\theta(t)\|_{L^\infty}}. \quad (2.8b)$$

We remark that the space-dependent parts of ν^r, ν^z are very small (below 10^{-7}) on the whole domain and are of order $O(r^2) + O(z^2)$ for $r \leq 10^{-4}$ and $z \leq 10^{-5}$. Since the quantity $\|\omega^\theta(t)\|_{L^\infty}$ is growing rapidly in our computation, the time-dependent part in ν^r, ν^z is also very small (below 4×10^{-7} initially) and is decreasing rapidly in time. In fact, the time-dependent part is non-essential for the potential singularity formation in our scenario; it only serves to regularize the solution in the very early stage of our computation and will quickly be dominated by the space-dependent parts (see Figure 5.5 in Section 5). We can even remove the time-dependent part of ν^r, ν^z after the solution enters a stable phase, and the phenomena we observe would remain almost the same.

In all, we only have an extremely weak diffusion effect with smooth degenerate coefficients. Nevertheless, the diffusion plays an important role in the development of the singularity in our blowup scenario. On the one hand, the non-trivial diffusion in the far field prevents the shearing induced instability from disturbing the locally self-similar solution and the nonlinear alignment of vortex stretching in the near field. On the other hand, we will see in Section 5 that the degeneracy of the diffusion is crucial for a two-scale singularity to survive in a shrinking domain near the origin $(r, z) = (0, 0)$. Furthermore, we will argue in Section 6 that the order of degeneracy of ν^r, ν^z contributes to the formation of a potential locally self-similar blowup.

For the sake of comparison, we will also study the solution of the original Navier–Stokes equations with constant diffusion coefficient on the entire domain. We will compare the numerical results from different choices of diffusion coefficients to study the effect of viscosity in the potential singularity near the symmetry axis $r = 0$. As a preview, there is no blowup observed with a constant diffusion coefficient, verifying the criticality of degeneracy in the diffusion coefficients.

2.5. The numerical methods. To numerically compute the potential singularity formation of the equations (2.3), we have designed a composite algorithm that is well-tailored to the solution in our blowup scenario. The detailed descriptions of our numerical methods will be presented in Appendix A. Here we briefly introduce the main ingredients of our overall algorithm.

2.5.1. Adaptive mesh. We will see in Section 3 that the profile of the solution quickly shrinks in space and develops complex geometric structures, which makes it extremely challenging to numerically compute the solution accurately. In order to overcome this difficulty, we design in Appendix A.1 a special adaptive mesh strategy to resolve the singularity formation near the origin $(r, z) = (0, 0)$. More precisely, we construct a pair of mapping functions

$$r = r(\rho), \quad z = z(\eta), \quad (\rho, \eta) \in [0, 1] \times [0, 1]$$

that maps the square $[0, 1] \times [0, 1]$ bijectively to the computational domain $\mathcal{D}_1 = \{(r, z) : 0 \leq r \leq 1, 0 \leq z \leq 1/2\}$. The densities of these mapping functions are dynamically adaptive to the complex multi-scale structure of the solution, which is crucial to the accurate computation of the potential singularity. Given a uniform mesh of size $n \times m$ on the $\rho\eta$ -domain, the adaptive mesh covering the physical domain is produced as

$$r_i = r(ih_\rho), \quad h_\rho = 1/n; \quad z_j = z(jh_\eta), \quad h_\eta = 1/m.$$

The precise definition and construction of the mesh mapping functions are described in Appendix B.

2.5.2. B-spline based Galerkin Poisson solver. One crucial step in our computation is to solve the Poisson problem (2.3c) accurately. The Poisson solver we use should be compatible to the our adaptive mesh setting. Moreover, the finite dimensional solver needs to be easy to construct from the mesh, as the mesh is updated frequently in our computation. For these reasons, we choose to implement the Galerkin finite element method based on a tensorization of B-spline functions, following the framework of Luo and Hou [LH14b] who used this method for computing the potential singularity formation of the 3D Euler equations on the solid boundary. The description of the Poisson solver will be given in Appendix A.2.

2.5.3. Numerical regularization. The potential blowup solution we compute develops a long thin tail structure, stretching from the sharp front to the far field. As we will report in Section 7, this tail structure can develop some shearing induced instability in the late stage of the computation, which may disturb the blowup mechanism. Therefore, we have chosen to apply some numerical regularization techniques to stabilize the solution, especially the tail part of the solution. In Appendix A.4, we introduce two types of regularizing operators. The first one is a low-pass filtering operator LPF in the $\rho\eta$ -plane, which is applied to all cases of our computations to suppress some mild oscillations. The second one is a stronger regularizing technique, the re-meshed low-pass filtering RLPF, that is only applied in our comparison study to gain further insight into the nature of these mild oscillations. We use the RLPF filtering to illustrate potential approaches to control the mild oscillations induced by the shearing flow along the thin tail.

2.5.4. Overall algorithm. We use 2nd-order centered difference schemes for the discretization in space and a 2nd-order explicit Runge–Kutta method for marching the solution in time. We also apply the basic low-pass filtering LPF in an L -shape domain covering the tail region when we update the velocity field, but we do not apply the LPF filtering in the most singular region. We have chosen to employ 2nd-order methods since the basic low-pass filtering LPF introduces a 2nd-order error of size $O(h_\rho^2 + h_\eta^2)$. The resulting overall algorithm for solving the initial-boundary value problem (2.3)–(2.6) is formally 2nd-order accurate in space and in time, which will be verified in Section 4.2.

3. NUMERICAL RESULTS: FIRST SIGN OF SINGULARITY

We have numerically solved the initial-boundary value problem (2.3)–(2.6) on the half-period cylinder $\mathcal{D}_1 = \{(r, z) : 0 \leq r \leq 1, 0 \leq z \leq 1/2\}$ with meshes of size $(n, m) = (256p, 128p)$ for $p = 2, 3, \dots, 8$. In particular, we have performed computations in 3 cases:

Case 1: no re-meshed low-pass filtering RLPF_c^k is applied; ν^r, ν^z given by (2.8).

Case 2: no re-meshed low-pass filtering RLPF_c^k is applied; $\nu^r = \nu^z = \mu$ for some constant μ .

Case 3: re-meshed low-pass filtering RLPF_c^k is applied with $k = 5, 10, 25, 50, N = M = m$; ν^r, ν^z given by (2.8).

See Appendix A.4 for the definition of RLPF_c^k . We will focus our discussions on the potential blowup phenomena in Case 1. Our results suggest that the solution will develop a singularity on the symmetry axis $r = 0$ in finite time, and we will provide ample evidences to support this finding. We first present,

in this section, the major features of the potential finite-time singularity revealed by our computation. In Section 4, we carry out a careful resolution study of the numerical solutions. Then we further quantitatively investigate the properties of the potential singularity and analyze the potential blowup scaling properties in Section 6.

Cases 2 and 3 are mainly for comparison purposes. Case 2 compares the solution of the original Navier–Stokes equations with the solution of the Navier–Stokes equations with variable diffusion coefficients using the same initial data. The results in Case 2 show that the degeneracy of the diffusion coefficients near $(r, z) = (0, 0)$ is critical for a sustainable singularity that approaches the symmetry axis $r = 0$. The corresponding numerical results and discussions are presented in Section 5.

Case 3 demonstrates how the strength of the low-pass filtering affects the numerical results. It shows that the potential blowup we observe is robust and insensitive to the numerical smoothing that we use. The re-meshed low-pass filtering is not essential in the development of the blowup; it is only meant to control mild oscillations that appears in the late stage of the computation. We will present our detailed study of this mild instability and the results in Case 3 in Section 7.

3.1. Profile evolution. In this subsection, we investigate how the profiles of the solution evolve in time. We will use the numerical results in Case 1 computed on the adaptive mesh of size $(n, m) = (1024, 512)$. We have computed the numerical solution in this case up to time $t = 1.76 \times 10^{-4}$ when it is still well resolved. We do not continue our computation in Case 1 beyond this time for two main reasons, which will be explained in Section 4 and Section 7, respectively. The computation roughly consists of two phases: a warm-up phase ($t \in [0, 1.6 \times 10^{-4}]$) and a stable phase ($t \in (1.6 \times 10^{-4}, 1.76 \times 10^{-4}]$). In the warm-up phase, the solution evolves from the smooth initial data into a special structure. In the stable phase, the solution maintains a certain geometric structure and blows up stably.

Figure 3.1 illustrates the evolution of u_1, ω_1 in the late warm-up phase by showing the solution profiles at 3 different times $t = 1.38 \times 10^{-4}, 1.55 \times 10^{-4}, 1.63 \times 10^{-4}$. We can see that the magnitudes of u_1, ω_1 grow in time. The “peak” parts of the profiles travel towards the symmetry axis $r = 0$ and shrink in space. The profile of u_1 develops sharp gradients around the peak; in particular, it develops a sharp front in the r direction. This is clearer if we look at the cross-sections of u_1 in both directions (Figure 3.2). Moreover, ω_1 develops a thin curved structure. Between the sharp front and the symmetry axis $r = 0$, there is a “vacuum” region where u_1, ω_1 are almost 0. Both u_1 and ω_1 form a long tail part propagating towards the far field. The vacuum region has an effect similar to that of a “moving boundary” and the long tail being propagated down stream resembles the vortex shedding phenomena that is typically observed for flow past an object for the incompressible 3D Navier–Stokes equations.

Let $(R(t), Z(t))$ denote the maximum location of $u_1(r, z, t)$. We will always use this notation throughout the paper. Figure 3.2 shows the cross sections of u_1 going through the point $(R(t), Z(t))$ in both directions. That is, we plot $u_1(r, Z(t), t)$ versus r and $u_1(R(t), z, t)$ versus z , respectively. It is clear that u_1 develops sharp gradients in both directions. In the r direction, u_1 forms a sharp front and a “vacuum” region between the sharp front and $r = 0$. In the z direction, the profile of u_1 develops a compact support (another “vacuum region”) that is shrinking towards $z = 0$.

3.2. Two scales. Figure 3.3 (first column) shows the trajectory of the maximum location $(R(t), Z(t))$ of $u_1(r, z, t)$. We can see that $(R(t), Z(t))$ moves towards the origin $(r, z) = (0, 0)$, but with different rates in the two directions. The trajectory tends to become parallel to the horizontal axis $z = 0$ in the stable phase, which means that $Z(t)$ converges to 0 much faster than $R(t)$. As shown in the second column of Figure 3.3, the ratio $R(t)/Z(t)$ grows rapidly in time, especially in the stable phase. These evidences imply that there are two separate spatial scales in the solution. We can see this more clearly if we plot the solution profiles in a square domain in the rz -plane. For example, Figure 3.4 shows the profiles and level sets of u_1, ω_1 at time $t = 1.63 \times 10^{-4}$ in a square domain $\{(r, z) : 0 \leq r \leq 10^{-3}, 0 \leq z \leq 10^{-3}\}$. The profiles have a sharp front in the r direction and are

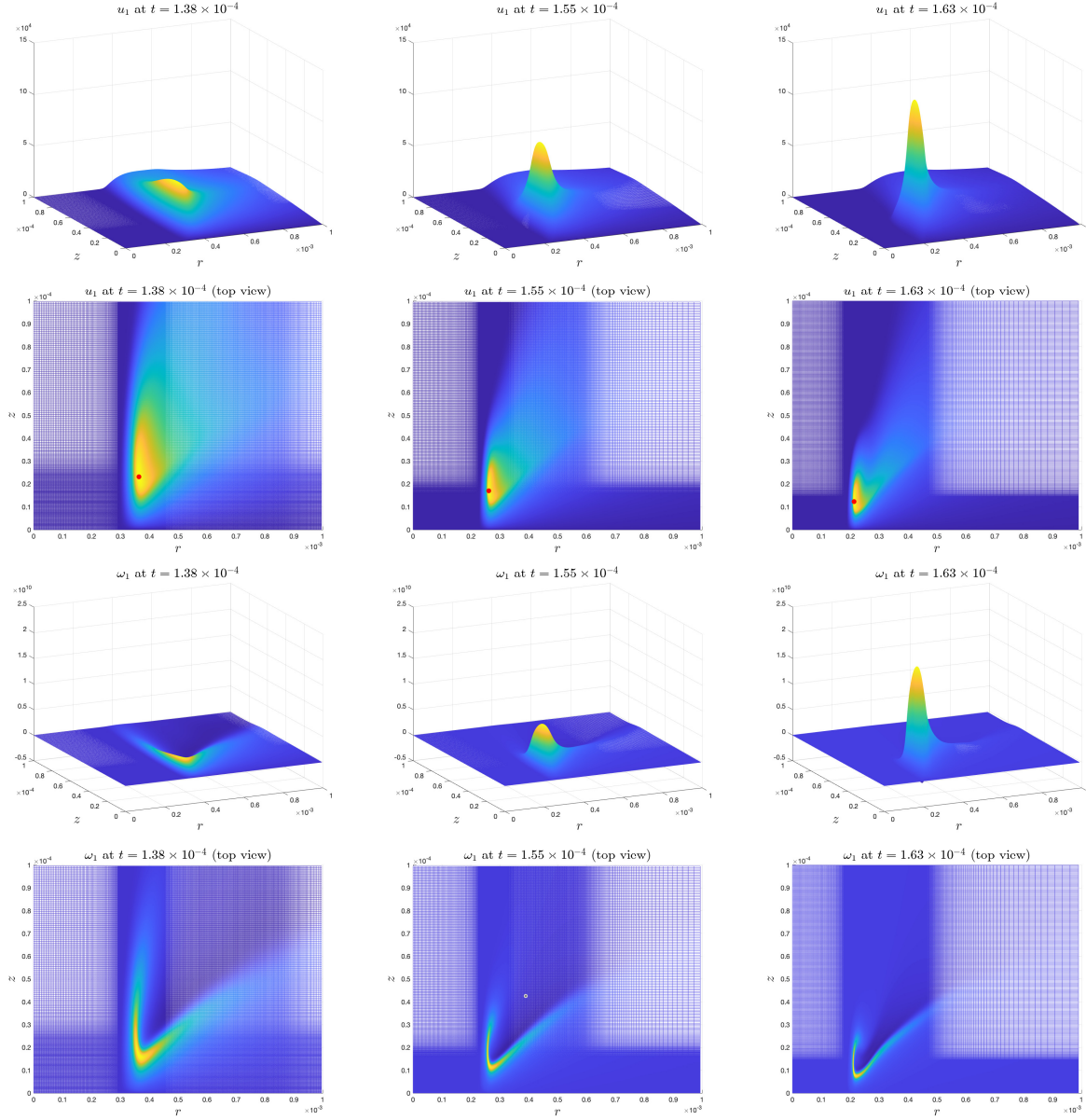


Figure 3.1: The evolution of the profiles of u_1 (row 1 and 2) and ω_1 (row 3 and 4) in Case 1. Line 1 and 3 are the profiles of u_1, ω_1 at three different times; Line 2 and 4 are the corresponding top-views. The red dot is the location of maximum u_1 .

extremely thin in the z direction, which corresponds to the scale of $Z(t)$ (the smaller scale). The long spreading tails of the profiles and the distance between the sharp front and the symmetry axis $r = 0$ correspond to the scale of $R(t)$.

If we zoom into a neighborhood of the smaller scale around the location $(R(t), Z(t))$, we can see that the smooth profiles of u_1, ω_1 are locally isotropic. Figure 3.5 shows the local isotropic profiles of u_1, ω_1 near the sharp front at a later time $t = 1.75 \times 10^{-4}$. These profiles are very smooth with respect to the smaller scale. In fact, such local structures have been developed ever since the solution enters the stable phase ($t \geq 1.6 \times 10^{-4}$), and they remain stable afterwards. We will further investigate this in Section 6.5.

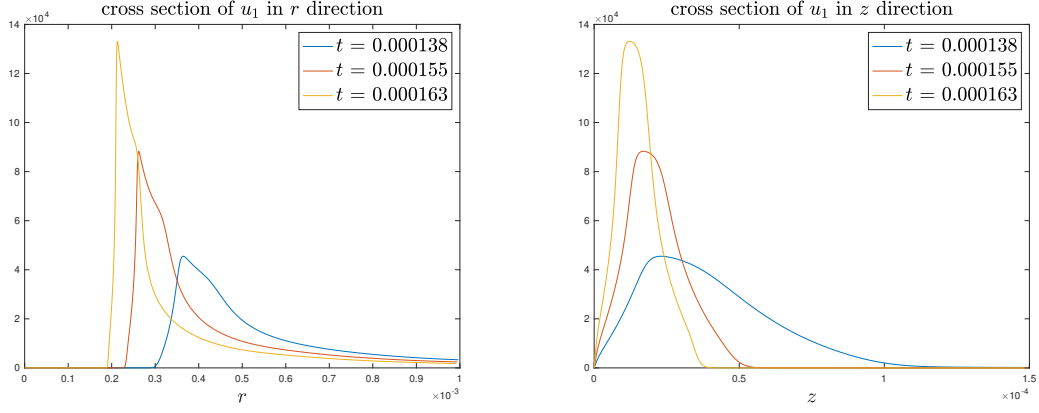


Figure 3.2: Cross sections of u_1 in both directions at different times.

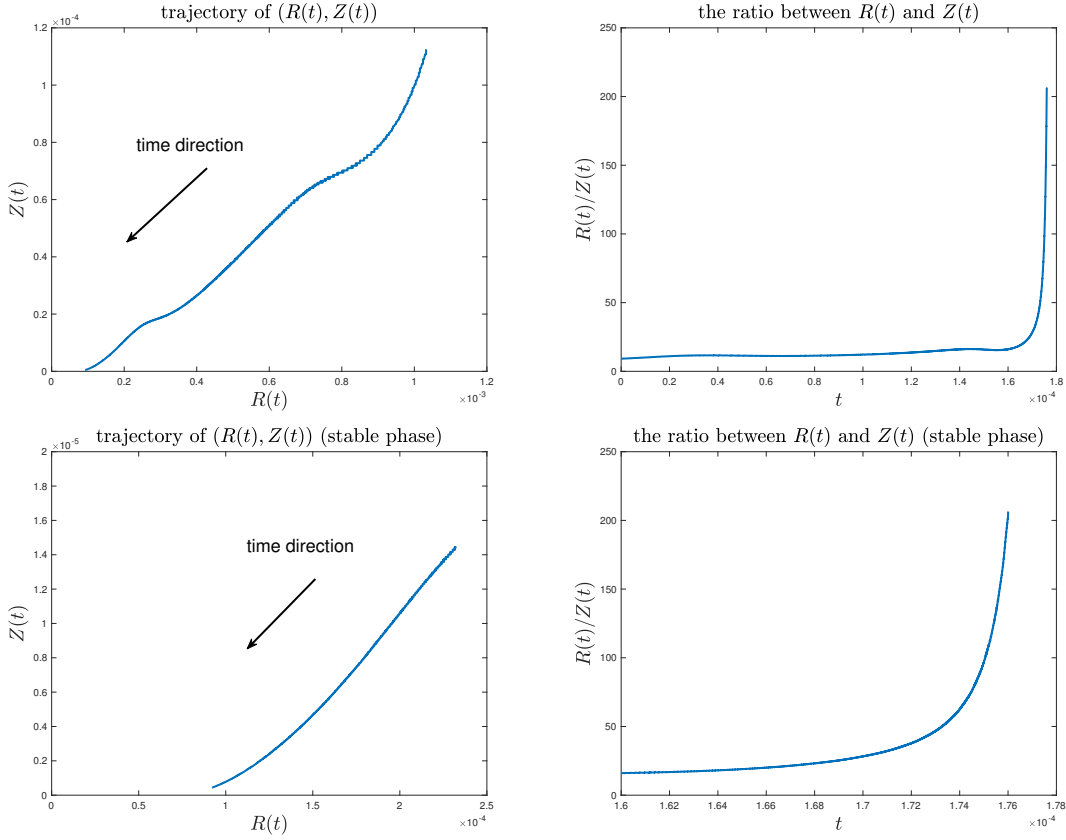


Figure 3.3: The trajectory of $(R(t), Z(t))$ and the ratio $R(t)/Z(t)$ as a function of time for $t \in [0, 1.76 \times 10^{-4}]$. First row: the whole computation. Second row: the stable phase.

One interesting perspective to interpret the evolution of u_1 is by seeing it as some form of “density”, for that u_1 is every where positive in the half-period domain \mathcal{D}_1 for all time $t \geq 0$ (which is guaranteed by our setting of the initial-boundary value problem (2.3)–(2.6)). We can see in Figure 3.5(a) and (b) that the profile of u_1 , which can be viewed as a distribution of the “density”, shows a clear “two-phase” feature. The sharp cliff surrounding the bulk part of u_1 behaves like a “moving boundary” between the two phases, whose contour is roughly indicated by the red level set of u_1 in Figure 3.5. On the

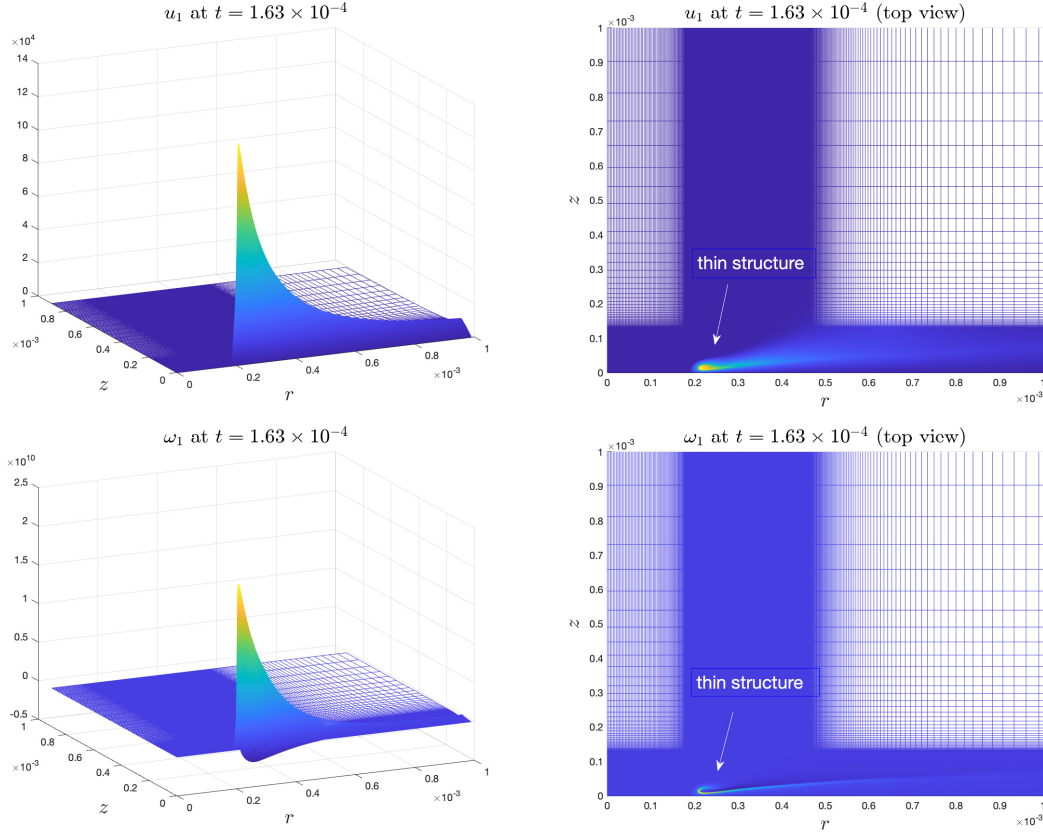


Figure 3.4: Profiles and level sets of u_1 (first row) and ω_1 (second row) at time $t = 1.63 \times 10^{-4}$ in the square domain $\{(r, z) : 0 \leq r \leq 10^{-3}, 0 \leq z \leq 10^{-3}\}$.

inner side of the “moving boundary” (where the red point is located), u_1 is large and smooth, which corresponds to a fluid phase with heavy density. On the outer side, however, u_1 is close to 0, which corresponds to a vacuum phase of the fluid. The fact that u_1 experiences a big jump from almost zero to a large value across the “moving boundary” suggests that the local flow near the center of the blowup can be treated formally as a “two-phase” flow. The evolution of the u_1 profile thus can be locally interpreted as the evolution of a two-phase flow separated by a “moving boundary”.

It is curious that the contours of u_1 and ω_1 seem to have the same shape. The thin structure of ω_1 behaves like a regularized 1D delta function supported along the “boundary” of the bulk part of u_1 , which is roughly indicated by the red curve. In fact, we will see in Section 6 that this phenomena is an evidence of the existence of a two-scale, locally self-similar blowup.

In summary, the solution to the initial-boundary value problem (2.3)–(2.6) has the following major features:

- The profile of u_1 develops a sharp front in the r direction. The profile of ω_1 deforms into a thin structure. Both u_1 and ω_1 develop a thin structure in the z direction. These geometric structures are featured by two separated spatial scales.
- The sharp front travels towards the symmetry axis $r = 0$. The maximum location $(R(t), Z(t))$ of u_1 travels towards the origin $(r, z) = (0, 0)$.
- The larger scale corresponds to $R(t)$ and the long tail of the solution.
- The smaller scale corresponds to $Z(t)$ and the local isotropic profiles near the sharp front.

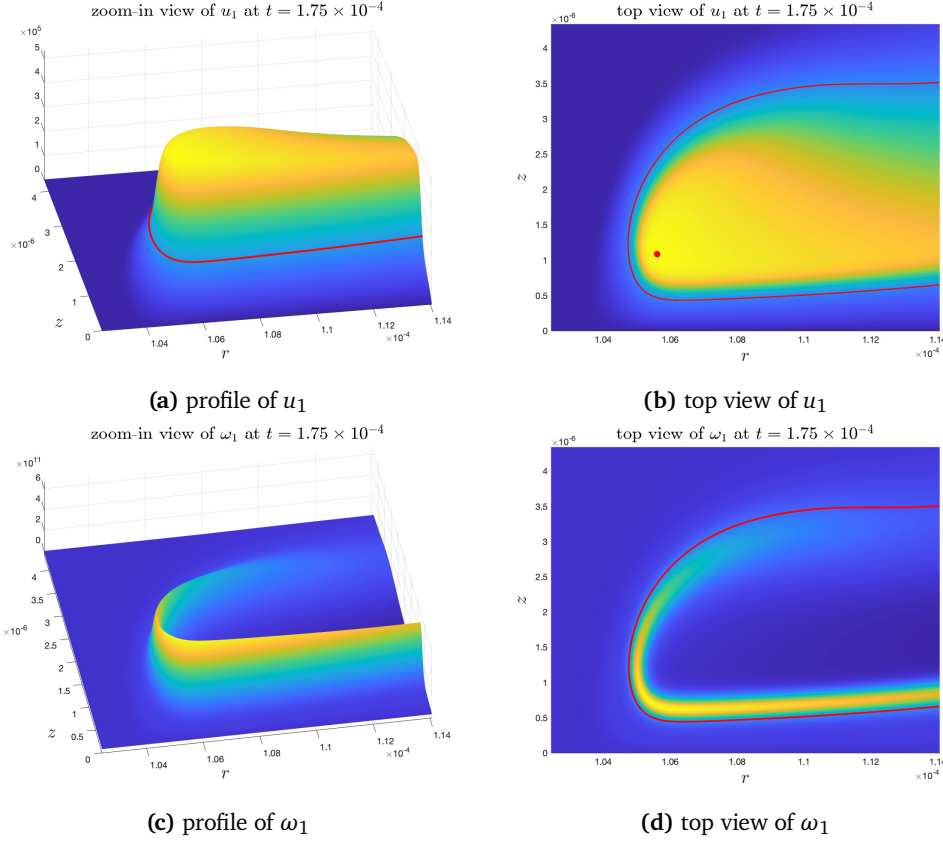


Figure 3.5: Zoom-in views of u_1, ω_1 at time $t = 1.75 \times 10^{-4}$. First row: profile and top view of u_1 . Second row: profile and top view of ω_1 . The red curve (in all figures above) is the level set of u_1 for the value $0.3\|u_1\|_{L^\infty}$, and the red point is the maximum location of u_1 .

We remark that the numerical solutions computed in cases 2 and 3 have almost the same features as described above in Case 1. The main difference between the 3 cases is how long these features can stay stable in time.

3.3. Rapid growth. The most important observation in our computation is the rapid growth of the solution. The maximums of $|u_1|$, $|\omega_1|$ and $|\omega|$ as functions of time are reported in Figure 3.6. Here

$$\omega = (\omega^\theta, \omega^r, \omega^z)^T = (r\omega_1, -ru_{1,z}, 2u_1 + ru_{1,r})^T$$

is the vorticity vector, and

$$|\omega| = \sqrt{(\omega^\theta)^2 + (\omega^r)^2 + (\omega^z)^2}.$$

We can see that these variables grow rapidly in time. In particular, they grow rapidly in the stable phase ($t \in [1.6 \times 10^{-4}, 1.76 \times 10^{-4}]$). Moreover, the second row in Figure 3.6 shows that the solution grows much faster than a double-exponential rate.

The rapid growth of the maximum vorticity $\|\omega\|_{L^\infty}$ is an important indicator of a finite time singularity. In fact, the famous Beale–Kato–Majda criterion [BKM84] states that the solution to the standard Navier–Stokes equations ceases to exist in some regularity class H^s (for $s \geq 3$) at some finite time T_* if and only if

$$\int_0^{T_*} \|\omega(t)\|_{L^\infty} dt = +\infty. \quad (3.1)$$

It is not hard to see that the argument in [BKM84] (with slight modifications) also works for the Navier–Stokes equations with variable diffusion coefficient if the coefficient tensor ν is a positive definite matrix that is uniformly bounded from below, i.e. $\nu \geq c\mathbf{I}$ in the entire space for some constant $c > 0$.

However, if the diffusion coefficient ν is degenerate as in our scenario, the quantity $\int_0^{T_*} \|\omega(t)\|_{L^\infty} dt$ can no longer control the regularity of the solution. To see this, we consider the L_2 estimate of ω , which is the first step in Beale–Kato–Majda’s argument. The variable diffusion coefficient ν gives rise to a term like $\langle \nabla \omega, G_\nu \nabla u \rangle$, here G_ν is a tensor related to the derivatives of ν . This term cannot be controlled by the L_2 norm of ω and the diffusion term with a degenerate coefficient. As a result, one cannot obtain a priori L_2 estimate of ω in terms of $\int_0^{T_*} \|\omega(t)\|_{L^\infty} dt$.

Nevertheless, we can still use a standard argument to show in that, the solution to the Navier–Stokes equations (2.1) with a degenerate diffusion coefficient ν ceases to exist in some regularity class H^s ($s \geq 3$) if and only if

$$\int_0^{T_*} \|\nabla u(t)\|_{L^\infty} dt = +\infty.$$

Moreover, it is clear that $\|\omega\|_{L^\infty} \lesssim \|\nabla u\|_{L^\infty}$. Therefore, the rapid growth of maximum vorticity $\|\omega\|_{L^\infty}$ is still a good indicator for a finite time singularity even in the case of a degenerate diffusion coefficient. We thus still view $\|\omega\|_{L^\infty}$ as a quantity of interest in our discussions. We will demonstrate in Section 6 that the growth of $\|\omega\|_{L^\infty}$ has a very nice fitting to an inverse power law

$$\|\omega(t)\|_{L^\infty} \approx (T - t)^{-\gamma}$$

for some finite time T and some power $\gamma > 1$. This then implies that the solution shall develop a potential singularity at a finite time T .

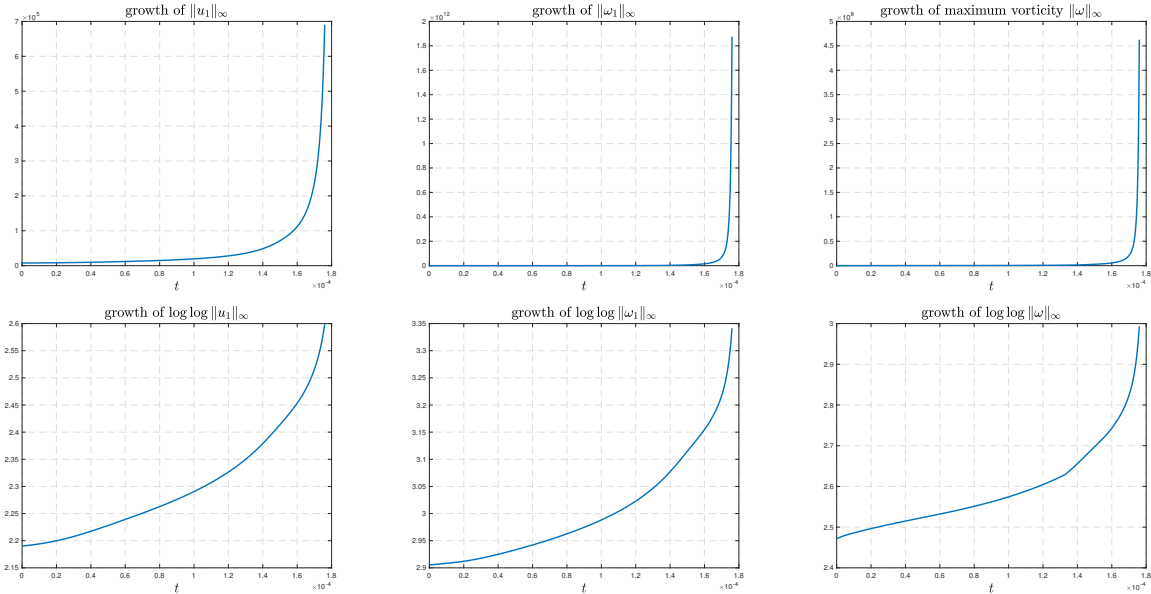


Figure 3.6: First row: the growth of $\|u_1\|_{L^\infty}$, $\|\omega_1\|_{L^\infty}$ and $\|\omega\|_{L^\infty}$ as functions of time. Second row: $\log \log \|u_1\|_{L^\infty}$, $\log \log \|\omega_1\|_{L^\infty}$ and $\log \log \|\omega\|_{L^\infty}$.

3.4. Velocity field. In this subsection, we investigate the feature of the velocity field. We first study the 3D velocity field $u = u^r e_r + u^\theta e_\theta + u^z e_z$ (denoted by (u^r, u^θ, u^z)) by looking at the induced streamlines. An induced streamline $\{\Phi(s; X_0)\}_{s \geq 0} \subset \mathbb{R}^3$ is completely determined by the background velocity u

and the initial point $X_0 = (x_0, y_0, z_0)^T$ through the initial value problem

$$\frac{\partial}{\partial s} \Phi(s; X_0) = \mathbf{u}(\Phi(s; X_0)), \quad s \geq 0; \quad \Phi(0; X_0) = X_0.$$

We remark that the induced streamlines do not give the particle trajectories in the real computation; they only characterize the geometric structure of the velocity field $\mathbf{u}(t)$ for a fixed physical time t . The parameter s does not correspond to the physical time t .

We will generate different streamlines with different initial points $X_0 = (r_0 \cos(2\pi\theta), r_0 \sin(2\pi\theta), z_0)^T$. Since the velocity field \mathbf{u} is now axisymmetric, the geometry of the streamline only depends on (r_0, z_0) . Varying the angular parameter θ only demonstrates the rotational symmetry of the streamlines.

3.4.1. A tornado singularity. Figure 3.7 shows the streamlines induced by the velocity field $\mathbf{u}(t)$ at $t = 1.7 \times 10^{-4}$ in a macroscopic scale (the whole cylinder domain $\mathcal{D}_1 \times [0, 2\pi]$) for different initial points with (a) $(r_0, z_0) = (0.8, 0.01)$ and (b) $(r_0, z_0) = (0.8, 0.1)$. The velocity field resembles that of a tornado spinning around the symmetry axis (the green pole). If the streamline starts near the “ground” ($z = 0$) as in Figure 3.7(a), it will first travel towards the symmetry axis, then move upward towards the “ceiling” ($z = 1/2$), and at last turn outward away from the symmetry axis. In the meanwhile, it spins around the symmetry axis. On the other hand, if the initial point is higher (in the z coordinate) as in Figure 3.7(b), the streamline will not get very close the symmetry axis. Instead, it will travel in an “inward-upward-outward-downward” cycle in the rz -coordinates and, in the mean time, circle around the symmetry axis.

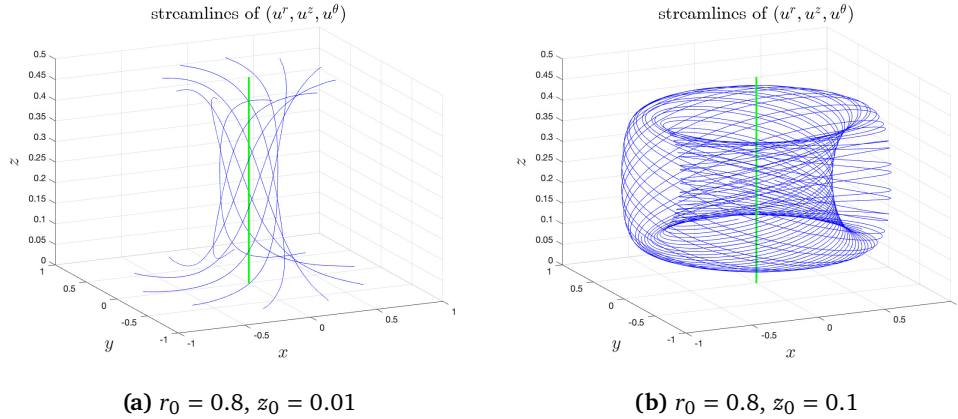


Figure 3.7: The streamlines of $(u^r(t), u^\theta(t), u^z(t))$ at time $t = 1.7 \times 10^{-4}$ with initial points given by (a) $(r_0, z_0) = (0.8, 0.01)$ and (b) $(r_0, z_0) = (0.8, 0.1)$. The green pole is the symmetry axis $r = 0$.

Next, we take a closer look at the blowup region near the sharp front. Figure 3.8 shows the streamlines at time $t = 1.7 \times 10^{-4}$ for different initial points near the maximum location $(R(t), Z(t))$ of $u_1(t)$. The red ring represents the location of $(R(t), Z(t))$, and the green pole is the symmetry axis $r = 0$. The 3 settings of (r_0, z_0) are as follows.

- (a) $(r_0, z_0) = (2R(t), 0.01Z(t))$. The streamline starts near the “ground” $z = 0$ and below the red ring $(R(t), Z(t))$. It first travels towards the symmetry axis and then travels upward away from $z = 0$. The spinning is weak since $u^\theta = ru_1$ is small in the corresponding region.
- (b) $(r_0, z_0) = (1.05R(t), 2Z(t))$. The streamline starts right above the ring $(R(t), Z(t))$. It gets trapped in a local region, oscillating and spinning around the symmetry axis periodically. The spinning is strong.
- (c) $(r_0, z_0) = (1.5R(t), 3Z(t))$. The streamline starts even higher and away from the ring $(R(t), Z(t))$. It spins upward and outward, traveling away from the blowup region.

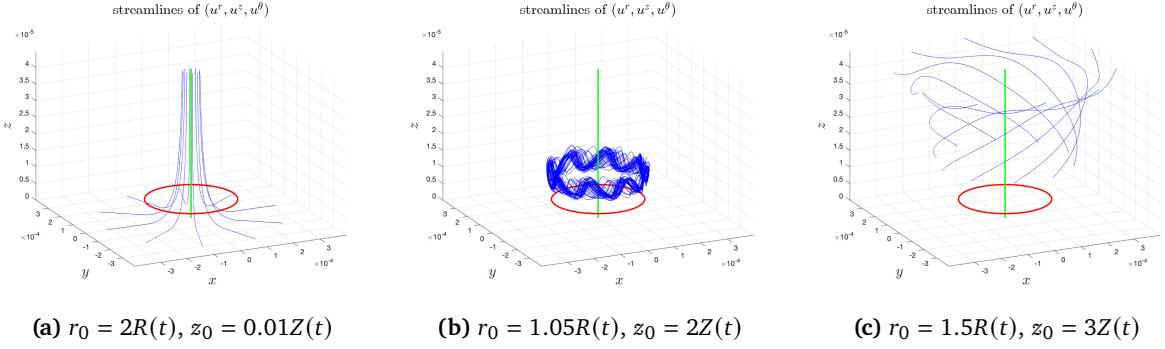


Figure 3.8: The streamlines of $(u^r(t), u^\theta(t), u^z(t))$ at time $t = 1.7 \times 10^{-4}$ with initial points given by (a) $(r_0, z_0) = (2R(t), 0.01Z(t))$, (b) $(r_0, z_0) = (1.05R(t), 2Z(t))$ and (c) $(r_0, z_0) = (1.5R(t), 3Z(t))$. $(R(t), Z(t))$ is the maximum location of $u_1(t)$, indicated by the red ring. The green pole is the symmetry axis $r = 0$.

3.4.2. The 2D flow. To understand the phenomena in the blowup region as shown in Figure 3.8, we look at the 2D velocity field (u^r, u^z) in the computational domain \mathcal{D}_1 . Figure 3.9(a) shows the vector field of $(u^r(t), u^z(t))$ in a local microscopic domain $[0, R_b] \times [0, Z_b]$, where $R_b = 2.5R(t) \approx 3.97 \times 10^{-4}$ and $Z_b = 8Z(t) = 4.50 \times 10^{-5}$. The domain has been rescaled in the figure for better visualization. Figure 3.9(b) is a schematic for the vector field in Figure 3.9(a).

We can see that the streamline below $(R(t), Z(t))$ first travels towards $r = 0$ and then move upward away from $z = 0$, bypassing the sharp front near $(R(t), Z(t))$, which again demonstrates the “two-phase” feature of the flow. As the flow gets close to $r = 0$, the strong axial velocity u^z transports u_1 from near $z = 0$ upward along the z direction. Due to the odd symmetry of u_1 , the angular velocity $u^\theta = ru^1$ is almost 0 in the region near $z = 0$. As a consequence, the upward stream dynamically generates a vacuum region between the sharp front of u_1 and the symmetry axis $r = 0$. This vacuum region resembles the calm eye of a tornado, an area of relatively low wind speed near the center of the vortex. This explains why the streamlines almost do not spin around the symmetry axis in this region, as illustrated in Figure 3.8(a).

Moreover, the velocity field $(u^r(t), u^z(t))$ forms a closed circle right above $(R(t), Z(t))$ as illustrated in Figure 3.9(b). The corresponding streamline is hence trapped in the circle region in the rz -plane. Since u_1 is large in this region (see Figure 3.5(a) and use the red point as a reference), the fluid spins fast around the symmetry axis $r = 0$. Consequently, the corresponding streamline travels fast inside a 3D torus surrounding the symmetry axis. This explains the oscillating and circling in Figure 3.8(b). This local circle structure of the 2D velocity field is critical in stabilizing the blowup process, as it keeps the major profiles of u_1, ω_1 traveling towards the origin instead of being pushed upward.

The velocity field $(u^r(t), u^z(t))$ can also explain the sharp structures of u_1, ω_1 in their local profiles (as shown in Figure 3.5(a),(b)). Figure 3.10 shows the level sets of u^r, u^z at $t = 1.7 \times 10^{-4}$. One can see that the radial velocity u^r has a strong shearing layer below $(R(t), Z(t))$ (the red point). This shearing contributes to the sharp gradient of u_1 in the z direction (e.g., see Figure 3.5(a)). Similarly, the axial velocity u^z also has a strong shearing layer close to the point $(R(t), Z(t))$. This shearing explains the sharp front of u_1 in the r direction. We will also explain in Section 6.6 the formation of a sharp front in the r direction from a different perspective.

3.5. Understanding the blowup mechanism. In this subsection, we gain further understanding of the potential blowup by examining several critical factors that lead to a sustainable blowup solution.

3.5.1. Vortex dipoles and hyperbolic flow. Though we have only shown numerical results in the half-period domain $\mathcal{D}_1 = \{(r, z); 0 \leq r \leq 1, 0 \leq z \leq 1/2\}$, one should keep in mind that the real

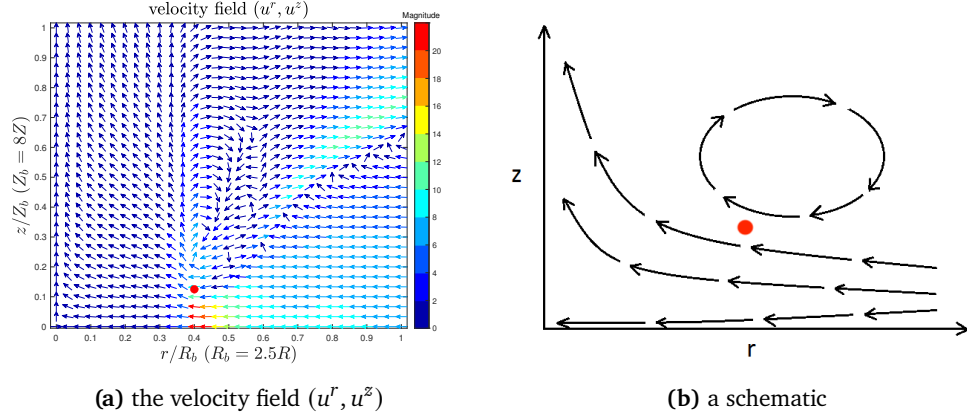


Figure 3.9: (a) The velocity field $(u^r(t), u^z(t))$ near the maximum location $(R(t), Z(t))$ of $u_1(t)$ (the red point) at $t = 1.7 \times 10^{-4}$. The color corresponds to the magnitude of $\sqrt{(u^r)^2 + (u^z)^2}$. The size of the domain has been rescaled. (b) A schematic of the vector field near the point $(R(t), Z(t))$.

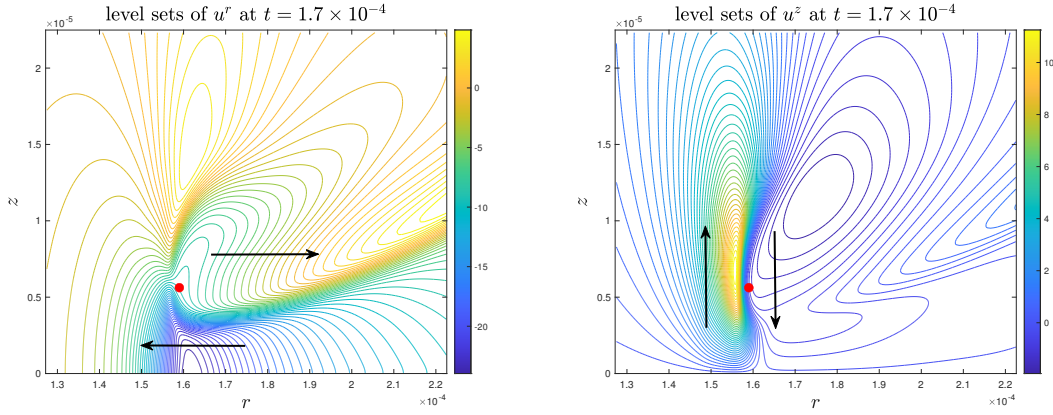


Figure 3.10: The level sets of u^r (left) and u^z (right) at $t = 1.7 \times 10^{-4}$. The red point is the maximum location $(R(t), Z(t))$ of $u_1(t)$.

meaningful physics happens in the whole period $\{(r, z); 0 \leq r \leq 1, -1/2 \leq z \leq 1/2\}$. Moreover, the 2D velocity field (u^r, u^θ) can be extended to the negative r plane as an even function of r . The odd symmetry (in z) of the initial data of ω_1 constitutes to a dipole structure of the angular vorticity ω^θ , which then induces a hyperbolic flow in the rz -plane with a pair of antisymmetric (with respect to z) local circulations. This pair of antisymmetric convective circulations is the cornerstone of our blowup scenario, as it has the desirable property of pushing the solution near $z = 0$ towards $r = 0$.

Figure 3.11 presents the dipole structure of the initial data ω_1^0 in a local symmetric region $(r, z) \in [0, 3 \times 10^{-3}] \times [-3 \times 10^{-4}, 3 \times 10^{-4}]$ and the hyperbolic velocity field induced by it. The negative radial velocity near $z = 0$ induced by the antisymmetric vortex dipoles pushes the solution towards $r = 0$, which is one of the driving mechanisms for a singularity on the symmetry axis. However, we also need another mechanism that squeezes the solution towards $z = 0$, so that it can be driven by the inward velocity. Otherwise, the upward velocity away from $z = 0$ may destroy the blowup trend. This critical squeezing mechanism comes from the odd symmetry of u_1 .

3.5.2. The odd symmetry and sharp gradient of u_1 . The odd symmetry of u_1 is not required for ω_1 to be odd at $z = 0$. The reason we construct u_1 to be an odd function of z is that it ensures that u_1^2 has a large gradient in the z direction near $z = 0$.

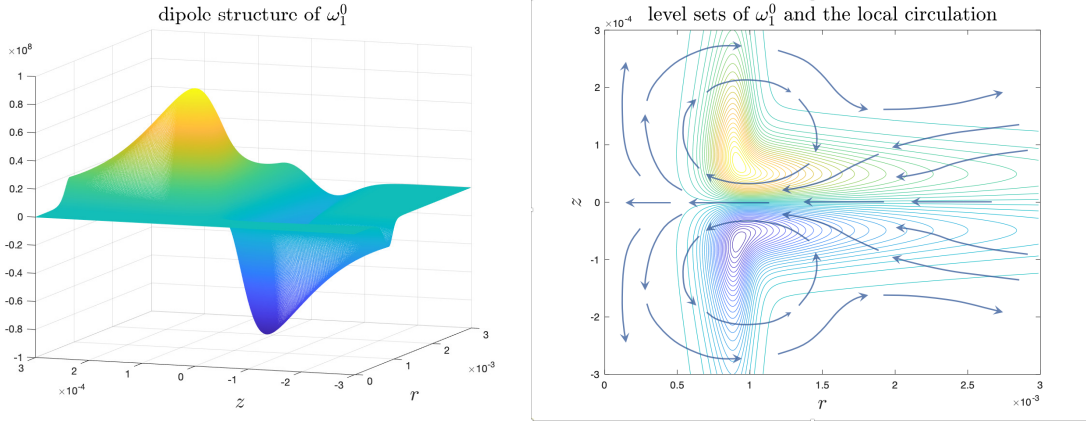


Figure 3.11: The dipole structure of the initial data ω_1^0 and the induced local velocity field.

It is clear from the ω_1 equation (2.3b) that the driving force for ω_1 to blow up is the vortex stretching term $2(u_1^2)_z$. The odd symmetry of u_1 ensures that $u_1(r, 0, t) = 0$ for all $t \geq 0$. Therefore, $(u_1^2)_z$ is positive and large somewhere between $z = Z(t)$ and $z = 0$, which drives ω_1 to grow fast near $z = 0$. The growth of ω_1 then feeds to the growth of u^r (in absolute value) around $z = 0$, as a stronger dipole structure of the angular vorticity ω^θ induces a stronger inward flow in between the dipole (as demonstrated in Figure 3.11). Note that u^r being negative means $\psi_{1,z} = -u^r/r$ is positive, and the growth of u^r around $z = 0$ implies the growth of $\psi_{1,z}$ there, especially near $r = R(t)$. This in turn contributes to the rapid growth of u_1 in the critical region near $z = 0$ through the vortex stretching term $2\psi_{1,z}u_1$ in the u_1 equation (2.3a). Moreover, since $\psi_1 = 0$ along $z = 0$ (by the odd condition), the Poisson equation (2.3c) can be approximated by $\psi_{1,zz} \approx -\omega_1$ near $z = 0$. This means that $\psi_{1,z}$, as a function of z , achieves its local maximum in a neighborhood of $z = 0$ where $\text{sign}(\omega_1) = \text{sign}(z)$. The rapid growth of $\psi_{1,z}$ and the nonlinear vortex stretching term $2\psi_{1,z}u_1$ in the u_1 equation induce a traveling wave for u_1 propagating towards $z = 0$, which drags the maximum location of u_1 towards $z = 0$. The traveling wave is so strong that it overcomes the stabilizing effect of advection along the z direction, which pushes the flow upward away from $z = 0$. The fact that the maximum location of u_1 traveling towards $z = 0$ generates an even sharper gradient of u_1^2 in the z direction. The whole coupling mechanism above forms a positive feedback loop,

$$(u_1^2)_z \uparrow \implies \omega_1 \uparrow \implies \psi_{1,z} \uparrow \implies u_1 \uparrow \implies (u_1^2)_z \uparrow, \quad (3.2)$$

that leads to a sustainable blowup solution shrinking towards $z = 0$ and traveling towards $r = 0$.

To trigger this mechanism, it is important that the initial data have the proper symmetry and a strong alignment between u_1 and ω_1 as we stated in Section 2.3. The maximum location of ω_1 should align with the location where $u_{1,z}$ is positive and large, which is slightly lower (in z) than the maximum location of u_1 . This is one of the guiding principles in the construction of our initial data.

Figure 3.12 demonstrates the alignment between $\psi_{1,z}$ and u_1 . Figure 3.12(b) shows the cross section of $u_1, \psi_{1,z}$ in the z direction through $(R(t), Z(t))$ at $t = 1.7 \times 10^{-4}$. We can see that $\psi_{1,z}(R(t), z, t)$ is monotonically decreasing for $z \in [0, 2Z(t)]$ and relatively flat for $z \in [0, 0.5Z(t)]$. Moreover, $\psi_{1,z}$ is large, positive, and comparable to u_1 in magnitude, which leads to the rapid growth of u_1 and pushes $Z(t)$ moving towards $z = 0$. Figure 3.12(c) shows the alignment ratio $\psi_{1,z}(R(t), Z(t), t)/u_1(R(t), Z(t), t)$, i.e. the alignment between $\psi_{1,z}$ and u_1 at the maximum location of u_1 . One can see that the ratio $\psi_{1,z}/u_1$ settles down to a stable value at $(R(t), Z(t))$ in the stable phase which is characterized by the time interval $[1.6 \times 10^{-4}, 1.76 \times 10^{-4}]$; that is $\psi_{1,z}(R(t), Z(t), t) \sim u_1(R(t), Z(t), t)$ in the stable phase. Consequently, the vortex stretching term in the u_1 equation is formally quadratic at the maximum

location of u_1 if we ignore the small viscosity:

$$\frac{d}{dt}u_{1,\max} \approx u_{1,\max}^2,$$

which implies that maximum u_1 should blow up like $(T - t)^{-1}$ for some finite time T . We will see more clearly this observation in Section 6.

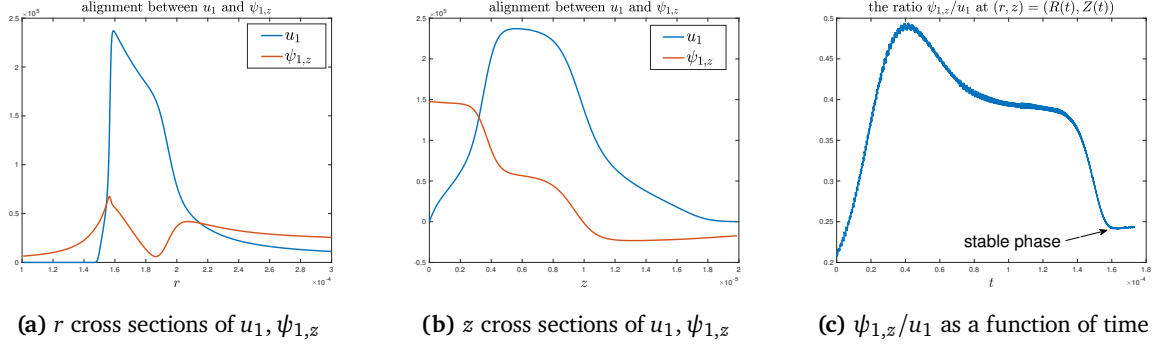


Figure 3.12: The alignment between u_1 and $\psi_{1,z}$.

3.5.3. Two scales. We have observed in Subsection 3.2 that the maximum location $(R(t), Z(t))$ of u_1 travels towards the origin with different rates in the two directions. The decrease of $R(t)$ is a consequence of the inward velocity field near $z = 0$, while the decrease of $Z(t)$ is due to the effect of the vortex stretching term $2\psi_{1,z}u_1$ with $\psi_{1,z}(R(t), z, t)$ being a monotonically decreasing function of z near $z = 0$, which induces a traveling wave with a sharp front moving towards $z = 0$. Moreover, the effect of the nonlinear vortex stretching is much stronger than the effect of convection. As a result, $Z(t)$ converges to 0 much faster than $R(t)$ does, which leads to the two separate spatial scales in the solution profiles.

The two-scale phenomenon is not only a consequence of the blowup mechanism in our scenario, it also critically constitutes to the stability of the blowup. The thin structure of u_1 in the z direction ensures that the solution is carried by the inward velocity towards the symmetry axis $r = 0$. If it were not for the two-scale property, the solution would have been pushed upward and then outward by the roundabout flow that is further away from $z = 0$.

In fact, we can easily destroy the two-scale property of the solution by replacing the degenerate diffusion coefficients with a constant diffusion coefficient, namely, we solve the standard Navier–Stokes equations. We will see in Section 5 that, even with a very small constant viscosity coefficient, the standard Navier–Stokes equations will lead to a completely different scenario where the solution has no two-scale structure and does not seem to lead to a finite time blowup.

4. NUMERICAL RESULTS: RESOLUTION STUDY

In this section, we perform resolution study and investigate the convergence property of our numerical methods. In particular, we will study

- (i) the effectiveness of the adaptive mesh (Section 4.1), and
- (ii) the convergence of the solutions when $h_\rho, h_\eta \rightarrow 0$ (Section 4.2).

4.1. Effectiveness of the adaptive mesh. As discussed in Appendix A.1, to effectively compute a potential singularity with finite resolution, it is important that the adaptive mesh well resolves the solution in the whole domain, especially in the most singular region. In this subsection, we study the effectiveness of our adaptive moving mesh.

To see how well the adaptive mesh resolves the solution, we first visualize how it transforms the solution from the rz -plane to the $\rho\eta$ -plane. Figure 4.1(a) shows the function u_1 at $t = 1.75 \times 10^{-4}$ in the original rz -plane. This plot suggests that the singular structure should be a focusing singularity at the original $(r, z) = (0, 0)$. For comparison, Figure 4.1(b) and (c) plot the profile of u_1 at the same time in the $\rho\eta$ -plane from two different angles. It is apparent that our adaptive mesh resolves the potential point-singularity structure of the solution in the (ρ, η) coordinates.

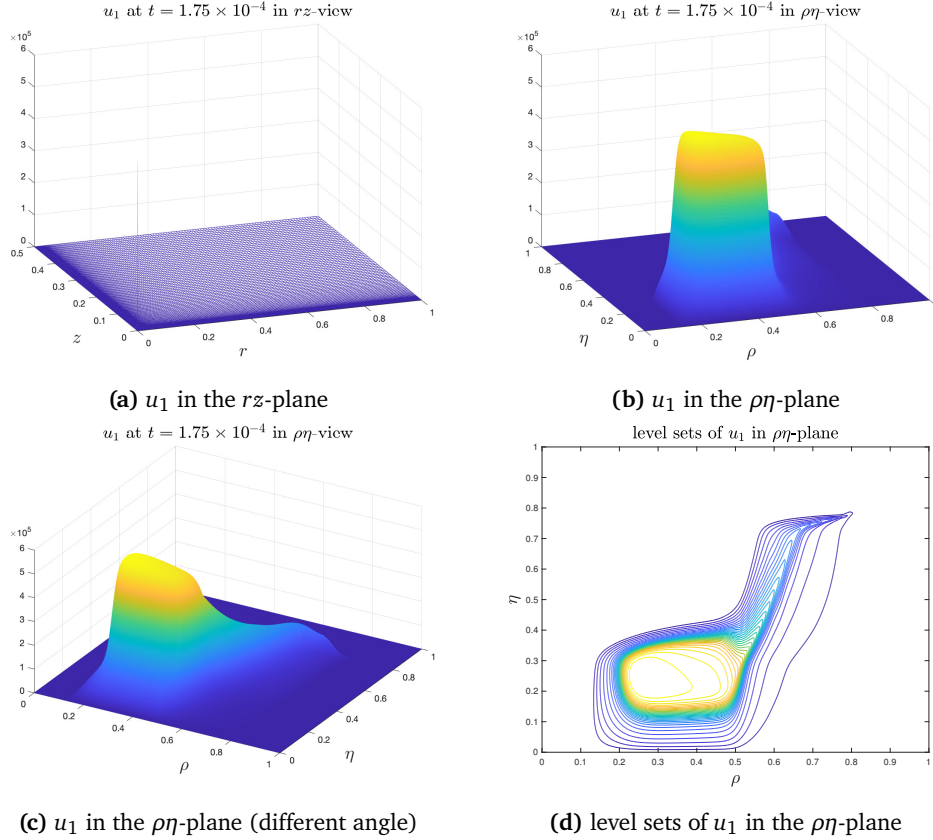


Figure 4.1: The adaptive mesh resolves the solution in the $\rho\eta$ -plane. (a) shows the focusing singularity structure of u_1 at $t = 1.75 \times 10^{-4}$ in the rz -plane on the whole computational domain \mathcal{D}_1 . (b) and (c) plot the profile of u_1 in the $\rho\eta$ -plane from different angles. (d) shows the level sets of u_1 in the $\rho\eta$ -plane.

Figure 4.2 shows the top views of the profiles of u_1, ω_1 in a local domain at $t = 1.75 \times 10^{-4}$. This figure demonstrates how the mesh points are distributed in different phases of the adaptive mesh. The blue numbers indicates the phase labels. By design, the adaptive meshes in phase 1 in both directions, which have the most mesh points, capture the most singular part of the solution.

To obtain a quantitative measure of the maximum resolution power achieved by the adaptive mesh, we define the mesh effectiveness functions $ME_\rho(v), ME_\eta$ with respect to some solution variable v as

$$ME_\rho(v) = \frac{h_\rho v_\rho}{\|v\|_{L^\infty}} = \frac{h_\rho r_\rho v_r}{\|v\|_{L^\infty}}, \quad ME_\eta(v) = \frac{h_\eta v_\eta}{\|v\|_{L^\infty}} = \frac{h_\eta r_\eta v_z}{\|v\|_{L^\infty}},$$

and the corresponding mesh effectiveness measures (MEMs) as

$$ME_{\rho,\infty}(v) = \|ME_\rho(v)\|_{L^\infty}, \quad ME_{\eta,\infty}(v) = \|ME_\eta(v)\|_{L^\infty}.$$

The MEMs quantify the the largest relative growth of a function v in one single mesh cell. The smaller the MEMs are, the better the adaptive mesh resolves the function v . Therefore, we can use these quantities to measure the effectiveness of our adaptive mesh.

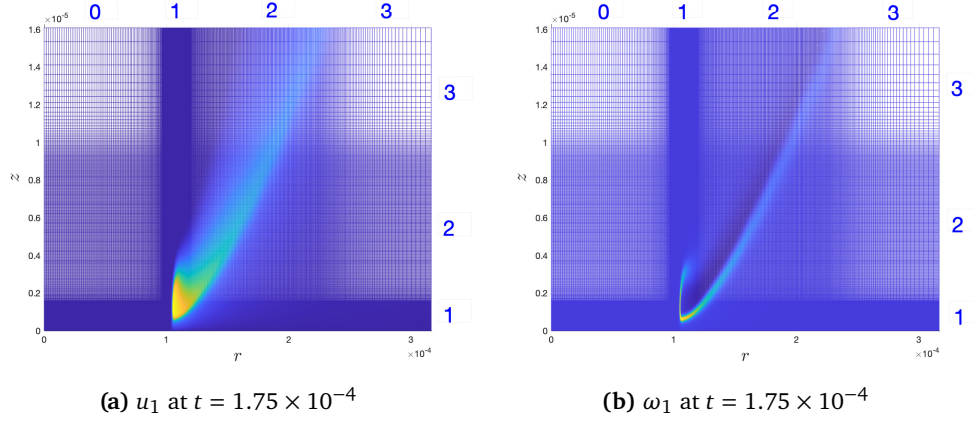


Figure 4.2: The adaptive mesh has different densities in different phases. The blue numbers are the labels of the phases.

Figure 4.3 plots the mesh effectiveness functions of u_1, ω_1 at time 1.75×10^{-4} on the mesh of size $(n, m) = (1024, 512)$. We can see that these functions are all uniformly bounded in absolute value by a small number (e.g., 0.1).

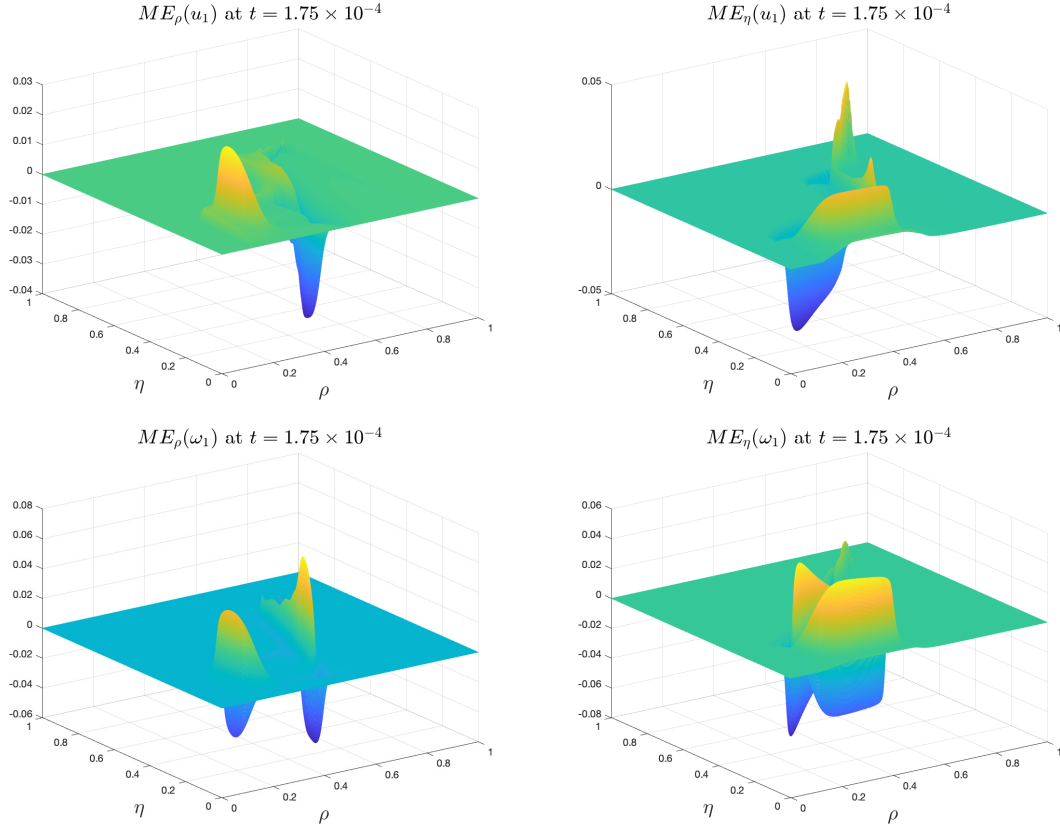


Figure 4.3: First row: the mesh effectiveness functions of u_1 at $t = 1.75 \times 10^{-4}$ with mesh dimension $(n, m) = (1024, 512)$. Second row: the mesh effectiveness functions of ω_1 in the same setting.

Table 4.1 reports the MEMs of u_1, ω_1 at $t = 1.75 \times 10^{-4}$ on meshes of different sizes. The MEMs decrease as the grid sizes h_ρ, h_η decrease, which is expected since the MEMs are proportional to h_ρ, h_η .

Table 4.2 reports the MEMs of u_1, ω_1 at different times with the same mesh size $(n, m) = (1024, 512)$. We can see that the MEMs remain relatively small throughout this time interval, though with an increasing trend (especially $ME_{\rho, \infty}$) in time. From the above study, we can confirm that our adaptive mesh strategy is effective in resolving the potential singularity of the computed solution; it is well adaptive to the solution over the entire computational domain \mathcal{D}_1 , especially in the local region near the sharp front where the solution is most singular.

We remark that though our mesh strategy can resolve the solution well before $t = 1.76 \times 10^{-4}$ in Case 1, it may not work well all the way to the potential singularity time T . The limitation is mostly due to the unbounded growth of the ratio between the two separate scales in the solution as t approaches T . To continue the computation in Case 1 beyond $t = 1.76 \times 10^{-4}$, one may need to use a finer resolution or a more sophisticated adaptive mesh strategy.

Mesh size	MEMs on mesh at $t = 1.75 \times 10^{-4}$			
	$ME_{\rho, \infty}(u_1)$	$ME_{\eta, \infty}(u_1)$	$ME_{\rho, \infty}(\omega_1)$	$ME_{\eta, \infty}(\omega_1)$
512×256	0.086	0.096	0.136	0.116
1024×512	0.038	0.050	0.067	0.066
1536×768	0.026	0.032	0.046	0.041
2048×1024	0.018	0.026	0.033	0.030

Table 4.1: MEMs of u_1, ω_1 at $t = 1.75 \times 10^{-4}$ on the meshes of different sizes.

Time	MEMs on mesh $(n, m) = (1024, 512)$			
	$ME_{\rho, \infty}(u_1)$	$ME_{\eta, \infty}(u_1)$	$ME_{\rho, \infty}(\omega_1)$	$ME_{\eta, \infty}(\omega_1)$
1.7×10^{-4}	0.022	0.042	0.049	0.070
1.73×10^{-4}	0.028	0.047	0.053	0.068
1.74×10^{-4}	0.031	0.041	0.056	0.059
1.75×10^{-4}	0.038	0.050	0.067	0.066
1.76×10^{-4}	0.065	0.059	0.100	0.069

Table 4.2: MEMs of u_1, ω_1 at different times on the mesh of size $(n, m) = (1024, 512)$.

4.2. Resolution study. In this subsection, we perform resolution study on the numerical solutions of the initial-boundary value problem (2.3)–(2.6) at various time instants t and in different cases. We will estimate the relative error of a solution variable f_p computed on the $256p \times 128p$ mesh by comparing it to a reference variable \hat{f} that is computed on a finer mesh at the same time instant. If f_p is a number, the absolute relative error is computed as $e_p = |f_p - \hat{f}|/|\hat{f}|$. If f_p is a spatial function, the reference variable \hat{f} is first interpolated to the mesh on which f is computed. Then the sup-norm relative error is computed as

$$e_p = \frac{\|f_p - \hat{f}\|_{\infty}}{\|\hat{f}\|_{\infty}} \quad \text{if } f \text{ is a scalar function,}$$

$$\text{and } e_p = \frac{\| (f_p^{\theta} - \hat{f}_p^{\theta}, f_p^r - \hat{f}_p^r, f_p^z - \hat{f}_p^z) \|_{\infty}}{\| (\hat{f}_p^{\theta}, \hat{f}_p^r, \hat{f}_p^z) \|_{\infty}} \quad \text{if } f \text{ is a vector function.}$$

The numerical order of the error is computed as

$$\beta_p = \log_{\frac{p}{p-1}} \left(\frac{e_{p-1}}{e_p} \right).$$

For all cases, the reference solution \hat{f} is chosen to be the one computed at the same time instant on the finer mesh of size $256(p+1) \times 128(p+1)$.

4.2.1. *Case 1.* This case is the most fundamental one among all of our computations. We will perform a more thorough resolution study for the computations corresponding to this case. Recall that in Case 1, we do not apply the re-meshed low-pass filter RLPPF.

We first study the sup-norm error of the solution, which is the most straightforward indication of the accuracy of our numerical method. Tables 4.3–4.6 report the sup-norm relative errors and numerical orders of different solution variables at times $t = 1.65 \times 10^{-4}$ and $t = 1.7 \times 10^{-4}$, respectively. The results confirm that our method in Case 1 is at least 2nd-order accurate. We remark that the error in the solution mainly arises from the interpolation error near the sharp front, where the gradient of the solution is largest and becomes larger and larger in time.

Mesh size	Sup-norm relative error at $t = 1.65 \times 10^{-4}$ in Case 1					
	u_1	Order	ω_1	Order	ψ_1	Order
256×512	1.2949×10^{-1}	–	2.7872×10^{-1}	–	2.4290×10^{-2}	–
384×768	4.4825×10^{-2}	2.62	9.8239×10^{-2}	2.57	8.2729×10^{-3}	2.66
512×1024	2.0467×10^{-2}	2.63	4.4789×10^{-2}	2.73	3.8283×10^{-3}	2.68
640×1280	1.1264×10^{-2}	2.68	2.5061×10^{-2}	2.60	1.9905×10^{-3}	2.93
768×1536	7.0304×10^{-3}	2.59	1.5410×10^{-2}	2.67	1.3228×10^{-3}	2.24
896×1792	4.3618×10^{-3}	3.10	9.5333×10^{-3}	3.12	8.2235×10^{-4}	3.08

Table 4.3: Sup-norm relative errors and numerical orders of u_1, ω_1, ψ_1 at $t = 1.65 \times 10^{-4}$ in Case 1.

Mesh size	Sup-norm relative error at $t = 1.65 \times 10^{-4}$ in Case 1					
	u^r	Order	u^z	Order	$\omega = (\omega^\theta, \omega^r, \omega^z)$	Order
256×512	2.3116×10^{-1}	–	6.5401×10^{-2}	–	2.5887×10^{-1}	–
384×768	8.0520×10^{-2}	2.60	2.2632×10^{-2}	2.62	9.1315×10^{-2}	2.57
512×1024	3.6975×10^{-2}	2.71	1.0477×10^{-2}	2.68	4.1456×10^{-2}	2.74
640×1280	2.0084×10^{-2}	2.74	5.7374×10^{-3}	2.70	2.3254×10^{-2}	2.59
768×1536	1.2862×10^{-2}	2.44	3.6477×10^{-3}	2.48	1.4134×10^{-3}	2.73
896×1792	7.9410×10^{-3}	3.13	2.2479×10^{-3}	3.14	8.7579×10^{-3}	3.11

Table 4.4: Sup-norm relative errors and numerical orders of u^r, u^z, ω at $t = 1.65 \times 10^{-4}$ in Case 1.

We can also study the convergence of some variables as functions of time. In particular, we report the convergence of the quantities $\|u_1\|_{L^\infty}$, $\|\omega_1\|_{L^\infty}$, $\|\omega\|_{L^\infty}$, and the kinetic energy E . Here the kinetic energy E is given by

$$E := \frac{1}{2} \int_{\mathcal{D}_1} |\mathbf{u}|^2 \, dx = \frac{1}{2} \int_0^1 \int_0^{1/2} \left(|u^r|^2 + |u^\theta|^2 + |u^z|^2 \right) r \, dr \, dz.$$

Mesh size	Sup-norm relative error at $t = 1.7 \times 10^{-4}$ in Case 1					
	u_1	Order	ω_1	Order	ψ_1	Order
256×512	3.1543×10^{-1}	–	5.7498×10^{-1}	–	6.3176×10^{-2}	–
384×768	1.1080×10^{-1}	2.58	2.1421×10^{-1}	2.44	2.1410×10^{-2}	2.67
512×1024	5.3980×10^{-2}	2.50	1.0487×10^{-1}	2.48	1.0267×10^{-2}	2.55
640×1280	2.8154×10^{-2}	2.92	5.4662×10^{-2}	2.92	5.3087×10^{-3}	2.96
768×1536	1.8674×10^{-2}	2.25	3.6419×10^{-2}	2.23	3.5579×10^{-3}	2.19
896×1792	1.1740×10^{-2}	3.01	2.2894×10^{-2}	3.01	2.2323×10^{-3}	3.02

Table 4.5: Sup-norm relative errors and numerical orders of u_1, ω_1, ψ_1 at $t = 1.7 \times 10^{-4}$ in Case 1.

Mesh size	Sup-norm relative error at $t = 1.7 \times 10^{-4}$ in Case 1					
	u^r	Order	u^z	Order	$\omega = (\omega^\theta, \omega^r, \omega^z)$	Order
256×512	5.1092×10^{-1}	–	1.3200×10^{-1}	–	5.0630×10^{-1}	–
384×768	1.8141×10^{-1}	2.55	4.6313×10^{-2}	2.58	1.8885×10^{-1}	2.43
512×1024	8.8443×10^{-2}	2.50	2.2743×10^{-2}	2.47	9.2927×10^{-2}	2.47
640×1280	4.5596×10^{-2}	2.97	1.2038×10^{-2}	2.85	4.8958×10^{-2}	2.87
768×1536	3.0860×10^{-2}	2.14	7.8363×10^{-3}	2.35	3.2255×10^{-2}	2.29
896×1792	1.9350×10^{-2}	3.03	4.9410×10^{-3}	2.99	2.0271×10^{-2}	3.01

Table 4.6: Sup-norm relative errors and numerical orders of u^r, u^z, ω at $t = 1.7 \times 10^{-4}$ in Case 1.

Since the diffusion term with variable coefficients in (2.1) is given in a conservative form, the kinetic energy is a non-increasing function of time: $E(t_1) \leq E(t_2)$ for $t_2 \geq t_1 \geq 0$. Figures 4.4 and 4.5 plot the relative errors and numerical orders of these quantities as functions of time. The results further confirm that our method is 2nd-order in h_ρ, h_η .

Remark 4.1. There are mainly two types of errors in our computation: one is the discretization error of the numerical scheme, and the other is the interpolation error from one mesh to another when we change our adaptive mesh at certain time instants. Since the solution is quite smooth in the early stage of the computation, the discretization error is small, and the total error may be dominated by the interpolation error. The change of mesh may happen more frequently for the computation with a finer mesh, and thus the total error can even be smaller on a coarser mesh, as we can see in the first row of Figure 4.4. We can only see the expected order of accuracy when the discretization error accumulates to some level such that it dominates the total error.

On the other hand, we also observe an increasing trend in the relative errors of $\|u_1\|_{L^\infty}$, $\|\omega_1\|_{L^\infty}$, and $\|\omega\|_{L^\infty}$, which implies that our numerical method with a fixed mesh size will not work for all time up to the anticipated singularity. As we mentioned in Section 4.1, our adaptive mesh strategy may lose its power to resolve the solution as the two scales in the solution becomes more and more separated. Indeed, the sharp front in the r direction becomes thinner and thinner as t approaches the potential singularity time, which makes it more and more difficult to construct an adaptive mesh with a fixed number of grid points that provides a small approximation error in the entire domain. Therefore, to obtain a well-resolved solution sufficiently close to the potential singularity time, one must use an extremely large number of grid points, which is, unfortunately, beyond the capacity of our current computational resources.

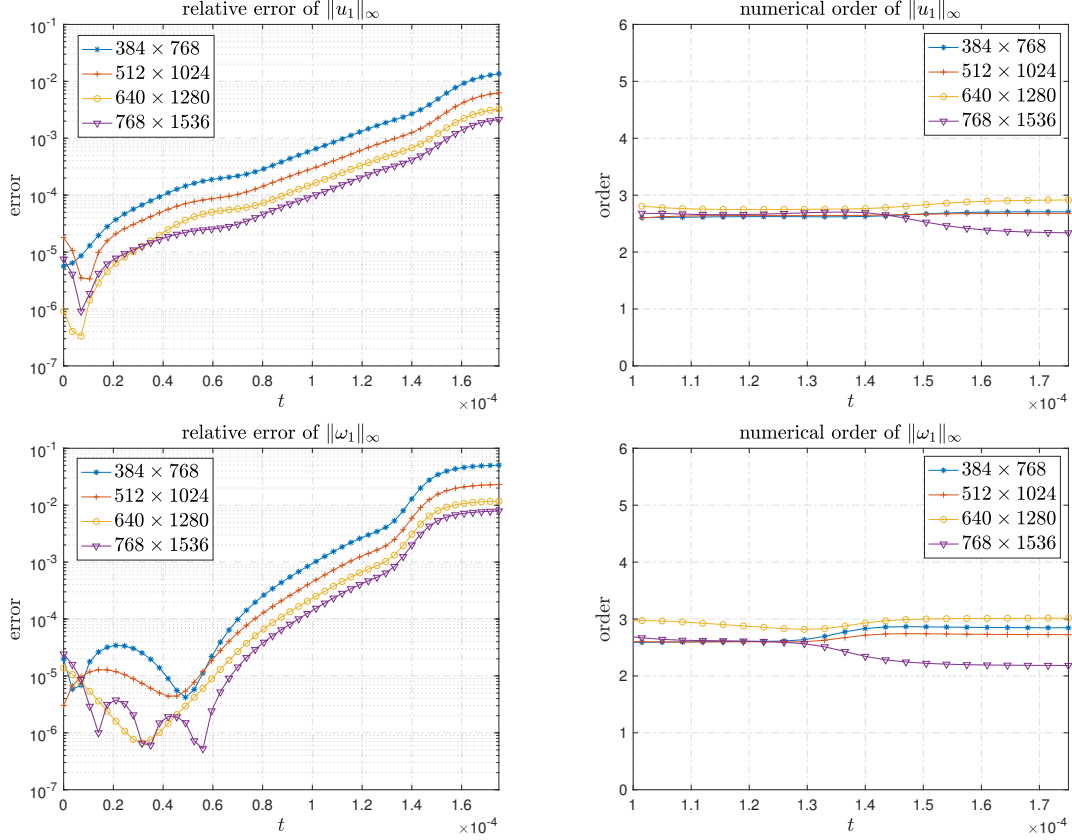


Figure 4.4: First row: relative error and numerical order of $\|u_1(t)\|_{L^\infty}$. Second row: relative error and numerical order of $\|\omega_1(t)\|_{L^\infty}$. The last time instant shown in the figure is $t = 1.76 \times 10^{-4}$.

4.2.2. *Case 2.* Recall that in the Case 2 computation, the only change we make is to replace the variable diffusion coefficients (2.8) by a constant diffusion coefficient μ , so we actually solve the original Navier–Stokes equations. Since the numerical methods in Case 1 and Case 2 are the same, we expect to see similar convergence behaviors of the solutions. Nevertheless, we still perform a resolution study in Case 2 to confirm the 2nd order accuracy of our method, and we only present the results from the case $\nu^r = \nu^z = 10^{-5}$. We remark that the solution in Case 2 evolves in a completely different way; in particular, it does not lead to a finite time blowup. We can thus compute the solution to a much later time. The sup-norm relative errors and numerical orders of u_1, ω_1, ω at $t = 2 \times 10^{-4}$ and $t = 2.5 \times 10^{-4}$ are reported in Tables 4.7 and 4.8, respectively.

4.2.3. *Case 3.* The difference between Case 1 and Case 3 is that we apply the extra re-meshed low-pass filtering RLPF_c^k in Case 3 to smooth out the mild instability that may occur at the tail part of the solution (see Section 7). As mentioned in Appendix A.4, the operator RLPF_c^k introduces an extra error that is also 2nd order in (h_ρ, h_η) . Therefore, the application of RLPF_c^k will not compromise the overall 2nd-order accuracy of our numerical method. Indeed, we have observed a 2nd-order convergence of the solution computed in Case 3 for all choices of k in RLPF_c^k . The convergence behaviors are very similar to those that we have reported for Case 1. To avoid redundancy, we only present the sup-norm relative errors of the solution variables u_1, ω_1, ω computed in Case 3 with $k = 50$ to confirm convergence.

Tables 4.9 and 4.10 report the sup-norm relative errors and numerical orders of u_1, ω_1, ω at $t = 1.65 \times 10^{-4}$ and $t = 1.7 \times 10^{-4}$, respectively. The data show that our numerical method supplemented with the re-meshed low-pass filtering RLPF_c^k is also 2nd-order accurate in (h_ρ, h_η) .

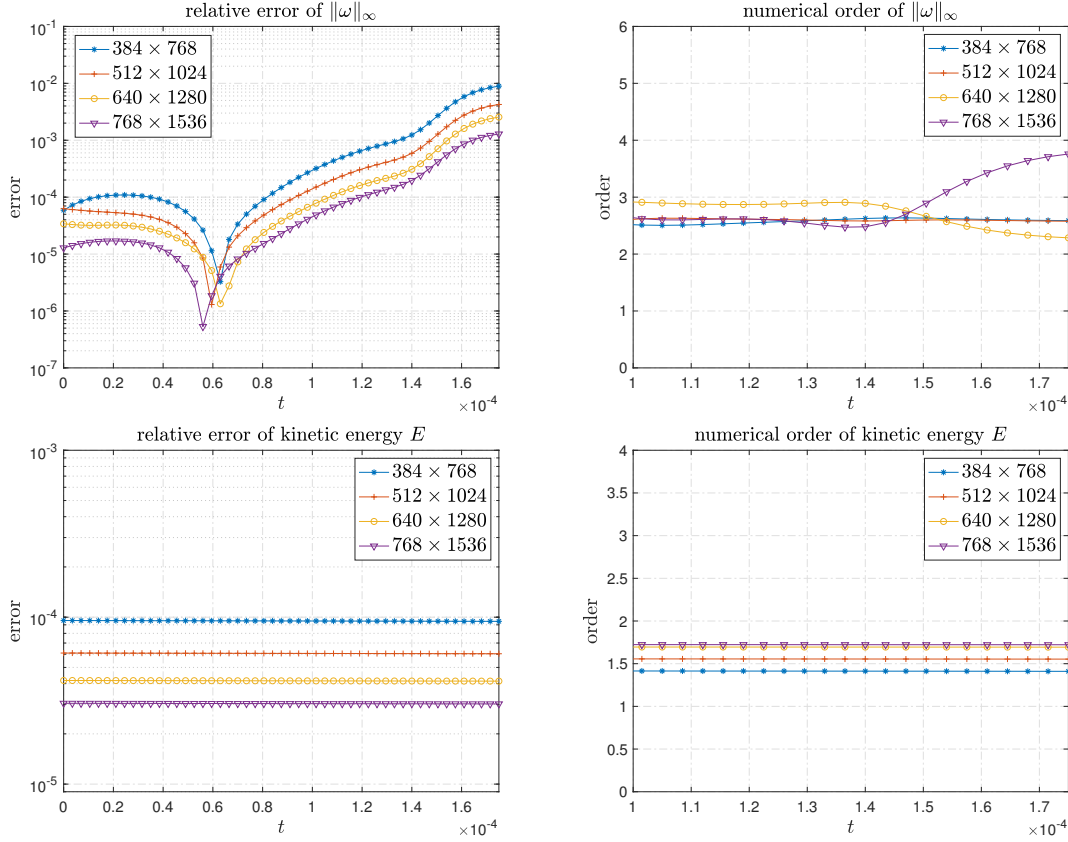


Figure 4.5: First row: relative error and numerical order of $\|\omega(t)\|_{L^\infty}$. Second row: relative error and numerical order of $E(t)$. The last time instant shown in the figure is $t = 1.76 \times 10^{-4}$.

Mesh size	Sup-norm relative error at $t = 2 \times 10^{-4}$ in Case 2					
	u_1	Order	ω_1	Order	ω	Order
256×512	1.6283×10^{-3}	—	2.0004×10^{-3}	—	2.4642×10^{-3}	—
384×768	5.7153×10^{-4}	2.58	7.0144×10^{-4}	2.58	8.6683×10^{-4}	2.57
512×1024	2.6353×10^{-4}	2.69	3.2570×10^{-4}	2.67	3.9648×10^{-4}	2.72
640×1280	1.4402×10^{-4}	2.70	1.7634×10^{-4}	2.75	2.1780×10^{-4}	2.68
768×1536	8.6198×10^{-5}	2.82	1.0735×10^{-4}	2.72	1.2873×10^{-4}	2.88
896×1792	5.5432×10^{-5}	2.86	6.8494×10^{-5}	2.91	8.3230×10^{-5}	2.83

Table 4.7: Sup-norm relative errors and numerical orders of u_1, ω_1, ω at $t = 2 \times 10^{-4}$ in Case 2.

5. COMPARISON WITH THE ORIGINAL NAVIER-STOKES EQUATIONS

In this section, we compare the solution to the equations (2.3) with the variable diffusion coefficients (2.8) (Case 1) and the solution to the original Navier-Stokes Equations (Case 2) using the same initial-boundary conditions (2.5), (2.6). This comparison will explain why the degeneracy of the variable diffusion coefficients is crucial for the solution to develop a potential finite time singularity. In fact, we observe that the Navier-Stokes equations with a constant diffusion coefficient will destroy the critical two-scale feature of the solution and eventually prevent the finite time blowup.

Mesh size	Sup-norm relative error at $t = 2.5 \times 10^{-4}$ in Case 2					
	u_1	Order	ω_1	Order	ω	Order
256×512	1.3726×10^{-3}	–	1.6971×10^{-3}	–	2.4229×10^{-3}	–
384×768	4.7140×10^{-4}	2.63	5.8979×10^{-4}	2.61	8.3826×10^{-4}	2.58
512×1024	2.1351×10^{-4}	2.75	2.7200×10^{-4}	2.69	3.7361×10^{-4}	2.85
640×1280	1.2303×10^{-4}	2.47	1.5144×10^{-4}	2.62	2.0920×10^{-4}	2.60
768×1536	7.1537×10^{-5}	2.97	9.0012×10^{-5}	2.85	1.2082×10^{-4}	3.01
896×1792	4.6082×10^{-5}	2.85	5.7634×10^{-5}	2.89	7.8138×10^{-5}	2.83

Table 4.8: Sup-norm relative errors and numerical orders of u_1, ω_1, ω at $t = 2.5 \times 10^{-4}$ in Case 2.

Mesh size	Sup-norm relative error at $t = 1.65 \times 10^{-4}$ in Case 3					
	u_1	Order	ω_1	Order	ω	Order
256×512	1.9272×10^{-1}	–	4.1490×10^{-1}	–	3.8716×10^{-1}	–
384×768	6.8074×10^{-2}	2.57	1.5153×10^{-1}	2.48	1.4241×10^{-1}	2.46
512×1024	3.1513×10^{-2}	2.68	7.0667×10^{-2}	2.65	6.5744×10^{-2}	2.69
640×1280	1.7593×10^{-2}	2.61	4.0146×10^{-2}	2.53	3.7524×10^{-2}	2.51
768×1536	1.0274×10^{-2}	2.95	2.2826×10^{-2}	3.10	2.1019×10^{-2}	3.18
896×1792	6.6072×10^{-3}	2.86	1.4779×10^{-3}	2.82	1.3672×10^{-2}	2.79

Table 4.9: Sup-norm relative errors and numerical orders of u_1, ω_1, ω at $t = 1.65 \times 10^{-4}$ in Case 3.

Mesh size	Sup-norm relative error at $t = 1.7 \times 10^{-4}$ in Case 3					
	u_1	Order	ω_1	Order	ω	Order
256×512	4.9296×10^{-1}	–	8.1229×10^{-1}	–	7.1310×10^{-1}	–
384×768	1.9482×10^{-1}	2.28	3.7147×10^{-1}	1.93	3.2991×10^{-1}	1.90
512×1024	9.4778×10^{-2}	2.50	1.8453×10^{-1}	2.43	1.6458×10^{-1}	2.42
640×1280	5.1658×10^{-2}	2.72	1.0106×10^{-2}	2.70	9.0886×10^{-2}	2.66
768×1536	3.2492×10^{-2}	2.54	6.3768×10^{-2}	2.53	5.7004×10^{-2}	2.56
896×1792	2.0879×10^{-2}	2.87	4.1045×10^{-2}	2.86	3.6625×10^{-2}	2.87

Table 4.10: Sup-norm relative errors and numerical orders of u_1, ω_1, ω at $t = 1.7 \times 10^{-4}$ in Case 3.

5.1. Profile evolution in Case 2. In Section 3, we studied the evolution of the solution in Case 1, and observed a stable blowup with a two-scale feature. Here, we investigate how the solution evolves differently when the degenerate diffusion coefficients ν^r, ν^z are replaced by a constant μ . As an illustration, we will focus our study on the case where $\mu = 10^{-5}$. In what follows, Case 2 refers to the computation of the Navier–Stokes equations with constant diffusion coefficient $\mu = 10^{-5}$ without further clarification. Similar phenomena have been observed in Case 2 when μ takes different values.

Figure (5.1) demonstrates the evolution of the solution in Case 2 from $t = 1.6 \times 10^{-4}$ to $t = 2 \times 10^{-4}$. One should notice the obvious difference in behavior between the solution in Case 1 and that in Case 2 when comparing Figure (5.1) with Figure (3.1). Below we list some of our observations.

- Unlike in Case 1, the computation in Case 2 can be continued to a much later time, and the solution still remains quite smooth.

- The solution does not change much from $t = 1.6 \times 10^{-4}$ to $t = 2 \times 10^{-4}$. In particular, it does not develop a two-scale spatial structure. Instead, it maintains a profile with a single scale that is comparable to $R(t)$, the distance between the maximum location of u_1 and the symmetry axis $r = 0$. Moreover, the profile of u_1 does not form a sharp gradient in the z direction or a sharp front in the r direction, and the profile of ω_1 does not develop a thin structure.
- The maximums of the solution u_1 and ω_1 only grow modestly in the early stage and eventually decrease in the late stage. From $t = 0$ to $t = 2 \times 10^{-4}$, $\|u_1\|_{L^\infty}$ increases only by a factor of 2.34, and $\|\omega_1\|_{L^\infty}$ increases only by a factor of 3.67.

These observations suggest that the solution in Case 2 does not develop a finite-time blowup, at least not in the same way as in Case 1. The main reason for such difference in behavior is that the diffusion term with a constant diffusion coefficient is so strong that it regularizes the smaller scale $Z(t)$ in the two-scale solution profile that we observed in Section 3.5, thus destroys the critical blowup mechanism. We will explain in Section 6.6 why the degenerate diffusion coefficient is crucial for a two-scale blowup to appear and persist.

Figure (5.2) compares the trajectories of $(R(t), Z(t))$ and the ratios $R(t)/Z(t)$ in Case 1 for $t \in [0, 1.76 \times 10^{-4}]$ and in Case 2 for $t \in [0, 3 \times 10^{-4}]$. We can see that, due to the effect of the stronger diffusion, the point $(R(t), Z(t))$ in Case 2 does not travel towards the symmetry axis $r = 0$ or towards the symmetry plane $z = 0$ as fast as in Case 1. The ratio $R(t)/Z(t)$ in Case 2 does not blow up rapidly; instead, the two coordinates remain comparable to each other. This again confirms that the solution does not develop the critical two-scale feature in Case 2. More interestingly, the red trajectory turns upward after some time, suggesting that there will be no blowup focusing at the origin $(r, z) = (0, 0)$ in Case 2. This is consistent with our discussion in Section 3.5 that when there is no two-scale feature, the main profile of the solution will eventually be pushed away from the “ground” $z = 0$ by the upward flow. As a result, the critical blowup mechanism in our scenario will be destroyed.

5.2. Growth of some key quantities in Case 2. To further illustrate that the solution will remain regular in Case 2, we directly study the growth of different solution variables. Figure 5.3 plots the maximums of u_1 , ω_1 , $|\omega|$ as functions of time. We can see that these quantities do not increase rapidly as in Case 1 (compared to the dramatic growth shown in Figure 3.6); moreover, they all start to decrease after some time. Recall that for the Navier–Stokes equations, the Beale–Kato–Majda criterion (see Section 3.3) states that the solution develops a singularity at some finite time T if and only if $\int_0^T \|\omega\|_{L^\infty} dt = +\infty$. From Figure 5.3 we can see that the maximum vorticity $\|\omega\|_{L^\infty}$ tends to remain bounded, at least for the duration of our computation. This observation strongly suggests that the solution to the equations (2.3) with a constant diffusion coefficient (namely the Navier–Stokes equations) will not blow up under the initial-boundary conditions (2.5), (2.6).

To understand why the maximum of u_1 does not rise rapidly and eventually drops in the later stage in Case 2, we study the competition between the vortex stretching and the diffusion. Since $2u_1$ is the leading order part of the axial vorticity $\omega^z = 2u_1 + ru^r$ for r near 0, the forcing term $2\psi_{1,z}u_1$ in the u_1 equation (2.3) can be considered as a vortex stretching term. This term is the driving force for the growth of u_1 . On the contrary, the diffusion term f_{u_1} (given by (2.4a)), which is always negative at $(R(t), Z(t))$, damps the maximum of u_1 . If the vortex stretching dominates the diffusion near $(R(t), Z(t))$, $\|u_1\|_{L^\infty}$ should grow; otherwise, $\|u_1\|_{L^\infty}$ will drop.

In Figure 5.4 we plot the relative magnitudes of the vortex stretching $2\psi_{1,z}$ and the diffusion $|f_{u_1}|/u_1$ at $(R(t), Z(t))$ in Case 1 (left) and in Case 2 (right). It is clear that the vortex stretching keeps growing and always dominates the diffusion term in the u_1 equations at $(R(t), Z(t))$ in Case 1; thus we observe a rapid growth of $\|u_1\|_{L^\infty}$ in time. This is the consequence of (i) the good alignment between $\psi_{1,z}$ and u_1 that relies on the thin structure (the smaller scale) of the solution in the z direction as described in Section 3.5 and (ii) the fact that the diffusion coefficients are degenerate at the origin. On the

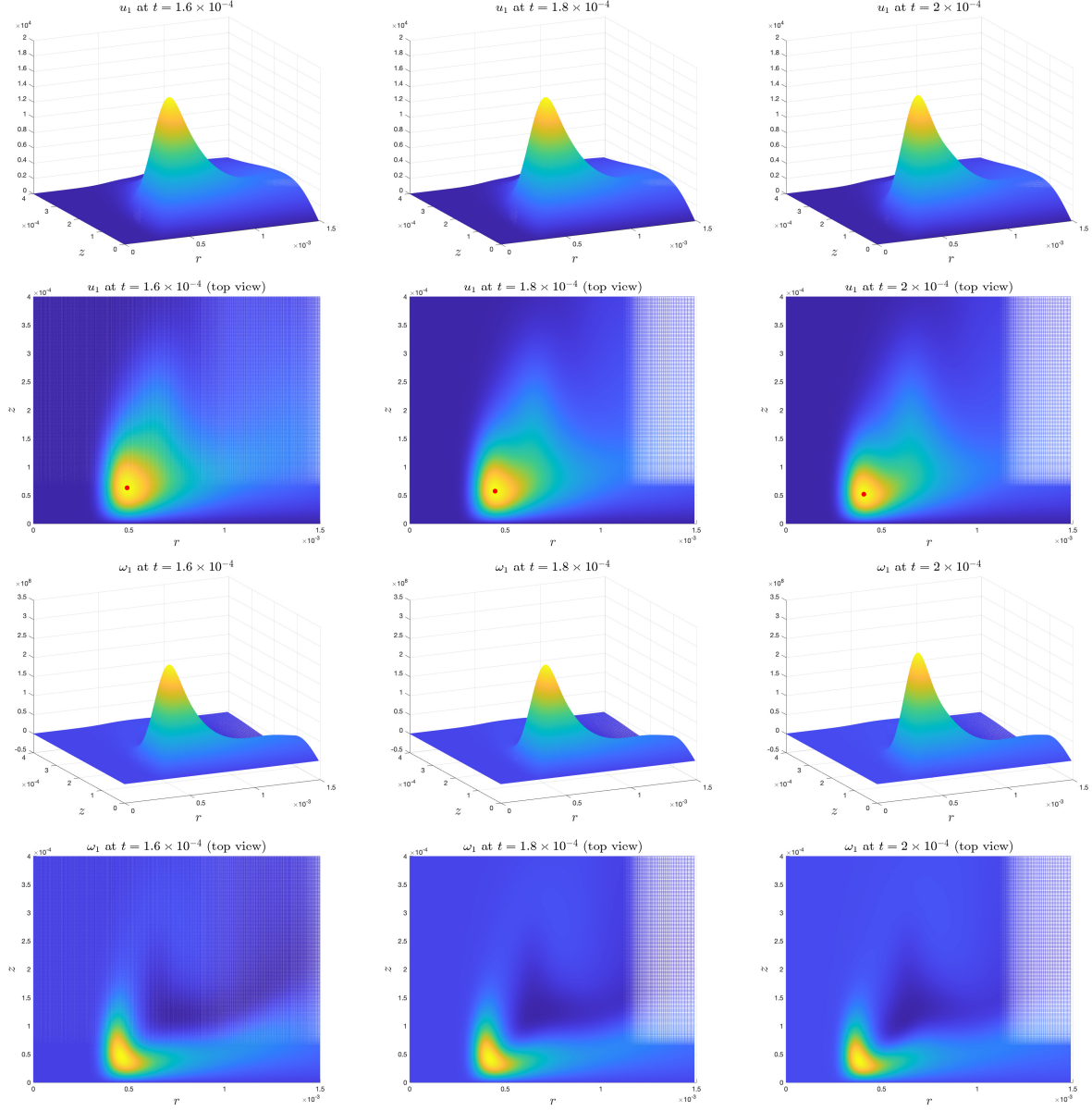


Figure 5.1: The evolution of the profiles of u_1 (row 1 and 2) and ω_1 (row 3 and 4) in Case 2 with $\nu^r = \nu^z = 10^{-5}$. Line 1 and 3 are the profiles of u_1, ω_1 at three different times; Line 2 and 4 are the corresponding top-views. The red dot is the location of maximum u_1 .

contrary, we observe in Case 2 that the relative strength of the vortex stretching starts to decrease after some time and is dominated by the diffusion term in later time, which leads to the decrease of $\|u_1\|_{L^\infty}$. This is caused by the strong diffusion from two aspects. On the one hand, if the blowup mechanism in Section 3.5 tries to generate a thinner scale in the solution, then the diffusion with a constant/non-degenerate coefficient will become too strong for the smaller scale to survive, and thus the alignment between $\psi_{1,z}$ and u_1 is not sustainable. On the other hand, if the solution does not develop a two-scale structure, $\psi_{1,z}$ and u_1 cannot develop a strong alignment for the coupling mechanism (3.2) to last. This dilemma prevents a sustainable blowup to occur in Case 2.

We remark that we have carried out computations in Case 2 with different values of μ in the range $[10^{-7}, 10^{-4}]$, and we have qualitatively similar observations in all trials: there is no sign of finite-time

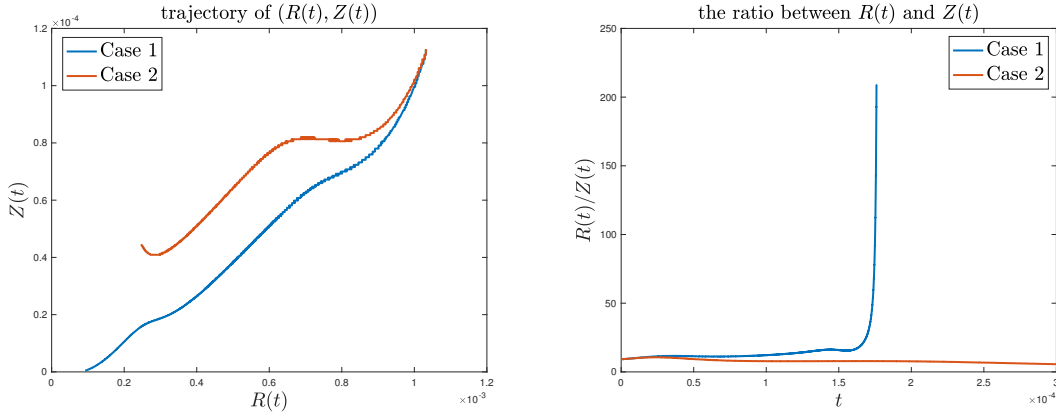


Figure 5.2: Left: trajectories of $(R(t), Z(t))$ in Case 1 and in Case 2. Right: ratios between $R(t), Z(t)$ in Case 1 and in Case 2. Blue curves: Case 1 for $t \in [0, 1.76 \times 10^{-4}]$. Red curves: Case 2 for $t \in [0, 3 \times 10^{-4}]$.

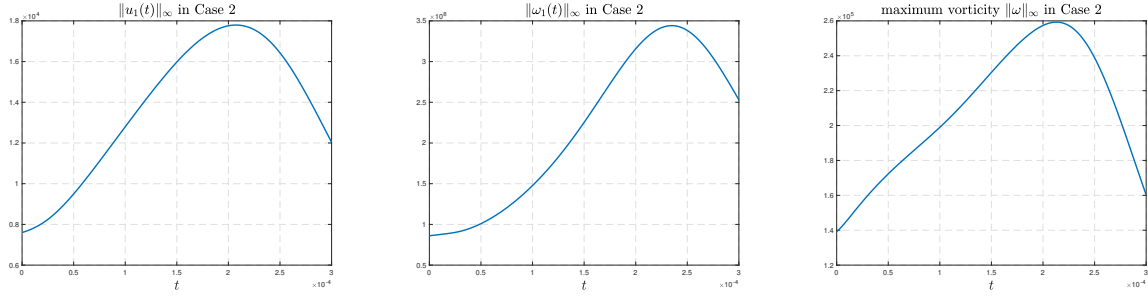


Figure 5.3: The values of $\|u_1\|_{L^\infty}$, $\|\omega_1\|_{L^\infty}$ and $\|\omega\|_{L^\infty}$ as functions of time in Case 2.

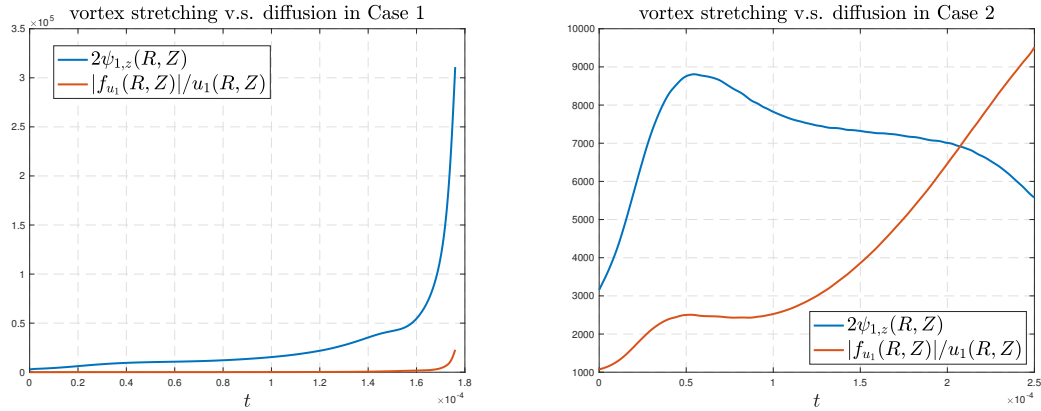


Figure 5.4: The relative magnitudes of the vortex stretching $2\psi_{1,z}$ and the diffusion $|f_{u_1}|/u_1$ at the point $(R(t), Z(t))$ in Case 1 (left) and in Case 2 (right).

blowup for all tested values of μ . For a smaller μ , the solution in Case 2 in the early stage of the computation is very similar the solution in Case 1, and a two-scale feature seems to develop. However, the diffusion with a constant coefficient will eventually take dominance and eliminate the potential two-scale blowup, and the solution starts to drop afterwards. If μ is even smaller ($\mu < 10^{-7}$), the diffusion term will be too weak to regularize the sharp fronts in the early stage of the computation and cannot effectively control the mild instability in the intermediate field and far field where the mesh

is not as dense as in the near field. The solution quickly becomes under-resolved. It is still unclear whether the solution to the original 3D axisymmetric Navier–Stokes equations can develop a focusing blowup at the symmetry axis in a different manner when μ is sufficiently small. Yet we conjecture that this cannot happen in the two-scale manner described in Case 1.

5.3. On the diffusion effect. We remark that the driving mechanism for the potential finite time singularity is from the incompressible Euler equations. But it is much harder to obtain a convincing Euler singularity due to the development of extremely sharp fronts in the early stage of the computation and the shearing instability in the tail region¹. The Navier–Stokes equations with degenerate diffusion coefficients capture the main effect of this potential Euler singularity and it is easier to resolve computationally due to the viscous regularization. As we will show in our scaling analysis, the degenerate diffusion coefficients also select a length scale for the smaller scale $Z(t)$, which plays an important role in generating a stable two-scale locally self-similar blowup. Without any viscous regularization, it is not clear what is the mechanism for selecting the length scale of $Z(t)$.

We need to choose the degenerate diffusion coefficients carefully to fulfill two purposes. On the one hand, the diffusion coefficients should be strong enough to control the shearing instability associated with the Euler equations so that the potential blowup can be stable and robust. On the other hand, the diffusion coefficients must not be too strong to suppress the intrinsic blowup mechanism of the Euler equations. The strength of the diffusion coefficients needs to maintain a delicate balance, especially in the crucial blowup region near the sharp front of the solution.

Out of such consideration, we propose to use the variable diffusion coefficients of the kind (2.8), which consists of a space-dependent part (SDP) and a time-dependent part (TDP). The SDP is globally small and degenerate at the origin with order $O(r^2) + O(z^2)$. Recall that the most important part of the blowup solution, i.e. the local profile near the sharp front, travels towards the origin $(r, z) = (0, 0)$. Correspondingly, the effective value of the SDP that affects the shrinking region of interest is decreasing to 0. Thus the blowup mechanism will not be hindered by this degenerate part of the viscosity. As we will see in Section 6.6, the order of degeneracy of the SDP is compatible with the smaller scale of the solution, so the SDP actually helps stabilize the two-scale blowup. In the meanwhile, the outer part of the solution (the far field) is under the influence of the non-degenerate part of the SDP, which suppresses some mild instability in the far field.

The TDP, which is equal to $0.025/\|\omega^\theta\|_{L^\infty}$, is relatively large in the early stage of the computation, so that it can help regularize the thin structure of the solution in the warm-up phase ($t \in [0, 1.6 \times 10^{-4}]$). However, as $\|\omega^\theta\|_{L^\infty}$ grows rapidly in time, the TDP will drop quickly and be dominated by the SDP in the critical blowup region near $(R(t), Z(t))$, and thus it will not harm the development of the focusing singularity in our blowup scenario. Figure 5.5 plots the SDPs of ν^r and ν^z evaluated at the point $(R(t), Z(t))$ and the TDP. We can see that the TDP drops below the SDP at an early time around $t = 1 \times 10^{-4}$ and is much smaller than the SDP in the stable phase ($t \in [1.6 \times 10^{-4}, 1.76 \times 10^{-4}]$). In fact, the TDP has no essential contribution to the development of the two-scale blowup. Removing the TDP in the late stage of the computation has almost no influence on the behavior of the solution.

Recall that the SDP parts of the diffusion coefficients consist of a r -dependent part and a z -dependent part. For ν^r , the r -dependent part of the diffusion coefficient dominates the z -dependent part. For ν^z , the z -dependent part dominates the r -dependent part in the warm-up phase and the r -dependent part dominates the z -dependent part in the stable phase. Moreover, the r -dependent part of ν^z is smaller than the r -dependent part of ν^r by a factor of 10^{-2} . This explains why the SDP of ν^z decays faster than that of ν^r in the late stage of the computation.

In summary, the effective values of the variable diffusion coefficients in the focusing blowup region near the sharp front are decreasing in time. As a result, the viscosity in this region of interest is

¹Numerical studies of potential singularity of the Euler equations in a similar scenario will be reported in a separate paper

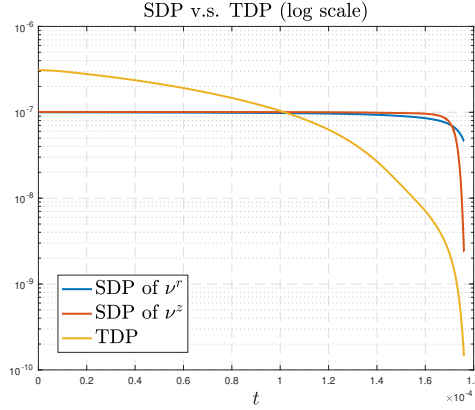


Figure 5.5: The SDP of ν^r and the SDP of ν^z evaluated at the point $(R(t), Z(t))$ versus the TDP.

not strong enough to prevent the blowup of the solution. In particular, this weak diffusion cannot prevent the occurrence and development of the two-scale feature in our scenario, which is crucial to the sustainability and stability of the blowup.

On the contrary, the diffusion with a constant coefficient will be too strong for a two-scale blowup to maintain in the late stage when the ratio between the large scale and the smaller scale becomes huge. If there were a two-scale structure, then the smaller scale would have generated a strong diffusion effect (with a constant diffusion coefficient) due to large second-order derivatives, which, paradoxically, would have smoothed out the smaller scale. This explains why we have observed that the two-scale feature is not sustainable in Case 2 computation and that the solution does not blowup in the end. In fact, the diffusion with a constant coefficient in the Navier–Stokes equations imposes a constraint on the spatial scaling of the blowup solution, if there is a stable blowup scaling. Such constraint denies the existence of a two-scale structure for the solution, which, however, appears to be crucial for the potential blowup in our computation in Case 1. We shall come back to this point in the next Section.

Remark 5.1. There were some unpublished computational results obtained by Dr. Guo Luo and the first author for 3D axisymmetric Euler and Navier–Stokes equations that showed some early sign of a tornado like singularity. However, the solution became unstable dynamically. In the case of the Euler equations, the shear layer in u_1 rolled up into several small vortices near the upper edge of the sharp front. The Navier–Stokes equations with a constant diffusion coefficient $\mu = 10^{-5}$ regularized these small vortices, but the solution developed into a “turbulent flow” in the late stage, which is very different from our computational results for the original Navier–Stokes equations with $\mu = 10^{-5}$. Unfortunately, these unpublished computational results are not reproducible due to the loss of Dr. Luo’s computer hard disk that contained all the computer codes and the initial data for these results.

6. POTENTIAL BLOWUP SCALING ANALYSIS

In this section, we will quantitatively examine the features of the potential blowup in our computation. We will first provide adequate numerical evidences that the growth and the spatial scaling of the solution obey some (inverse) power laws, which suggest that a finite-time singularity exists in a locally self-similar form. In particular, we employ a linear fitting procedure to estimate the blowup rates and scalings. Then we will perform an asymptotic analysis of the potential blowup based on a two-scale self-similar ansatz. We show that the results of the asymptotic analysis are highly consistent with our numerical results, supporting the existence of a locally self-similar blowup.

6.1. Linear fitting procedure. The most straightforward way to numerically identify a finite-time blowup is to study the growth rate of the solution. For a solution quantity $v(t)$ that is expected to blow up at some finite time T , a typical asymptotic model is the inverse power law:

$$v(t) \sim \alpha(T - t)^{-c_v} \quad \text{as } t \rightarrow T, \quad (6.1)$$

where $c_v > 0$ is the blowup rate and $\alpha > 0$ is some constant. To verify that $v(t)$ satisfies an inverse power law and to learn the power c_v , we follow the idea of Luo and Hou [LH14b] and study the time derivative of the logarithm:

$$\frac{d}{dt} \log v(t) = \frac{v'(t)}{v(t)} \sim \frac{c_v}{T - t}.$$

This naturally leads to the linear regression model

$$y(t; v) := \frac{v(t)}{v'(t)} \sim -\frac{1}{c_v}(t - T) =: \tilde{a}t + \tilde{b}, \quad (6.2)$$

with response variable y , explanatory variable t , and model parameters $\tilde{a} = -1/c_v$, $\tilde{b} = T/c_v$. Then the blowup rate c_v can be estimated via a standard least-squares procedure. The quality of the fitting using this model can be measured by the coefficient of determination (the R^2):

$$R^2 = 1 - \frac{SS_{\text{err}}}{SS_{\text{tot}}},$$

with a value close to 1 indicating a high quality fitting. Here $SS_{\text{tot}} = \sum_i (y_i - \bar{y})^2$ is the total sum of squares, $SS_{\text{err}} = \sum_i (y_i - \hat{y}_i)^2$ is the residual sum of squares, y_i, \hat{y}_i denote the observed and predicted values of the response variable y , respectively, and \bar{y} denotes the mean of the observed data y_i .

To have a convincing estimate of the blowup rate c_v , it is important that the fitting procedure is performed in a proper time interval $[t_1, t_2]$. First of all, this time interval must lie in the asymptotic regime of the inverse power law (6.1) if such scaling does exist. Secondly, the solution must be well resolved in this time interval $[t_1, t_2]$. As we have observed, the blowup settles down to a stable phase at around $t = 1.6 \times 10^{-4}$, after which the evolution of the solution begins to have a stable pattern. It is likely that the solution enters the asymptotic regime of the blowup after this time instant. In addition, we have learned in Section 4.2 that the numerical solution is well resolved before $t = 1.76 \times 10^{-4}$. Therefore, according to the two criteria, we should place the fitting interval $[t_1, t_2]$ within the time interval $[1.6 \times 10^{-4}, 1.76 \times 10^{-4}]$. Moreover, the interval should not be too short; otherwise, any curve may look like a straight line. In particular, we choose $[t_1, t_2] = [1.60 \times 10^{-4}, 1.75 \times 10^{-4}]$.

To perform the fitting procedure on the model (6.2), we need to compute the time derivative of $v(t)$ in the fitting interval $[t_1, t_2]$. Since the time derivative of some quantity of interest (e.g. $v(t) = \|\omega(t)\|_{L^\infty}$) may not be easy to compute from the equations (2.3), we will approximate $v'(t)$ using the observations of $v(t)$. We achieve this by first interpolating the observed values of $v(t)$ to a uniform discretization $t_1 = \tau_1 < \tau_2 < \dots < \tau_K = t_2$ of the interval $[t_1, t_2]$ using a 4th-order interpolation method, and then approximating these time derivatives on the grid points τ_i using a 2nd-order centered difference scheme. The linear fitting of the model (6.2) will then be performed over the interpolated values $v(\tau_i)$ and the approximated derivatives $v'(\tau_i)$. We will denote by $\tilde{c}_v = -1/\tilde{a}$, $\tilde{T}_v = -\tilde{b}/\tilde{a}$ the approximate blowup rate and blowup time obtained from this fitting procedure.

Remark 6.1. In the scenario of Luo and Hou [LH14b], the time derivative of $\|\omega(t)\|_{L^\infty}$ can be computed explicitly from the Euler equations with a simple expression since the maximum of $|\omega(t)|$ is always achieved at a fixed stagnation point on the boundary. In our scenario, however, the maximum location of $|\omega(t)|$ (and similarly, the maximum locations of other functions) is not fixed but traveling towards the origin $(r, z) = (0, 0)$. The mesh point (r_i, z_j) where $|\omega(r_i, z_j, t)|$ achieves the maximum over the discrete values may not be the exact maximum location of $|\omega(t)|$. That is, the spatial gradient of $|\omega(t)|$

may not be zero at (r_i, z_j) . It is then not correct to directly compute $d\|\omega(t)\|_{L^\infty}/dt$ using the equations (2.3) at (r_i, z_j) . Nevertheless, the relative error between $|\omega(r_i, z_j, t)|$ and $\|\omega(t)\|_{L^\infty}$ should be small. Therefore, we derive the time derivative directly from the observed values of $\|\omega(t)\|_{L^\infty}$.

Since the quantities for which we would like to obtain the potential blowup rates are mostly the L^∞ norms of some solution functions, their values are sensitive to the discretization methods, the choice of the adaptive mesh, and the interpolation operations, especially when the maximum locations are traveling as in our scenario. As a result, the observed values of the studied quantity $\nu(t)$ may not yield a very accurate approximation of its time derivative $\nu'(t)$; the interpolation of $\nu(t)$ onto a uniform mesh over $[t_1, t_2]$ would introduce additional errors. Therefore, the model (6.2) may not yield an ideal fitting even if the inverse power law (6.1) does exist, and the resulting \tilde{c}_ν may not reflect the true blowup rate c_ν , though it should still be a good approximation. To obtain a better approximation of c_ν , we will conduct a local search near the crude estimate \tilde{c}_ν and find a value \bar{c}_ν such that the model

$$\gamma(t; \nu) := \nu(t)^{-1/\bar{c}_\nu} \sim \alpha^{-1/\bar{c}_\nu} (T - t)^{c_\nu/\bar{c}_\nu} \sim \alpha^{-1/c_\nu} (T - t) =: \bar{a}t + \bar{b} \quad (6.3)$$

has the best linear regression fitness (the R^2) against a least-square test. More precisely, we put a uniform mesh (with 100 points) over the interval $[\bar{c}_\nu - 0.1, \bar{c}_\nu + 0.1]$, compute the R^2 value of the model (6.3) for each candidate blowup rate on the mesh, and find the blowup rate \bar{c}_ν such that the model (6.3) has the optimal fitness over all candidates. If \bar{c}_ν falls into one of the endpoints of the interval, i.e. $\bar{c}_\nu \pm 0.1$, we will conduct the local search again around \bar{c}_ν and update the value of \bar{c}_ν . After this procedure, the resulting \bar{c}_ν should be a better approximation of c_ν . Corresponding, $\bar{T} := -\bar{b}/\bar{a}$ is an approximation of the true blowup time T . Note that for the fitting of the model (6.3), we use the original recorded values of $\nu(t)$ rather than the time-interpolated values. We remark that the fitting of model (6.3) is more reliable than the fitting of model (6.2) in reflecting a potential inverse power law, as it is directly applied to the quantity of interest without taking the time derivative of the logarithm of this quantity. It is much harder for the logarithm of a blowup quantity to fall into the asymptotic regime in comparison with the blowup quantity itself. In other words, the fitting based on (6.3) is a refinement of the fitting based on (6.2).

6.2. Fitting of the growth rate. We are now ready to apply the above fitting procedures to the numerical solutions obtained in our computation. Figure(6.1) shows the fitting results for the quantity $\|u_1(t)\|_{L^\infty}$ (in Case 1) on the time interval $[t_1, t_2] = [1.6 \times 10^{-4}, 1.75 \times 10^{-4}]$. We can see that both models, $y(t; \|u_1\|_{L^\infty})$ and $\gamma(t; \|u_1\|_{L^\infty})$, have excellent linear fitness with R^2 values very close to 1 (the R^2 value for the model $\gamma(t; \|u_1\|_{L^\infty})$ is greater than $1 - 10^{-6}$). Note that the blowup rates (or the blowup times) learned from the two models are close to each other, cross-verifying the validity of both models. This strongly implies that $\|u_1\|_{L^\infty}$ has a finite-time singularity of an inverse power law with a blowup rate very close to 1, which is consistent with our observation and analysis in Section 3.5. Recall that we have observed a strong positive alignment between $\psi_{1,z}$ and u_1 around the maximum location $R(t), Z(t)$ of u_1 . In particular, $\psi_{1,z}(R(t), Z(t), t) \sim u_1(R(t), Z(t), t)$ in the stable phase $[1.6 \times 10^{-4}, 1.75 \times 10^{-4}]$. If we ignore the degenerate diffusion, then the equation of $\|u_1(t)\|_{L^\infty}$ can be approximated by

$$\frac{d}{dt} \|u_1(t)\|_{L^\infty} = 2\psi_{1,z}(R(t), Z(t), t) \cdot u_1(R(t), Z(t), t) \sim c_0 \|u_1(t)\|_{L^\infty}^2,$$

which then implies that $\|u_1(t)\|_{L^\infty} \sim (T - t)^{-1}$ for some finite time T . This asymptotic analysis is now supported by our linear fitting results.

Next, we study the growth of the maximum vorticity $\|\omega\|_{L^\infty}$, which is an important indicator of a finite-time singularity. However, the growth of $\|\omega\|_{L^\infty}$ may not reflect a clean inverse power law, since the maximum location of the vector magnitude $|\omega|$ and the maximum locations of the components $\omega^\theta, \omega^r, \omega^z$ are distinct in general. Therefore, we directly apply the fitting procedure to the maximums

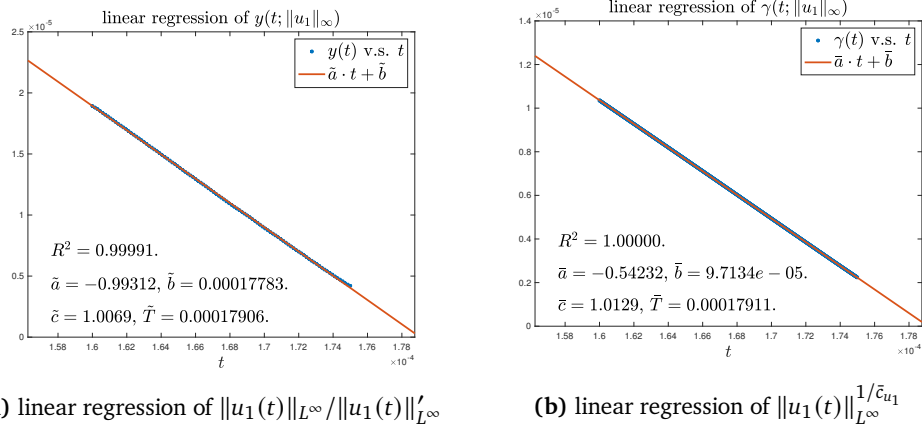


Figure 6.1: The linear regression of (a) $y(t; \|u_1\|_{L^\infty})$ and (b) $\gamma(t; \|u_1(t)\|_{L^\infty})$ on the time interval $[t_1, t_2] = [1.65 \times 10^{-4}, 1.75 \times 10^{-4}]$. The blue points are the data points obtained from our computation, and the red lines are the linear models. We plot the linear models on a larger interval.

of the vorticity components instead of to the maximum vorticity. As an illustration, we present the study of the inverse power law of the axial vorticity component ω^z . Figure 6.2 shows the linear fitting for the associated models of $\|\omega^z(t)\|_{L^\infty}$ (in Case 1) on the time interval $[t_1, t_2] = [1.6 \times 10^{-4}, 1.75 \times 10^{-4}]$. Again, we see that both models $y(t; \|\omega^z\|_{L^\infty})$ and $\gamma(t; \|\omega^z\|_{L^\infty})$ have good linear fitness, which provides evidences of the finite-time blow of $\|\omega^z(t)\|_{L^\infty}$ in the form of an inverse power law

$$\|\omega^z(t)\|_{L^\infty} \sim (T - t)^{-\tilde{c}_{\omega^z}}.$$

More importantly, the estimated blowup rate is approximately equal to 1.5, which implies that

$$\int_0^T \|\omega(t)\|_{L^\infty} \geq \int_0^T \|\omega^z(t)\|_{L^\infty} dt = +\infty.$$

According to our discussion in Section 3.3, this strongly supports the existence of a finite-time singularity of the solution to the initial-boundary value problem (2.3)–(2.6).

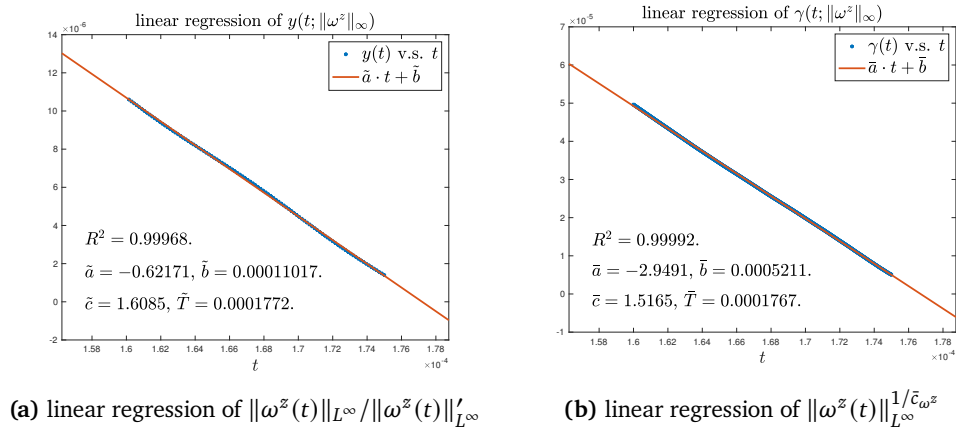


Figure 6.2: The linear regression of (a) $y(t; \|\omega^z\|_{L^\infty})$ and (b) $\gamma(t; \|\omega^z\|_{L^\infty})$ on the time interval $[t_1, t_2] = [1.65 \times 10^{-4}, 1.75 \times 10^{-4}]$. The blue points are the data points obtained from our computation, and the red lines are the linear models. We plot the linear models on a larger interval.

To further illustrate the existence of a potential finite-time blowup, we perform the linear fitting procedure on more blowup quantities computed with different mesh resolutions. We only present

the fitting results of model (6.3). Table 6.1 reports the linear fitting results of different solution quantities computed in Case 1 with different mesh sizes. Again, the fitting time interval is $[t_1, t_2] = [1.6 \times 10^{-4}, 1.75 \times 10^{-4}]$. We can see that all the quantities reported in the table have excellent fitting to some inverse power law, and the fitting results are consistent over different resolutions.

Mesh size	$\ u_1\ _{L^\infty}$			$\ \omega_1\ _{L^\infty}$			$\ \psi_{1,r}\ _{L^\infty}$		
	\bar{c}	$\bar{T}/10^{-4}$	R^2	\bar{c}	$\bar{T}/10^{-4}$	R^2	\bar{c}	$\bar{T}/10^{-4}$	R^2
1024×512	1.0129	1.7911	1.00000	1.9773	1.7908	1.00000	1.1154	1.7998	0.99999
1536×768	1.0126	1.7914	1.00000	2.0366	1.7966	1.00000	1.1151	1.7975	0.99999
1024×1024	1.0125	1.7916	1.00000	2.0217	1.7956	1.00000	1.1129	1.7966	1.00000
Mesh size	$\ \psi_{1,z}\ _{L^\infty}$			$\ u_{1,r}\ _{L^\infty}$			$\ u_{1,z}\ _{L^\infty}$		
	\bar{c}	$\bar{T}/10^{-4}$	R^2	\bar{c}	$\bar{T}/10^{-4}$	R^2	\bar{c}	$\bar{T}/10^{-4}$	R^2
1024×512	0.9744	1.7952	0.99990	2.0427	1.7712	0.99993	1.9752	1.7687	0.99998
1536×768	0.9730	1.7954	0.99990	2.0445	1.7718	0.99993	1.9690	1.7690	0.99998
1024×1024	0.9724	1.7954	0.99991	2.0438	1.7719	0.99993	1.9666	1.7692	0.99998
Mesh size	$\ \omega^\theta\ _{L^\infty}$			$\ \omega^r\ _{L^\infty}$			$\ \omega^z\ _{L^\infty}$		
	\bar{c}	$\bar{T}/10^{-4}$	R^2	\bar{c}	$\bar{T}/10^{-4}$	R^2	\bar{c}	$\bar{T}/10^{-4}$	R^2
1024×512	1.5045	1.7950	1.00000	1.4878	1.7652	0.99997	1.5165	1.7670	0.99992
1536×768	1.5407	1.7937	1.00000	1.4912	1.7658	0.99997	1.5108	1.7648	0.99992
1024×1024	1.5270	1.7911	1.00000	1.4924	1.7661	0.99997	1.5097	1.7623	0.99993

Table 6.1: Linear fitting results of model (6.3) on time interval $[t_1, t_2] = [1.6 \times 10^{-4}, 1.75 \times 10^{-4}]$ for different solution quantities computed with different mesh sizes.

However, the estimated blowup times obtained from the fitting of different blowup quantities agree only up to the third digit. This may be due to the fact that the estimated blowup time is an extrapolated information from the fitting model, which can be very sensitive to the recorded observations and the model parameters. In fact, if we force the blowup rate of $\|u_1\|_{L^\infty}$ to be $\bar{c} = 0.9$ (instead of $\bar{c} = 1.0129$) in model (6.3), then it still yields a fairly good linear regression with fitness $R^2 = 0.99945$, but the estimated blowup time drops to $\bar{T} = 1.7802$ (compared to 1.7911). Therefore, the estimated blowup time may not be a robust approximation of the true blowup time even if the finite-time singularity does exist. It is the estimated blowup rate that is more interesting in our analysis.

For the blowup rates reported in Table 6.1, we have the following observations and discussions. First, the fittings of $\|u_1\|_{L^\infty}$, $\|\psi_{1,z}\|_{L^\infty}$ again confirm the strong alignment between u_1 and $\psi_{1,z}$. As we can see, the blowup rates of $\psi_{1,z}$ and u_1 are both close to 1, which is consistent with our observation that $\psi_{1,z} \sim u_1$ in the critical region around $(R(t), Z(t))$. This result supports our discussions on the blowup mechanism in Section 3.5.

Moreover, there seems to be a pattern in the blowup rates of the quantities reported in Table 6.1. More precisely, we have the following approximation that agrees with the fitting results up to the first two digits:

$$\bar{c}_{u_1} \approx \bar{c}_{\psi_{1,r}} \approx \bar{c}_{\psi_{1,z}} \approx 1, \quad \bar{c}_{\omega^\theta} \approx \bar{c}_{\omega^r} \approx \bar{c}_{\omega^z} \approx 1.5, \quad \bar{c}_{\omega_1} \approx \bar{c}_{u_{1,r}} \approx \bar{c}_{u_{1,z}} \approx 2, \quad (6.4)$$

where we use \bar{c}_f to denote the estimated blowup rate of $\|f(t)\|_{L^\infty}$ for a function $f(r, z, t)$. In the next section, we will argue that this pattern implies the existence of power laws for the two spatial scales of the solution, which is consistent to the direct linear fitting of these scales. Furthermore, this pattern reflects the possibility that the solution blows up in a locally self-similar way.

6.3. Fitting of spatial scalings. Recall that we have observed a two-scale property of the solution in our scenario: the smaller scale (featured by $Z(t)$) measures the length scale of the local solution profile near the location $(R(t), Z(t))$ (or the sharp front), and the larger scale (featured by $R(t)$) measures the distance between the sharp front and the symmetry axis $r = 0$. Our numerical observations suggest that these two scales are separated and both converge to 0, which characterizes the focusing nature of the blowup. The next step is to quantitatively investigate how fast these two scales go down to 0. Just like how we characterize the growth of the solution, we assume that these two spatial scales of the solution also admit some power laws:

$$C_s(t) = (T - t)^{c_s}, \quad C_l(t) = (T - t)^{c_l}, \quad (6.5)$$

where C_s denotes the larger scale (with a smaller power $c_s > 0$) and C_l the smaller scale (with a larger power $c_l > 0$). We will use two methods to check the validity of the power laws (6.5) and to learn the powers c_s, c_l , and we will compare the results from both methods to see if they are consistent.

The first method to learn the scalings of C_s, C_l is to extract the spatial information of the solution from the growth of different quantities. In fact, if the blowup solution develops a local profile of a isotropic spatial scale $C_l(t)$, it should be reflected by the spatial derivatives. More precisely, for a blowup function $f(r, z, t)$ that is smooth with respect to the scale $C_l(t)$, we should have

$$C_l(t) \sim \frac{\|f(t)\|_{L^\infty}}{\|f_r(t)\|_{L^\infty}} \sim \frac{\|f(t)\|_{L^\infty}}{\|f_z(t)\|_{L^\infty}},$$

which is equivalent to the relation

$$c_l = c_{f_r} - c_f = c_{f_z} - c_f,$$

if $f(t)$ also admits an inverse power law (6.1). We have seen in Section 3.2 that the profile of u_1 is smooth when observed in a local neighborhood around $(R(t), Z(t))$, so we may use u_1 to extract the scaling of C_l . Our data in the previous subsection, particularly the pattern in (6.4), show that

$$\bar{c}_{u_{1,r}} - \bar{c}_{u_1} \approx \bar{c}_{u_{1,z}} - \bar{c}_{u_1} \approx 1,$$

which suggests that the solution has a local spatial scale

$$C_l(t) \sim Z(t) \sim T - t. \quad (6.6)$$

Similarly, we can learn the power of the larger scale C_s from our fitting of the growth of different blowup quantities. By the definition of u_1, ω_1 and ω , we have

$$\omega^\theta = r\omega_1, \quad \omega^r = -ru_{1,z}, \quad \omega^z = 2u_1 + ru_{1,r}.$$

We observe that the maximums of $\omega_1, u_{1,z}, u_{1,r}, \omega^\theta, \omega^r$ and ω^z are all achieved inside a local region around $(R(t), Z(t))$, whose length scale is featured by $Z(t) \ll R(t)$. Therefore, we should have

$$R(t) \sim \frac{\|\omega^\theta\|_{L^\infty}}{\|\omega_1\|_{L^\infty}} \sim \frac{\|\omega^r\|_{L^\infty}}{\|u_{1,z}\|_{L^\infty}} \sim \frac{\|\omega^z\|_{L^\infty}}{\|u_{1,r}\|_{L^\infty}},$$

which, ideally, is equivalent to the relations

$$c_s = c_{\omega^\theta} - c_{\omega_1} = c_{\omega^r} - c_{u_{1,z}} = c_{\omega^z} - c_{u_{1,r}}.$$

The data in Table 6.1 or the approximations in (6.4) yield that

$$\bar{c}_{\omega^\theta} - \bar{c}_{\omega_1} \approx \bar{c}_{\omega^r} - \bar{c}_{u_{1,z}} \approx \bar{c}_{\omega^z} - \bar{c}_{u_{1,r}} \approx 0.5,$$

which then suggests that

$$C_s(t) \sim R(t) \sim (T - t)^{0.5}. \quad (6.7)$$

The second method to verify the power laws (6.5) and to learn the powers c_s, c_l is by applying the fitting procedure in Section 6.1 directly to the blowup quantities $R(t)^{-1}, Z(t)^{-1}$. Figure 6.3 presents the linear regression of model (6.3) for $R(t)^{-1}, Z(t)^{-1}$. We can see in Figure 6.3(a) that $R(t)$ has an

excellent fitting to a power law with a rate $\bar{c}_s \approx 0.5$, which is very close to the conjectured power law (6.7) obtained from the first method.

Figure 6.3(b) shows that $Z(t)$ also approximately satisfies the power law with a rate $\bar{c}_l \approx 1$, though the fitness is not as good as that of $R(t)$. This lower fitness may be due to the issue that the numerical recording of $Z(t)$ is sensitive to the construction of the adaptive mesh and the interpolation operation between different meshes. Since $Z(t) \ll R(t)$, the relative error in $Z(t)$ due to discretization and interpolation is expected to be much larger than the relative error in $R(t)$. Nevertheless, the estimated power of $Z(t)$, which is close to 1, is consistent with the conjectured power law (6.6).

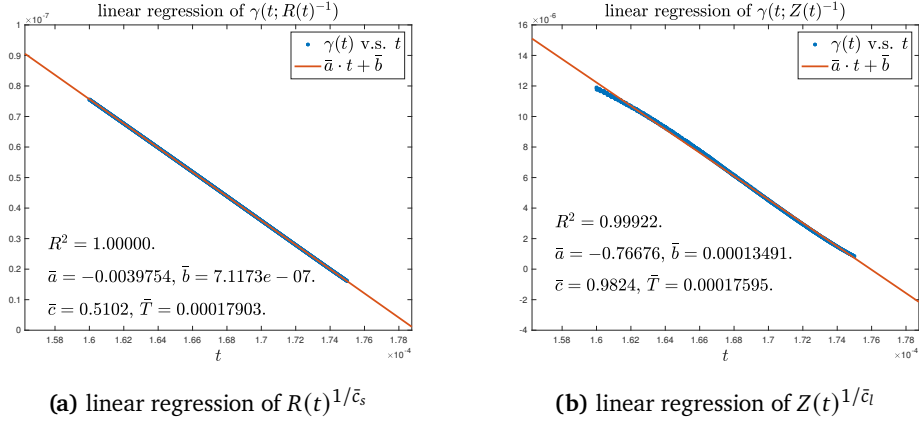


Figure 6.3: The linear regression of (a) $\gamma(t; R(t)^{-1})$ and (b) $\gamma(t; Z(t)^{-1})$ on the time interval $[t_1, t_2] = [1.65 \times 10^{-4}, 1.75 \times 10^{-4}]$. The blue points are the data points obtained from our computation, and the red lines are the linear models. We plot the linear models on a larger interval.

The consistency between the numerical fitting results in this subsection and in the last subsection further confirms the validity of the (inverse) power laws (6.1), (6.5) of the solution, which provides additional supporting evidence for the existence of a finite-time singularity.

6.4. Locally self-similar structure. It is well known that the 3D Euler equations have the scaling invariance property that, if $\mathbf{u}(x, t)$ is a solution to the equations, then

$$\mathbf{u}_{\lambda, \tau}(x, t) := \frac{\lambda}{\tau} \mathbf{u}\left(\frac{x}{\lambda}, \frac{t}{\tau}\right), \quad \forall \lambda, \tau \in \mathbb{R},$$

is still a solution. Similarly, the 3D Navier–Stokes equations satisfy a more restricted scaling invariance property that, if $\mathbf{u}(x, t)$ is a solution to the equations, then

$$\mathbf{u}_{\lambda}(x, t) := \frac{1}{\lambda} \mathbf{u}\left(\frac{x}{\lambda}, \frac{t}{\lambda^2}\right), \quad \forall \lambda \in \mathbb{R},$$

is still a solution. Regarding these scaling properties, a fundamental question is whether the Euler equations or the Navier–Stokes equations have self-similar solutions of the form

$$\mathbf{u}(x, t) = \frac{1}{(T-t)^{\gamma}} \mathbf{U}\left(\frac{x-x_0}{(T-t)^{\beta}}\right), \quad (6.8)$$

where \mathbf{U} is a self-similar vector profile and $\beta, \gamma > 0$ are scaling powers. If such a solution exists, it will imply that the Euler equations or the Navier–Stokes equations can develop a focusing self-similar singularity at the point x_0 at a finite time T .

The scaling properties of the Euler equations or the Navier–Stokes equations cannot hold in our scenario due to the existence of the cylinder boundary at $r = 1$ and the variable diffusion coefficients. Nevertheless, a focusing self-similar blowup can still exist asymptotically and locally near the symmetry

axis $r = 0$ for two reasons. First of all, since the potential singularity is a focusing one around the origin $(r, z) = 0$, the solid boundary at $r = 1$ has no essential contribution to the blowup and can be neglected as a far field. Secondly, the variable diffusion coefficients in our scenario are degenerate near the origin and have an asymptotic behavior in the critical region that may be compatible with a self-similar blowup. More importantly, as we have seen in the previous subsections, the (inverse) power law fitting for the growth and the spatial scales of the solution and the consistency among the fitting results strongly suggest that the solution develops a finite-time self-similar singularity of the form (6.8).

However, the conventional self-similar ansatz (6.8) with a single spatial scaling is not enough to fully characterize the potential blowup in our computation, since we have observed two separate spatial scales in the solution. To adjust the self-similar framework to our scenario, we propose the following self-similar ansatz with two spatial scalings in the axisymmetric setting:

$$u_1(r, z, t) \sim (T - t)^{-c_u} \bar{U} \left(\frac{r - R(t)}{(T - t)^{c_l}}, \frac{z}{(T - t)^{c_l}} \right), \quad (6.9a)$$

$$\omega_1(r, z, t) \sim (T - t)^{-c_\omega} \bar{\Omega} \left(\frac{r - R(t)}{(T - t)^{c_l}}, \frac{z}{(T - t)^{c_l}} \right), \quad (6.9b)$$

$$\psi_1(r, z, t) \sim (T - t)^{-c_\psi} \bar{\Psi} \left(\frac{r - R(t)}{(T - t)^{c_l}}, \frac{z}{(T - t)^{c_l}} \right), \quad (6.9c)$$

$$R(t) \sim (T - t)^{c_s} R_0. \quad (6.9d)$$

Here \bar{U} , $\bar{\Omega}$, $\bar{\Psi}$ denote the self-similar profiles of u_1 , ω_1 , ψ_1 respectively. For notational simplicity, we use c_u, c_ω, c_ψ for $c_{u_1}, c_{\omega_1}, c_{\psi_1}$. As in our previous setting, the reference point $R(t)$ is chosen to be r -coordinate of the maximum location of u_1 , and $R_0 > 0$ is some normalization constant. This ansatz depicts that, the solution develops an asymptotically self-similar blowup focusing at the point $(R(t), 0)$ with a local spatial scaling $(T - t)^{c_l}$, and in the mean time, the point $(R(t), 0)$ travels towards the origin with a different length scaling $(T - t)^{c_s}$.

In what follows, we will carry out a numerical study of the solution profile in a local region around the dynamic location $(R(t), Z(t))$ (the maximum location of u_1) to further demonstrate the existence of a locally self-similar blowup of the form (6.9). After that, we will analyze the existence conditions and the potential properties of the self-similar profiles U, Ω, Ψ using a dynamic rescaling formulation of the equations (2.3).

6.5. Numerical evidence of locally self-similar profiles. An straightforward but useful way to identify a self-similar solution is by comparing the properly normalized profiles of the solution at different time instants. As we have mentioned, the self-similar ansatz (6.9) is not supposed to hold globally in the entire computational domain \mathcal{D}_1 ; it should only characterize the asymptotic blowup behavior of the solution in a local critical region. Therefore, it is important that we focus our study on the solution profile in a small-scale neighborhood of a reference point. In particular, the reference point is chosen as usual to be $(R(t), Z(t))$, the maximum location of u_1 .

Figure 6.4 compares the level sets of u_1 at different time instants. The first row of Figure 6.4 plots the level sets of u_1 in a local domain $(r, z) \in [0.8 \times 10^{-4}, 2.5 \times 10^{-4}] \times [0, 8 \times 10^{-6}]$. We can see that in a short time interval, from $t = 1.72 \times 10^{-4}$ to $t = 1.75 \times 10^{-4}$, the profile of u_1 changes remarkably. The main part of the profile shrinks in space and travels towards $z = 0$ in the z direction and towards the symmetry axis $r = 0$ in the r direction. The sharp front also becomes thinner and thinner. However, if we plot the level sets of the spatially rescaled function

$$\tilde{u}_1(\xi, \zeta, t) = u_1(Z(t)\xi + R(t), Z(t)\zeta, t) \quad (6.10)$$

as in the second row of Figure 6.4, we can see that the landscape of \tilde{u}_1 (in the $\xi\zeta$ -plane) is almost static in the presented time interval. Here

$$\xi = \frac{r - R(t)}{Z(T)} \sim \frac{r - R(t)}{(T - t)^{c_l}}, \quad \zeta = \frac{z}{Z(T)} \sim \frac{z}{(T - t)^{c_l}}$$

are the shifted and rescaled coordinates motivated by the self-similar ansatz (6.9). This observation suggests that the asymptotic behavior (6.9a) of u_1 is valid and a self-similar profile $U(\xi, \zeta)$ exists.

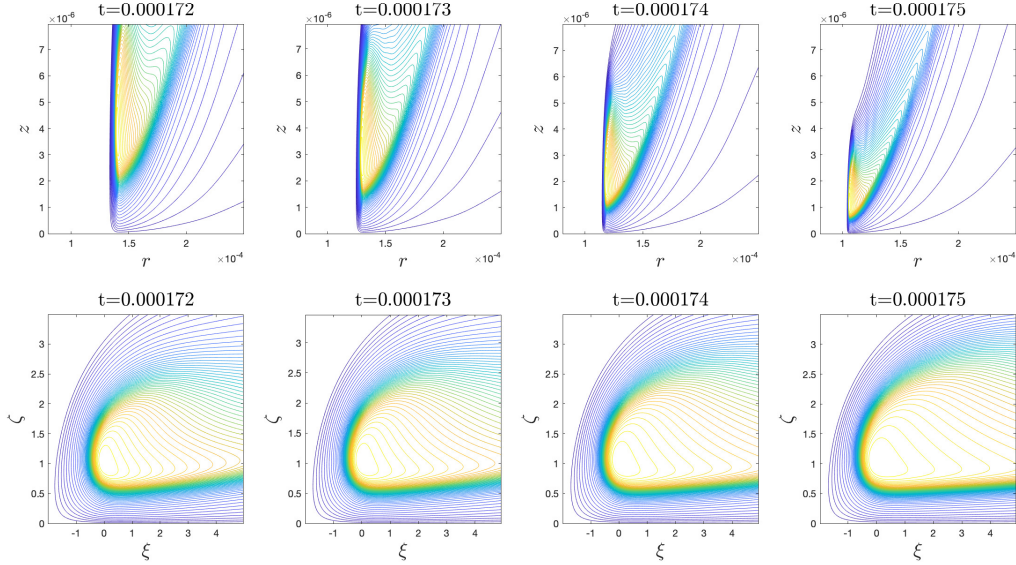


Figure 6.4: Comparison of the level sets of u_1 at different time instants. First row: original level sets of u_1 in the domain $(r, z) \in [0.8 \times 10^{-4}, 2.5 \times 10^{-4}] \times [0, 8 \times 10^{-6}]$. Second row: rescaled level sets of u_1 as a function of (ξ, ζ) in the domain $(\xi, \zeta) \in [-2, 5] \times [0, 3.5]$.

Figure 6.5 compares the level sets of ω_1 and the level sets of the spatially rescaled function

$$\tilde{\omega}_1(\xi, \zeta, t) = \omega_1(Z(t)\xi + R(t), Z(t)\zeta, t) \quad (6.11)$$

in a similar manner. Again, we can see that this profile of ω_1 changes a lot in the presented time interval $t \in [1.72 \times 10^{-4}, 1.75 \times 10^{-4}]$, while the landscape of $\tilde{\omega}_1$ seems to converge. This further suggests the validity of the self-similar conjecture (6.9) for the solution.

We can also compare the cross sections of the solution at different time instants to study the potential self-similar blowup. As an example, Figure 6.6(a) and (c) present the evolution of the cross sections of u_1 through the point $R(t), Z(t)$ in both directions. The length scale of the profile shrinks in both directions, and the sharp front travels towards $r = 0$. For comparison, Figure 6.6(b) and (d) plot the corresponding cross sections of the normalized function $u_1 / \|u_1\|_{L^\infty}$ in the rescaled coordinates $(r/R(t), z/Z(t))$, illustrating the potential convergence of the properly rescaled profile of u_1 . Note that the rescaled cross sections in the r direction seem to converge only in a small neighborhood of $R(t)$, i.e. within $|r - R(t)| = O(Z(t))$, implying that the asymptotic self-similar behavior (6.9a) is only valid locally. These results again support the existence of a locally self-similar profile of the solution near the reference location $(R(t), Z(t))$.

6.6. Asymptotic analysis of self-similar blowup. In this subsection, we carry out an asymptotic analysis based on the self-similar ansatz (6.9) to study how the self-similar profiles should behave and what the blowup rates should be.

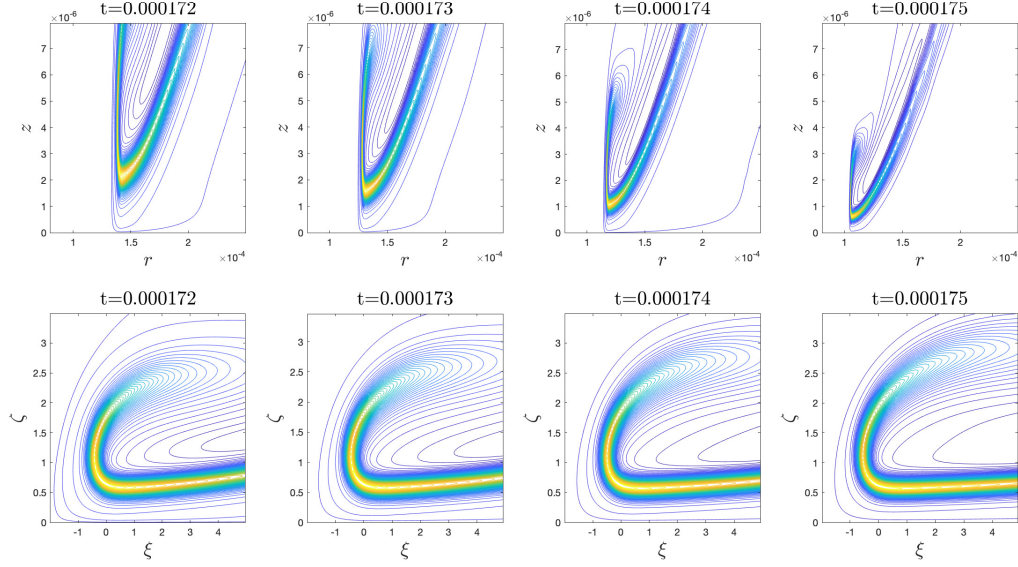


Figure 6.5: Comparison of the level sets of ω_1 at different time instants. First row: original level sets of u_1 in the domain $(r, z) \in [0.8 \times 10^{-4}, 2.5 \times 10^{-4}] \times [0, 8 \times 10^{-6}]$. Second row: rescaled level sets of ω_1 as a function of (ξ, ζ) in the domain $(\xi, \zeta) \in [-2, 5] \times [0, 3.5]$.

A standard method to study a self-similar blowup is by substituting the self-similar ansatz (6.9) into the physical equations (2.3) and deriving equations for the potential self-similar profiles $\bar{U}, \bar{\Omega}, \bar{\Psi}$, based on the fundamental assumption that these profiles exist and are smooth functions. More appropriately, we will introduce time-dependent profile solutions U, Ω, Ψ and treat the potential self-similar profiles $\bar{U}, \bar{\Omega}, \bar{\Psi}$ as the steady state of U, Ω, Ψ . Thus, we can relate (u_1, ω_1, ψ_1) to (U, Ω, Ψ) by a dynamic change of variables given below:

$$u_1(r, z, t) = (T - t)^{-c_u} U(\xi, \zeta, \tau(t)), \quad (6.12a)$$

$$\omega_1(r, z, t) = (T - t)^{-c_\omega} \Omega(\xi, \zeta, \tau(t)), \quad (6.12b)$$

$$\psi_1(r, z, t) = (T - t)^{-c_\psi} \Psi(\xi, \zeta, \tau(t)), \quad (6.12c)$$

where

$$\xi := \frac{r - R(t)}{C_l(t)}, \quad \zeta := \frac{z}{C_l(t)}, \quad (6.12d)$$

and $\tau(t)$ is a rescaled time satisfying

$$\tau'(t) = (T - t)^{-1}. \quad (6.12e)$$

Now the self-similar ansatz (6.9) asserts that the profile solutions $U(\xi, \zeta, \tau), \Omega(\xi, \zeta, \tau), \Psi(\xi, \zeta, \tau)$ in the $\xi\zeta$ -coordinates should converge to some time-independent profiles $\bar{U}(\xi, \zeta), \bar{\Omega}(\xi, \zeta), \bar{\Psi}(\xi, \zeta)$ as $\tau \rightarrow \infty$ (i.e. $t \rightarrow T$). In particular, $\bar{U}, \bar{\Omega}, \bar{\Psi}$ should be smooth functions of ξ, ζ .

Before we derive the equations for the profile solutions U, Ω, Ψ , we first make some preparations to simplify our argument, so that we can focusing on delivering the main idea. For simplicity, we only keep the diffusion terms (2.4) to their leading-order terms:

$$\begin{aligned} f_{u_1} &\approx \nu^r \left(u_{1,rr} + \frac{3}{r} u_{1,r} \right) + \nu^z u_{1,zz}, \\ f_{\omega_1} &\approx \nu^r \left(\omega_{1,rr} + \frac{3}{r} \omega_{1,r} \right) + \nu^z \omega_{1,zz}. \end{aligned}$$

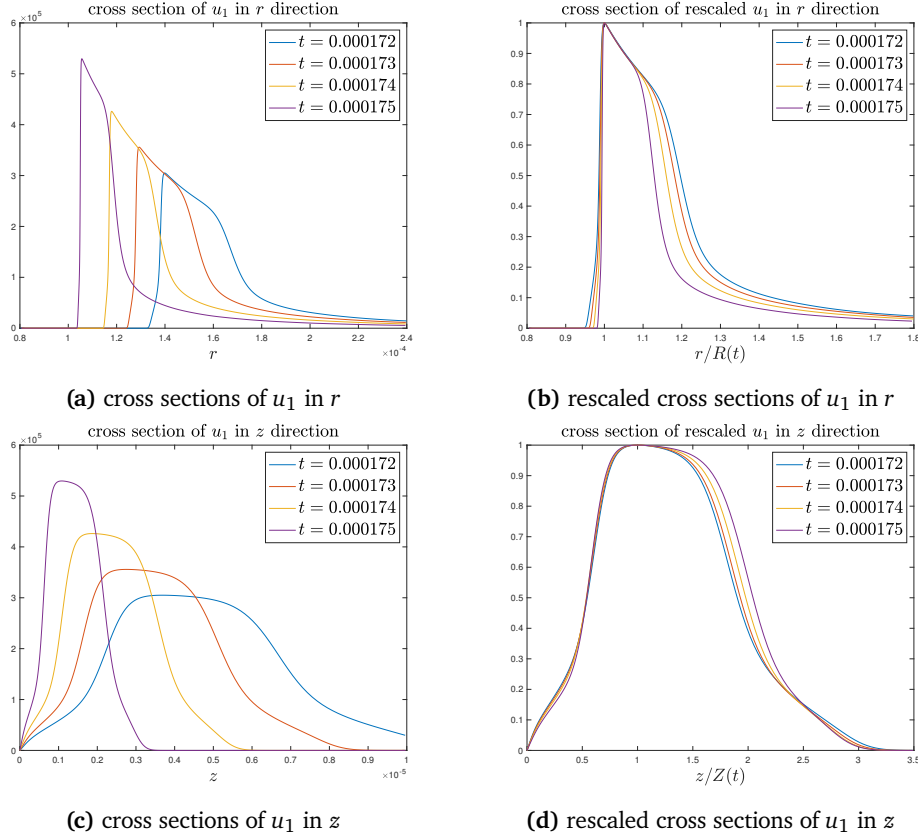


Figure 6.6: Cross sections and rescaled cross sections of u_1 through the point $R(t), Z(t)$ in both directions at different time instants. (a) Cross sections in the r direction. (b) Rescaled cross sections in the r directions. (c) Cross sections in the z direction. (d) Rescaled cross sections in the z directions.

We remark that this approximation will not change the resulting equations for the self-similar profiles in the asymptotic analysis, since the terms that we have dropped are asymptotically small under our ansatz. Moreover, we assume that the ansatz (6.9d) is actually an identity:

$$R(t) = (T - s)^{c_s} R_0.$$

Guided by our numerical observations, we make the two-scale assumption:

$$c_s < c_l, \quad \text{or equivalently, } R(t)/C_l(t) \rightarrow +\infty \quad \text{as } t \rightarrow T. \quad (6.13)$$

Recall that $C_l := (T - t)^{c_l}$ (see the definition (6.5)). We will also use the following notations

$$C_1(t) := (T - t)^{-1}, \quad C_u(t) := (T - t)^{-c_u}, \quad C_\omega(t) := (T - t)^{-c_\omega}, \quad C_\psi(t) := (T - t)^{-c_\psi}.$$

6.6.1. Substituting the self-similar ansatz. Now we substitute the change of variables (6.12) into the equations (2.3) (with the simplified diffusion terms). For clarity, we do this term by term. For the u_1 equation (2.3a), we have

$$\begin{aligned} u_{1,t} &= C_1 C_u U_\tau + c_u C_1 C_u U + c_l C_1 C_u (\xi U_\xi + \zeta U_\zeta) + c_s C_1 C_u C_l^{-1} R U_\xi, \\ u^r u_{1,r} + u^z u_{1,z} &= C_\psi C_u C_l^{-1} (-\xi \Psi_\zeta U_\xi + (2\Psi + \xi \Psi_\xi) U_\zeta) + C_\psi C_u C_l^{-2} R (-\Psi_\zeta U_\xi + \Psi_\xi U_\zeta), \\ 2\psi_{1,z} u_1 &= 2C_\psi C_u C_l^{-1} \Psi_\zeta U, \\ f_{u_1} &= C_u C_l^{-2} (\nu^r U_{\xi\xi} + 3\nu^r (\xi + R C_l^{-1})^{-1} U_\xi + \nu^z U_{\zeta\zeta}). \end{aligned} \quad (6.14a)$$

Note that we have used the expressions of u^r, u^z in (2.3d). We have also used the relation (6.12e): $\tau'(t) = (T - t)^{-1} = C_1$. Similarly, for the ω_1 equation (2.3b), we have

$$\begin{aligned} \omega_{1,t} &= C_1 C_\omega \Omega_\tau + c_\omega C_1 C_\omega \Omega + c_l C_1 C_\omega (\xi \Omega_\xi + \zeta \Omega_\zeta) + \underline{c_s C_1 C_\omega C_l^{-1} R \Omega_\xi}, \\ u^r \omega_{1,r} + u^z \omega_{1,z} &= C_\psi C_\omega C_l^{-1} (-\xi \Psi_\zeta \Omega_\xi + (2\Psi + \xi \Psi_\xi) \Omega_\zeta) + \underline{C_\psi C_\omega C_l^{-2} R (-\Psi_\zeta \Omega_\xi + \Psi_\xi \Omega_\zeta)}, \\ 2u_{1,z} u_1 &= 2C_u^2 C_l^{-1} U_\zeta U, \\ f_{\omega_1} &= C_\omega C_l^{-2} (\nu^r \Omega_{\xi\xi} + 3\nu^r (\xi + RC_l^{-1})^{-1} \Omega_\xi + \nu^z \Omega_\zeta \zeta). \end{aligned} \quad (6.14b)$$

Finally, for the Poisson equation (2.3c), we have

$$-\left(\partial_r^2 + \frac{3}{r} \partial_r + \partial_z^2\right) \psi_1 = \omega_1 \implies -C_\psi C_l^{-2} \left(\partial_\xi^2 + \frac{3}{\xi + RC_l^{-1}} \partial_\xi + \partial_\zeta^2\right) \Psi = C_\omega \Omega. \quad (6.14c)$$

6.6.2. Balancing the equations. The next step is to determine the relations between the quantities $C_u, C_\omega, C_\psi, C_l$ and R by balancing the terms in each equation of (6.14) in the asymptotic regime $t \rightarrow T$, based on the assumption that the limit profiles $\bar{U}, \bar{\Omega}, \bar{\Psi}$ are smooth regular functions of ξ, ζ and are independent of time t . We also assume that the diffusion term are of the same order as the vortex stretching term. This balance is crucial in determining the length scale for C_l or $Z(t)$.

We have underlined some terms in (6.14a) and (6.14b) for some reason to be clarified later. For those terms that are not underlined in (6.14a), the balance among various terms as $t \rightarrow T$ requires

$$C_1 C_u = C_\psi C_u C_l^{-1} \sim \nu C_u C_l^{-2}.$$

Similarly, for those terms that are not underlined in (6.14b), the balance among various terms as $t \rightarrow T$ enforces

$$C_1 C_\omega = C_\psi C_\omega C_l^{-1} = C_u^2 C_l^{-1} \sim \nu C_\omega C_l^{-2}.$$

Finally, for the Poisson equation (6.14c) to balance each other as $t \rightarrow T$, we must have

$$C_\psi C_l^{-2} = C_\omega.$$

Summarizing up these relations, we obtain

$$\begin{cases} C_u = C_1, \\ C_\omega = C_1 C_l^{-1}, \\ C_\psi = C_1 C_l, \end{cases} \iff \begin{cases} c_u = 1, \\ c_\omega = 1 + c_l, \\ c_\psi = 1 - c_l, \end{cases} \quad (6.15)$$

and

$$\nu^r \sim \nu^z \sim C_1 C_l^2 = (T - t)^{2c_l - 1}. \quad (6.16)$$

Note that the relations (6.15) also imply that the underlined terms can balance with each other in (6.14a) and in (6.14b).

So far, we have already obtained some meaningful information of the blowup rates. If the self-similar ansatz (6.9) is true, then no matter what the spatial scalings c_s, c_l are, the asymptotic blowup rates of $u_1, \psi_{1,r}, \psi_{1,z}$ are always 1:

$$\|u_1\|_{L^\infty} \sim C_u = C_1 = (T - t)^{-1}, \quad \|\psi_{1,r}\|_{L^\infty} \sim \psi_{1,z} \sim C_\psi C_l^{-1} = C_1 = (T - t)^{-1}.$$

This result of the asymptotic analysis is consistent with our observations and fitting results in Section 6.2, which confirms the validity of the inverse power law for u_1 . To obtain the blowup rate of ω_1 , we still need to determine the value of c_l .

6.6.3. Conservation of circulation. To determine the values of c_s, c_l , we need to make use of the conservation of the total circulation, an important physical property of the axisymmetric Euler or Navier–Stokes equations.

The total circulation is defined as

$$\Gamma(r, z, t) := ru^\theta(r, z, t) = r^2u_1(r, z, t).$$

It is easy to derive the equation of Γ from the u^θ equation (2.2a) of (or the u_1 equation (2.3a)):

$$\Gamma_t + u^r\Gamma_r + u^z\Gamma_z = rf_u. \quad (6.17)$$

Recall that f_u is the diffusion term in the u^θ equation (2.2a). In our scenario, Γ is a non-negative variable in the computational domain \mathcal{D}_1 , since $u_1 \geq 0$ in \mathcal{D}_1 . It is well known that the circulation function Γ satisfies a maximum principle for the Euler equations or the Navier–Stokes equations. In fact, it also satisfies a maximum principle for our equations (2.3). Let $(\tilde{R}(t), \tilde{Z}(t))$ be a local maximum location of Γ , then we have from (6.17) that

$$\frac{d}{dt}\Gamma(\tilde{R}, \tilde{Z}, t) = \nu^r\Gamma_{rr} + \nu^z\Gamma_{zz} - \frac{\nu_r^r}{\tilde{R}}\Gamma \leq 0,$$

where we have used that $\Gamma_{rr}, \Gamma_{zz} \leq 0$ at the local maximum location $(\tilde{R}(t), \tilde{Z}(t))$, and that $\nu_r^r \geq 0$ for the variable diffusion coefficient we use in our computation. This means that $\Gamma(\tilde{R}(t), \tilde{Z}(t), t)$ is always non-increasing in time.

In fact, we have observed that the maximum location $(R(t), Z(t))$ of u_1 is also a local maximum point of Γ . Therefore,

$$\frac{d}{dt}\Gamma(R(t), Z(t), t) = \nu^r\Gamma_{rr} + \nu^z\Gamma_{zz} - \frac{\nu_r^r}{R}\Gamma \leq 0.$$

The diffusion term $\nu^r\Gamma_{rr} + \nu^z\Gamma_{zz}$ cannot damp $\Gamma(R, Z, t)$ to 0 in a finite time as long as the diffusion coefficients are bounded, which is the case in our computation. From the expression (2.8a) of ν_r , we have $\nu_r^r = O(r)$ in the critical blowup region and thus $\nu_r^r(R, Z)/R = O(1)$. Therefore, the term $-\nu_r^r\Gamma/R$ is a linear damping term with an $O(1)$ coefficient, which, again, can only drive Γ to 0 as $t \rightarrow +\infty$. In summary, $\Gamma(R, Z, t)$ will not blowup or vanish to 0 in some finite time T . That is, $\Gamma(R, Z, t) = R^2u_1(R, Z, t) = O(1)$ as $t \rightarrow T$. This means that

$$R(t) \sim \|u_1\|_{L^\infty}^{-1/2} \sim (T-t)^{c_u/2} = (T-t)^{1/2},$$

which implies $c_s = 1/2$. We remark that this property only relies on the conservation of the maximum circulation and the fact that $c_u = 1$, which are intrinsic to the equations (2.3).

6.6.4. Determining the smaller scale. To determine c_l , we need to use again the asymptotic values of the variable diffusion coefficients,

$$\nu^r \sim \nu^z = O(r^2) + O(z^2) + 0.025 \|\omega^\theta\|_{L^\infty}^{-1},$$

for r, z close to 0, which follows from the expressions (2.8). In particular, in the critical region around the reference point $(R(t), Z(t))$ where the self-similar ansatz (6.9) is assumed to be valid, we have

$$\begin{aligned} \nu^r \sim \nu^z &= O(R^2) + O(Z^2) + O(R^{-1}\|\omega_1\|_{L^\infty}^{-1}) \\ &= O((T-t)^{2c_s}) + O((T-t)^{2c_l}) + O((T-t)^{1+c_l-c_s}) \sim (T-t)^1, \end{aligned}$$

where we have used $c_s = 1/2$ and the two-scale assumption (6.13) that $c_l > c_s$, so that $O((T-t)^{2c_l})$ and $O((T-t)^{1+c_l-c_s})$ are dominated by $O((T-t)^{2c_s})$. Comparing this with the relation (6.16), we conclude that $2c_l - 1 = 1$, that is, $c_l = 1$.

We have now obtained all the blowup rates and the spatial scalings in the self-similar ansatz (6.9):

$$c_s = 1/2, \quad c_l = 1, \quad c_u = 1, \quad c_\omega = 1 + c_l = 2, \quad c_\psi = 1 - c_l = 0. \quad (6.18a)$$

Moreover, the derivative relations and product relations yield that

$$\begin{aligned} c_{\psi_{1,r}} &= c_{\psi_{1,z}} = c_\psi + c_l = 1, \quad c_{u_{1,r}} = c_{u_{1,z}} = c_u + c_l = 2, \\ c_{\omega^\theta} &= c_\omega - c_s = 1.5, \quad c_{\omega^r} = c_{u_{1,z}} - c_s = 1.5, \quad c_{\omega^z} = c_{u_{1,r}} - c_s = 1.5. \end{aligned} \quad (6.18b)$$

These results are surprisingly consistent with the fitting data in Sections 6.2 and 6.3, especially the numerically observed pattern (6.4). The consistency between the blowup rates obtained by our numerical fitting procedures and the those obtained by the asymptotic scaling analysis provides further support for the existence of a finite time locally self-similar blowup of the form (6.9).

We remark that if we use a constant diffusion coefficient $\nu^r = \nu^z = \mu$, then through a similar balancing procedure we will obtain a different scaling result with $c_l = 1/2$. This implies that there is no two-scale feature in the potential blowup solution, which is consistent with our numerical observations. This also explains why the two-scale blowup cannot survive the diffusion with a constant coefficient in Case 2 computation, as we have seen in Section 5.

6.6.5. Equations for the self-similar profiles. Our previous analysis on the blowup rates is based on the fundamental assumption that the asymptotic self-similar profiles $\bar{U}, \bar{\Omega}, \bar{\Psi}$ exist, for which we present strong numerical evidences in the previous sections. To gain more insights into the locally self-similar blowup, we will derive some potential time-independent equations for the self-similar profiles, which may help us understand the properties and the existence conditions of these profiles.

Collecting the terms in (6.14a), (6.14b) and (6.14c) and using the relations in (6.15) and (6.16), we first obtain the following time-dependent equations for the dynamic profiles:

$$\begin{aligned} U_\tau + (c_l \xi - \xi \Psi_\zeta) U_\xi + (c_l \zeta + 2\Psi + \xi \Psi_\xi) U_\zeta + \underbrace{RC_l^{-1}((c_s - \Psi_\zeta) U_\xi + \Psi_\xi U_\zeta)}_{= 2\Psi_\zeta U - c_u U + \tilde{\nu}^r (U_{\xi\xi} + 3(\xi + RC_l^{-1}) U_\xi) + \tilde{\nu}^z U_{\zeta\zeta}}, \\ \Omega_\tau + (c_l \xi - \xi \Psi_\zeta) \Omega_\xi + (c_l \zeta + 2\Psi + \xi \Psi_\xi) \Omega_\zeta + \underbrace{RC_l^{-1}((c_s - \Psi_\zeta) \Omega_\xi + \Psi_\xi \Omega_\zeta)}_{= 2U_\zeta U - c_\omega \Omega + \tilde{\nu}^r (\Omega_{\xi\xi} + 3(\xi + RC_l^{-1}) \Omega_\xi) + \tilde{\nu}^z \Omega_{\zeta\zeta}}, \end{aligned} \quad (6.19a)$$

$$\begin{aligned} -(\partial_{\xi\xi} + 3(\xi + RC_l^{-1})^{-1} \partial_\xi + \partial_{\zeta\zeta}) \Psi = \Omega, \end{aligned} \quad (6.19b)$$

$$- (\partial_{\xi\xi} + 3(\xi + RC_l^{-1})^{-1} \partial_\xi + \partial_{\zeta\zeta}) \Psi = \Omega, \quad (6.19c)$$

where

$$\tilde{\nu}^r(\xi, \zeta) := (T - t)^{-1} \nu^r(C_l \xi + R(t), C_l \zeta), \quad \tilde{\nu}^z(\xi, \zeta) := (T - t)^{-1} \nu^z(C_l \xi + R(t), C_l \zeta).$$

For the self-similar profiles to exist, it requires that the solution to the equations (6.19) converge to some non-trivial steady state $\bar{U}, \bar{\Omega}, \bar{\Psi}$ as $\tau \rightarrow \infty$. We thus expect that each equation of (6.19) is balanced in the limit $\tau \rightarrow \infty$. Note that from the relation (6.12e) we have $\tau = -\log(T - t) + c$ for some constant c , so $\tau \rightarrow \infty$ means $t \rightarrow T$. Since we have argued that $R(t)/C_l(t) \sim (T - t)^{-1/2} \rightarrow \infty$ as $t \rightarrow T$, the underlined terms in equations (6.19a) and (6.19b) need to satisfy some extra conditions so that they can balance with the other terms. In particular, we should have

$$RC_l^{-1}((c_s - \Psi_\zeta) U_\xi + \Psi_\xi U_\zeta) \rightarrow G_u(\xi, \zeta), \quad RC_l^{-1}((c_s - \Psi_\zeta) \Omega_\xi + \Psi_\xi \Omega_\zeta) \rightarrow G_\omega(\xi, \zeta)$$

for some smooth functions G_u, G_ω as $t \rightarrow T$. This further implies that

$$(c_s - \Psi_\zeta) U_\xi + \Psi_\xi U_\zeta \rightarrow 0 \quad \text{and} \quad (c_s - \Psi_\zeta) \Omega_\xi + \Psi_\xi \Omega_\zeta \rightarrow 0 \quad \text{as } t \rightarrow T.$$

Moreover, since $R(t)/C_l(t) \rightarrow \infty$ as $t \rightarrow T$, the lower order diffusion term $3(\xi + RC_l^{-1})^{-1} \partial_\xi$ in equations (6.19a), (6.19b) and in the Poisson equation (6.19c) should vanish as $t \rightarrow T$.

Based on the preceding discussions, we thus propose the following time-independent equations for the self-similar profiles $\bar{U}, \bar{\Omega}, \bar{\Psi}$:

$$(c_l \xi - \xi \bar{\Psi}_\zeta) \bar{U}_\xi + (c_l \zeta + 2\bar{\Psi} + \xi \bar{\Psi}_\xi) \bar{U}_\zeta + G_u = 2\bar{\Psi}_\zeta \bar{U} - c_u \bar{U} + \tilde{\nu}^r \bar{U}_{\xi\xi} + \tilde{\nu}^z \bar{U}_{\zeta\zeta}, \quad (6.20a)$$

$$(c_l \xi - \xi \bar{\Psi}_\zeta) \bar{\Omega}_\xi + (c_l \zeta + 2\bar{\Psi} + \xi \bar{\Psi}_\xi) \bar{\Omega}_\zeta + G_\omega = 2\bar{U}_\zeta \bar{\Omega} - c_\omega \bar{\Omega} + \tilde{\nu}^r \bar{\Omega}_{\xi\xi} + \tilde{\nu}^z \bar{\Omega}_{\zeta\zeta}, \quad (6.20b)$$

$$-(\partial_{\xi\xi} + \partial_{\zeta\zeta}) \bar{\Psi} = \bar{\Omega}, \quad (6.20c)$$

$$(c_s - \bar{\Psi}_\zeta) \bar{U}_\xi + \bar{\Psi}_\xi \bar{U}_\zeta = 0, \quad (6.20d)$$

$$(c_s - \bar{\Psi}_\zeta) \bar{\Omega}_\xi + \bar{\Psi}_\xi \bar{\Omega}_\zeta = 0, \quad (6.20e)$$

where

$$\bar{\nu}^r(\xi, \zeta) := \lim_{t \rightarrow T} (T - t)^{-1} \nu^r(R(t), 0), \quad \bar{\nu}^z(\xi, \zeta) := \lim_{t \rightarrow T} (T - t)^{-1} \nu^z(R(t), 0).$$

The existence of the self-similar profiles of the above equations is beyond the scope of this paper. One should note that our preceding asymptotic scaling analysis is only valid when we rescale the solution and zoom into a shrinking neighborhood of $(R(t), Z(t))$ of the smaller scale. Correspondingly, the equations (6.20) only characterize the behavior of the asymptotic self-similar profiles $\bar{U}, \bar{\Omega}, \bar{\Psi}$ on the scale of C_l (the smaller scale $Z(t)$) in the limit $t \rightarrow T$. If we zoom out to the scale of $R(t)$, or even back to the macroscopic scale, we will not be able to see the effect of these equations in a domain of constant size. Therefore, the potential two-scale blowup in our scenario is only locally self-similar.

6.6.6. A level set condition. Though we cannot use the equations (6.20) to determine the self-similar profiles $\bar{U}, \bar{\Omega}, \bar{\Psi}$, we can still learn some properties of the profiles from them. Note that the equations (6.20d) and (6.20e) are independent of the unknown functions G_u, G_ω , it thus makes sense to study their implications. One can see these two equations as the necessary conditions for the self-similar profiles to exist. The physical solution u_1, ω_1, ψ_1 can only develop the two-scale self-similar blowup when their profiles satisfy these two conditions locally (or after rescaling). If these two conditions are not satisfied locally, the underlined terms in equations (6.19) will not be compatible with our preceding scaling analysis based on the balance of scales among various terms.

Let $\Phi(\xi, \zeta) = \Psi(\xi, \zeta) - c_s \zeta$. Then the equations (6.20d) and (6.20e) can be written as

$$\Phi_\xi U_\zeta - \Phi_\zeta U_\xi = 0, \quad \Phi_\xi \Omega_\zeta - \Phi_\zeta \Omega_\xi = 0, \quad (6.21)$$

which implies that the gradient of U, Ω, Φ are parallel to each other:

$$(U_\xi, U_\zeta) \parallel (\Omega_\xi, \Omega_\zeta) \parallel (\Phi_\xi, \Phi_\zeta),$$

or that the level sets of U, Ω, Φ have the same geometric contours. In other words, the profiles U, Ω, Φ can be viewed as functions of each other:

$$U = U(\Phi), \quad \Omega = \Omega(\Phi).$$

The above relationship also implies that the velocity field induced by the modified stream function Φ is parallel to the level set of U and Ω . In other words, the large underlined advection terms in (6.19a) and (6.19b) enforce an interfacial condition that the local velocity field near the “free interface” (the sharp front) should be tangent to the “free interface”. This also provides us a way to numerically verify the condition (6.21). Note that under the asymptotic ansatz (6.9), we have

$$(u_{1,r}, u_{1,z}) \parallel (U_\xi, U_\zeta) \quad \text{and} \quad (\omega_{1,r}, \omega_{1,z}) \parallel (\Omega_\xi, \Omega_\zeta),$$

which means that, if U is a function of Ω , then u_1 is also a function of ω_1 :

$$(u_{1,r}, u_{1,z}) \parallel (\omega_{1,r}, \omega_{1,z}). \quad (6.22)$$

We can thus examine the validity of the condition (6.21) by comparing the level sets of u_1 and ω_1 .

Figure 6.7 compares the level sets of the rescaled functions $\tilde{u}_1, \tilde{\omega}_1$ (see the definitions (6.10), (6.11)) at $t = 1.76 \times 10^{-4}$ in the $\xi\zeta$ -plane. As we can see, though the contours of these two functions are not exactly the same in the local neighborhood (of length scale $Z(t)$) of the point $(R(t), Z(t))$, they have surprising geometric similarities. In particular, the level sets of \tilde{u}_1 and $\tilde{\omega}_1$ are almost parallel to each other along curved band where lies the thin structure of $\tilde{\omega}_1$. This numerical observation provides a strong evidence of the validity of the condition (6.21) in the critical blowup region and partial justification of our asymptotic analysis of the potential locally self-similar blowup. As mentioned above, we can also understand this interesting phenomenon from a different angle: it is because the level set condition (6.22) is well satisfied in a local region around $(R(t), Z(t))$ that the solution can possibly develop a locally self-similar blowup in the form of (6.9).

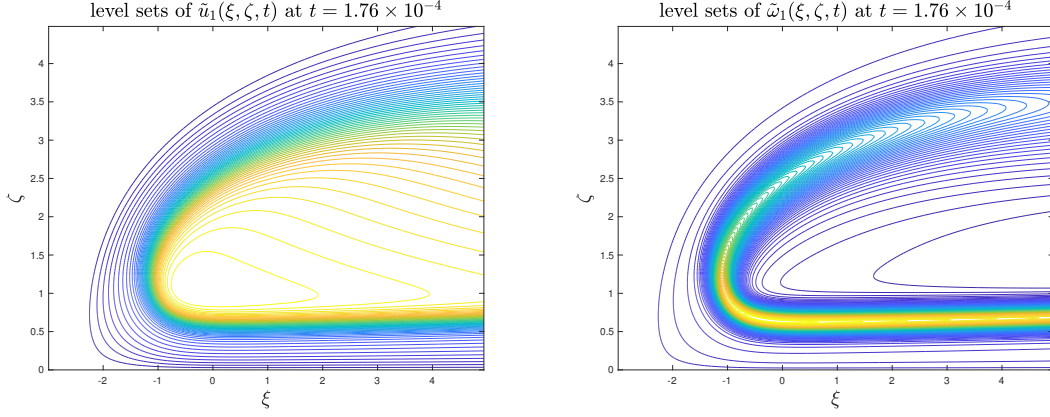


Figure 6.7: Level sets of the stretched functions \tilde{u}_1 (left) and $\tilde{\omega}_1$ (right) at $t = 1.76 \times 10^{-4}$.

6.6.7. Local compression along the radial direction. The underlined terms in (6.19) can also explain the sharp fronts in the profiles of u_1, ω_1 in the r direction (see Figure 3.5). At any time t before the blowup time T , namely when τ is finite, the conditions (6.20a) and (6.20b) are not expected to be satisfied exactly. Therefore, the underlined terms in equations (6.19a) and (6.19b) are active convection terms that serve to shape the profiles of U, Ω . The corresponding velocity field is given by

$$U^\xi := RC_l^{-1}(c_s - \Psi_\zeta), \quad U^\zeta = RC_l^{-1}\Psi_\xi,$$

which is formally much stronger than the velocity field corresponding to the non-underlined advection terms. This strong advection effect will transport and redistribute the profiles of U, Ω so that the conditions (6.20a) and (6.20b) are satisfied locally.

Let us now focus on the velocity U^ξ in the ξ direction (i.e. the r direction). In particular, we study how the sign of U^ξ changes. Suppose that the profile solution U is already very close to the steady state, so that the time derivative of the maximum of U is negligible. By evaluating the U -equation at the maximum location of U , namely at the point $(\xi_0, \zeta_0) = (0, Z(t)/C_l(t))$, we have

$$(2\Psi_\zeta - c_u)U \approx -\tilde{\nu}^r U_{\xi\xi} - \tilde{\nu}^z U_{\zeta\zeta} > 0.$$

Since $U(\xi_0, \zeta_0) > 0$, we obtain

$$\Psi_\zeta(\xi_0, \zeta_0) \geq c_u/2 = \frac{1}{2}.$$

As a result, the velocity U^ξ is negative (traveling from right to left) around the point (ξ_0, ζ_0) since

$$U^\xi(\xi_0, \zeta_0) = RC_l^{-1}(c_s - \Psi_\zeta(\xi_0, \zeta_0)) = RC_l^{-1}\left(\frac{1}{2} - \Psi_\zeta(\xi_0, \zeta_0)\right) < 0.$$

Also, we have learned from our numerical observations that the maximum location of the cross-section $\psi_{1,z}(r, Z(t))$ (as a function of r) aligns with the maximum location of u_1 . The value of $\psi_{1,z}(r, Z(t))$ decreases as r goes away from $R(t)$ (see Figure 3.12(a)); correspondingly, the value of Ψ_ζ (the rescaled version of $\psi_{1,z}$) will drop below $1/2$ as $|\xi|$ becomes large. As a result, the velocity U^ξ is positive when $|\xi|$ is away from 0 by a small distance.

To see this more clearly, we plot the ξ cross sections of U, Ψ_ζ through the point (ξ_0, ζ_0) at physical time $t = 1.7 \times 10^{-4}$ in Figure 6.8(a) and the corresponding ξ cross section of $c_s - \Psi_\zeta$ in Figure 6.8(b). The rescaled profiles U and Ψ_ζ are obtained from the numerical solution u_1 and $\psi_{1,z}$ via the formulas (6.12) with the blowup rates given by (6.18) and the blowup time estimated by the linear fitting of u_1 in Section 6.2 (i.e. $T = 1.791 \times 10^{-4}$). We can see that, as we have argued, U^ξ is negative near the maximum location $(0, \zeta_0)$ of U and is positive for ξ away from 0. Consequently, there are two

hyperbolic points in the rescaled radial velocity U^ξ : the left one is a compression point, while the right one is a rarefaction point. The local compressive nature of the flow along the radial direction explains why u_1 (or U) develops a sharp front to the left of its maximum location in the r direction; the rarefaction wave to the right of its maximum location explains why the local profile of u_1 is relatively flat on the right side of its maximum location (see Figure 3.5(a)). We remark that we can observe a similar flow structure in other ξ cross sections of U^ξ that correspond to different values of ζ .

In summary, the flow structure of the rescaled radial velocity U^ξ forces the profile of U to develop a two-phase structure via the underlined advection term in the equation (6.19a). This advection effect continues to shape the profile of U until the level set condition (6.20d) is well satisfied locally. Conversely, the fact that the numerical solution u_1 develops a sharp front to the left of its maximum location (in the r direction) and a smooth tail on the right strongly supports the validity of our preceding analysis for the self-similar blowup in a local region around $(R(t), Z(t))$.

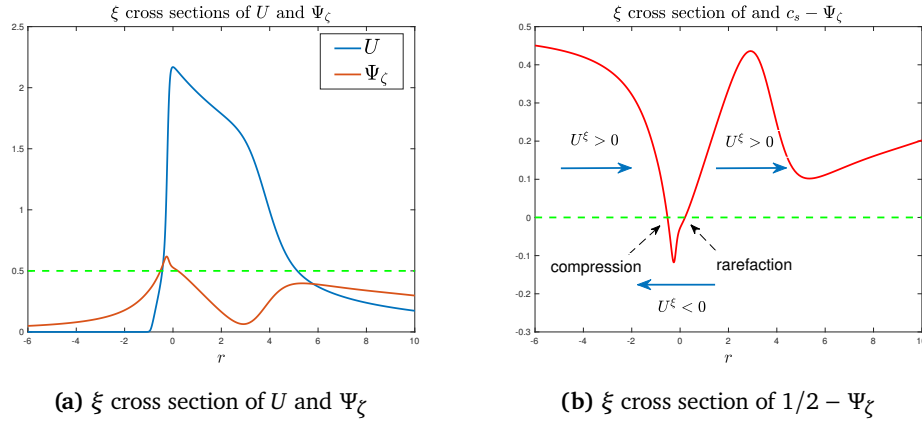


Figure 6.8: (a) The ξ cross sections of U and Ψ_ζ ; the green dashed line makes the level of $1/2$. (b) The ξ cross section of $1/2 - \Psi_\zeta$; the green dashed line makes the level of 0 and the blue arrows indicate the direction of the flow.

6.7. On the choice of diffusion coefficients. As we have demonstrated in the previous subsection, the fact that $c_u = 1$ and $c_s = 1/2$, i.e.

$$\|u_1(t)\|_{L^\infty} \sim (T-t)^{-1}, \quad R(t) \sim (T-t)^{1/2},$$

is an intrinsic property of the equations (2.3), which does not depend on the choice of the diffusion coefficients (though we have used that $\nu_r^r \geq 0$, but it is not essential). However, the result that $c_l = 1$ and its consequences (such as $c_\omega = 2$) rely on the particular asymptotic behavior of the degenerate diffusion coefficients:

$$\nu^r \sim \nu^z \sim R(t)^2 \sim (T-t)^1,$$

which does not seem to be essential to the potential blowup.

We have also solved the initial-boundary value problem (2.3)–(2.6) with stronger or weaker diffusion but failed to observe convincing evidences of a sustainable (self-similar) blowup. Since the smooth diffusion coefficients are even functions of r and z (see Section 2.2), we can only choose ν^r, ν^z to have the asymptotic behavior

$$\nu^r, \nu^z = O(r^{2p}) + O(z^{2q})$$

for some integers p, q , where we have ignored the time-dependent part of ν^r, ν^z . If the diffusion is too strong ($p, q = 0$), the two-scale feature cannot survive and there is no blowup observed, as we have reported in Section 5. If the diffusion is too weak or if there is no diffusion, the solution quickly becomes very unstable in the early stage of the computation before a stable self-similar blowup can be

observed. Even in the case of $p = q = 1$, the constants in front of r^2 and z^2 need to be chosen carefully so that the diffusion is strong enough to control the mild oscillations in the tail region.

It would be interesting to investigate whether the scale $c_l = 1$ is intrinsic to the two-scale singularity or it is determined by the order of degeneracy $O(r^2) + O(z^2)$ in our variable diffusion coefficients. We plan to investigate this question by applying degenerate diffusion coefficients with different orders of degeneracy at the origin. As in the case of $p = q = 1$, the constants in front of r^{2p} and z^{2q} need to be chosen carefully so that the diffusion is strong enough to control the mild oscillations in the tail region. We shall leave this question to our future work.

7. SHEARING INDUCED OSCILLATIONS AND NUMERICAL REGULARIZATION

In this section, we investigate the mild oscillations that occur at the tail part of the solution in the very late stage of our computation, which seem to be generated by the vortex shedding from the strong shearing flow in the near field. Such oscillations do not cause or contribute to the potential singularity of interest; instead, they may obstruct the blowup process by compromising the nice coupling phenomena of the solution that we discussed in Section 3.5. In order to comprehend the true nature of the potential blowup, we choose to use numerical regularization, the re-meshed low-pass filtering, to control the mild oscillations in the tail region. We will study the effect of the numerical regularization by comparing our results in Case 1 and Case 3.

7.1. Oscillations induced by velocity shearing. We mentioned earlier that we could not extend the computation all the way to the potential singularity time in Case 1. One of the reasons is that our mesh strategy with an affordable mesh size will lose effectiveness when the contrast between the two separate scales becomes extremely huge. Another reason is that the solution triggers some mild oscillations in the late stage of our computation, particularly when $t \geq 1.76 \times 10^{-4}$. According to our observations, the oscillations mainly occur along the long tail part of the solution where a strong velocity shear appears.

The first row of Figure 7.1 shows the level sets of u_1 , ω_1 (computed on mesh of size 1024×512 in Case 1) at $t = 1.76 \times 10^{-4}$ in a local region where the oscillations begin to appear. We can see that the tails of u_1 and ω_1 have already had mild oscillations that propagate to the far field. The second row of Figure 7.1 shows that the oscillations become stronger at $t = 1.764 \times 10^{-4}$. We remark that these oscillations we observe are not the same as the grid-scale high frequency instability that we typically observe for the Kelvin–Helmholtz instability since the degenerate diffusion has regularized the high frequency components of the solution. In fact, the wavelengths of these oscillations remain the same as we increase the mesh size from $(n, m) = (1024, 512)$ to $(n, m) = (2048, 1024)$.

To understand the cause of these oscillations, we look at the velocity field near the tail part of the solution that is shown in Figure 7.2 (in the rescaled coordinates). The arrows represent the direction of the velocity vector field, and the background color represents the profile (magnitude) of ω_1 . One can see that the flows on the two sides of the tail have opposite directions, meaning that there is strong a velocity shearing along the tail. This shearing can trigger unstable modes and roll into oscillations under slight perturbations. In fact, this long thin tail structure of ω_1 mimics the behavior of a regularized vortex sheet. This explains the occurrence of the mild instability in the late stage of our computation when the structure of ω_1 becomes very thin.

In general, viscosity shall prevent the occurrence of shearing-type instability in fluids. However, the variable diffusion coefficients (2.8) in our equations (2.3) are degenerate in both space and time. The space-dependent part of the diffusion coefficients is degenerate at $r = 0$ and $z = 0$, and the time-dependent part decreases rapidly in time since $\max \omega^\theta$ grows rapidly. Therefore, as the main profiles of the solution grow and travel towards the origin $(r, z) = (0, 0)$, the effective diffusion

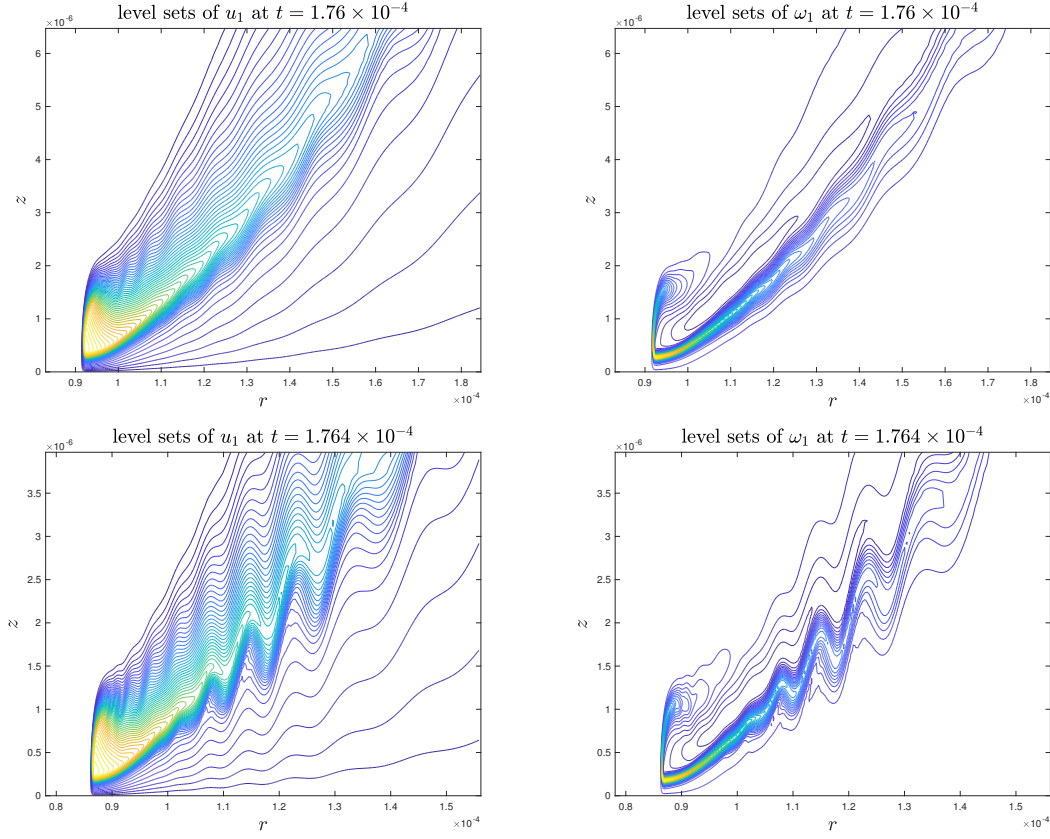


Figure 7.1: The level sets of u_1 , ω_1 in Case 1 at $t = 1.76 \times 10^{-4}$ (first row) and $t = 1.764 \times 10^{-4}$ (second row). There oscillations begin to appear at $t = 1.76 \times 10^{-4}$ and become severer at $t = 1.764 \times 10^{-4}$.

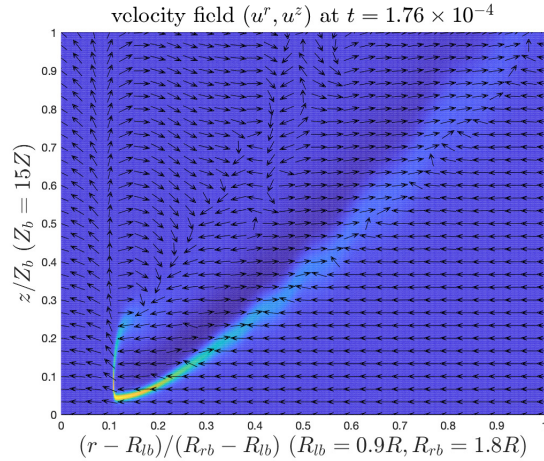


Figure 7.2: Directions of the velocity (u^r, u^z) (vectors) and the profile of ω_1 (background color map) in rescaled coordinates at $t = 1.76 \times 10^{-4}$. The velocity field has a strong shearing along the tail of ω_1 .

coefficients in the region of interest become smaller and smaller. The viscosity in the tail part of the solution is then too weak to control the shearing instability in the late stage of the computation.

7.2. Controlling the oscillations. We have argued in Section 3.5 that the strong coupling effect (3.2) at the front part of the solution around $(R(t), Z(t))$ is the major driving mechanism for a potential

sustainable blowup. The long tail structure of the solution is only a subordinate phenomenon that is left behind by the traveling blowup front. However, the mild oscillations that mainly appear at the tail part may affect and even jeopardize the blowup of the front in two ways. First, the inward flow (towards $r = 0$) below the tail may back propagate the oscillations to the front and eventually weaken the delicate blowup mechanism at the front. Second, since ψ_1 couples with ω_1 globally through the Poisson equation (2.3c), the local instability in ω_1 at the tail part can trigger global instability in ψ_1 , which may weaken or harm the critical alignment between u_1 and $\psi_{1,z}$ near $(R(t), Z(t))$.

Therefore, in order to obtain a stable blowup solution in our scenario for a longer time, we need to apply some numerical regularization to control and suppress the oscillations in the tail region. This is why we implement the stronger smoothing operation, the re-meshed low-pass filter RLPF_c^k , in our Case 3 computation. In particular, we choose the filtering strength function $c(\rho, \eta)$ to be the “L” shape function (A.8) that mainly affect the phase 2 region of the adaptive mesh. This is because the tail part of the solution is covered in the phase 2 region by the design of our adaptive mesh. Moreover, we only apply the RLPF to the variables $\psi_{1,r}, \psi_{1,z}$ that are used to compute the velocity (u^r, u^z) via (2.3d), so that the shearing effect of the velocity field near the tail part can be smoothed out.

To study the effect of the RLPF in suppressing the oscillations in the tail region, we compare the solutions computed in Case 3 with different numbers of RLPF_c^k beyond $t = 1.76 \times 10^{-4}$. Figure 7.3 plots the level sets of u_1 at 1.764×10^{-4} obtained from computations with different k in RLPF_c^k . One should compare Figure 7.3 with Figure 7.1 and see that (i) the RLPF effectively suppresses the oscillations in the tail region that occurs beyond $t = 1.76 \times 10^{-4}$, and (ii) a larger number of RLPF gives a stronger smoothing effect, leading to a smoother solution. This shows that our RLPF smoothing operation can successfully stabilize the potential blowup solution in the very late stage of computation.

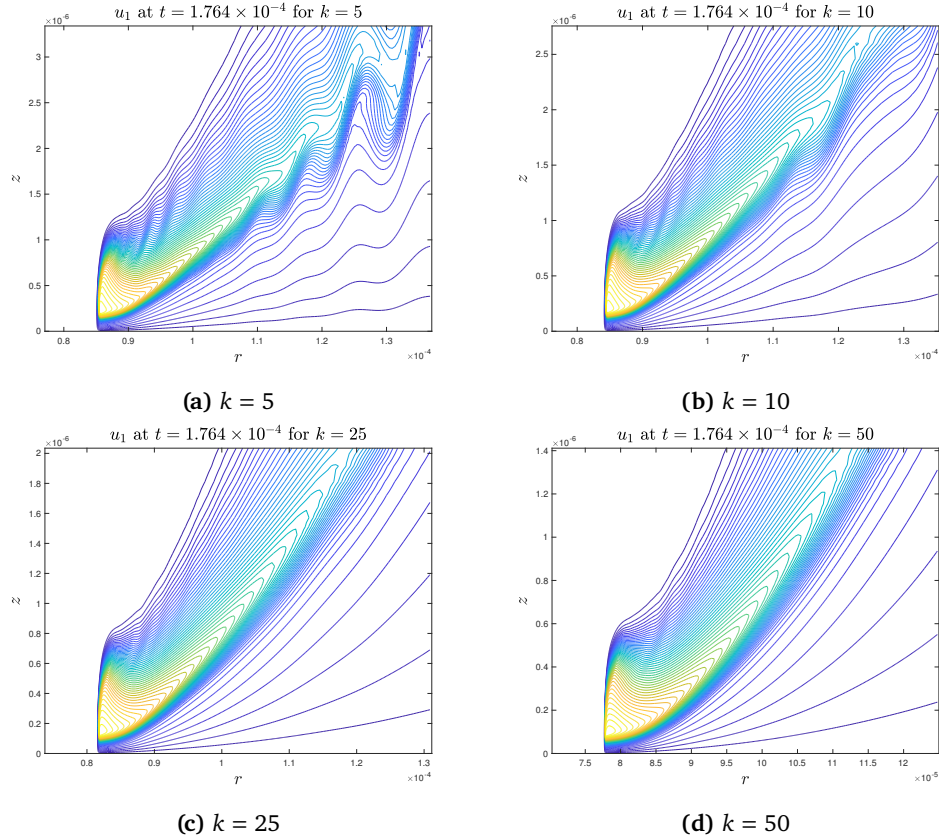


Figure 7.3: Profiles of u_1 under different strength of RLPF (different k in RLPF_c^k).

Given the powerful effect of RLPF in controlling the oscillations in the tail region, one may raise a nature question: does the RLPF also suppress the potential blowup in addition to suppressing the oscillations? According to our observation and understanding of the computation, the answer is no. The “L” shape design of the strength function $c(\rho, \eta)$ in RLPF_c^k ensures that the effect of RLPF does not directly affect the front part of the solution. Indeed, the RLPF only smooths out the velocity field of u^r, u^z at the tail part that is away from the crucial blowup region around $(R(t), Z(t))$.

More interestingly, the application of RPLF even helps with the blowup by stabilizing the driving mechanism. To see this, we compare in Figure 7.4 the growth of $\|\omega\|_{L^\infty}, R(t)^{-1}, Z(t)^{-1}$ in Case 1 and in Case 3 using different numbers of RLPF. Figure 7.4(a) shows that the stronger RLPF we apply, the faster $\|\omega\|_{L^\infty}$ grows up to the same time. Figure 7.4(b) and (c) show that the maximum location $(R(t), Z(t))$ of u_1 approaches the origin faster with a stronger RLPF. Moreover, we report in Table 7.1 the amplification of the quantities $\|u_1\|_{L^\infty}, \|\omega_1\|_{L^\infty}, \|\omega\|_{L^\infty}$ up to $t = 1.76 \times 10^{-4}$ for different numbers of RLPF, which further confirms that applying the RLPF actually favors the blowup of the solution.

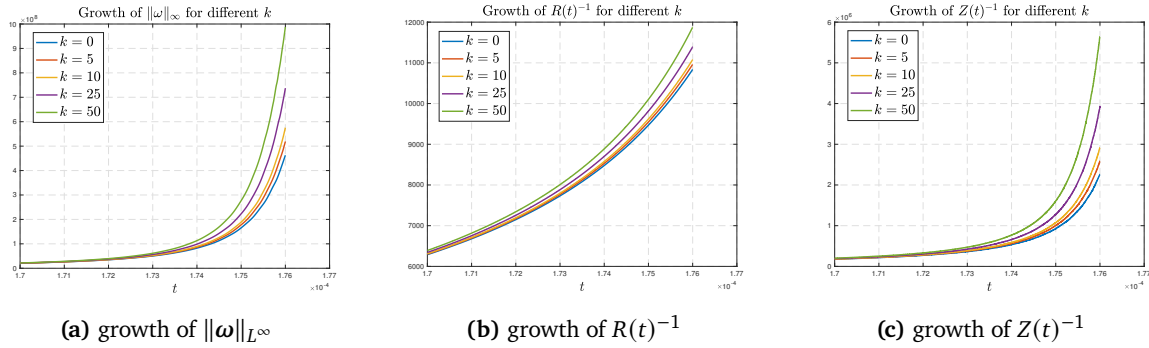


Figure 7.4: The growth of $\|\omega\|_{L^\infty}, R(t)^{-1}, Z(t)^{-1}$ with different numbers of RLPF. The last time instant shown in the figure is $t = 1.76 \times 10^{-4}$.

k	$\ u_1(t)\ _{L^\infty} / \ u_1(0)\ _{L^\infty}$	$\ \omega_1(t)\ _{L^\infty} / \ \omega_1(0)\ _{L^\infty}$	$\ \omega(t)\ _{L^\infty} / \ \omega(0)\ _{L^\infty}$
0	9.0814×10^1	2.1802×10^4	3.3227×10^3
5	9.2917×10^1	2.4480×10^4	3.7277×10^3
10	9.4875×10^1	2.7144×10^4	4.1343×10^3
25	1.0023×10^2	3.5007×10^4	5.2966×10^3
50	1.0858×10^2	4.8301×10^4	7.0959×10^3

Table 7.1: Amplification of $\|u_1\|_{L^\infty}, \|\omega_1\|_{L^\infty}, \|\omega\|_{L^\infty}$ up to $t = 1.76 \times 10^{-4}$.

These results imply that the RPLF has a positive effect on the potential blowup even before the oscillations in the tail region occur. It is very likely that the the solution has already developed some mild instability that is not yet visible before $t = 1.76 \times 10^{-4}$. This mild instability may have generated some minor influence on the blowup in the stable phase. The application of the RLPF helps suppress this mild instability throughout the entire computation. In the meanwhile, the RLPF does not harm the coupling blowup mechanism in the most singular region near the sharp front as discussed in Section 3.5. This confirms that maintaining this coupling blowup mechanism is crucial for our potential blowup at the origin.

8. CONCLUDING REMARKS

In this paper, we presented strong numerical evidences that the 3D axisymmetric Navier–Stokes equations with degenerate variable diffusion coefficients develop a finite time singularity at the origin. An important feature of this potential singularity is that the solution develops a two-scale traveling wave solution that travels towards the origin. The antisymmetric vortex dipoles and the odd symmetry in the initial data generate a strong shear flow that pushes the solution travels towards the symmetry plane $z = 0$ rapidly. The flow is then transported towards the symmetry axis $r = 0$ by the strong negative radial velocity induced by the vortex dipoles. The hyperbolic flow structure near the center of the traveling wave generates a vacuum region dynamically. The flow evolves into a local “two-phase” flow that separates the “vacuum phase” from the fluid phase by a “moving boundary”. The special design of our initial data and the dynamic formation of this vacuum region generate a positive feedback loop that enforces strong nonlinear alignment in vortex stretching, leading to a potential locally self-similar blowup at the origin. We performed careful resolution study and asymptotic scaling analysis to provide further support of the potential locally self-similar blowup.

The degeneracy of the variable diffusion coefficients at the origin plays an essential role in stabilizing this potential singularity formation for the incompressible 3D Navier–Stokes equations. We have also studied the incompressible Navier–Stokes equations with constant diffusion coefficient using the same initial data. Our numerical study revealed that the constant coefficient diffusion regularizes the smaller scale of the two-scale traveling wave solution and destabilizes the nonlinear alignment in the vortex stretching term. The solution of the Navier–Stokes equation with constant diffusion coefficient behaves completely differently. We did not observe the finite time singularity formation that we observed for the Navier–Stokes equations with degenerate variable diffusion coefficients.

A natural follow-up work would be to investigate the potential singular solutions of the 3D axisymmetric Euler equations using the same initial data. Our study showed that u_1 corresponding to the Euler equations developed a very sharp front along the r direction and extremely large gradient along the z direction. This phenomena occurred in the early stage of the computation before the nonlinear vortex stretching had a chance to develop a strong alignment. Without viscous regularization, the smaller scale $Z(t)$ seemed to approach to zero much faster than $O(T - t)$. In the case of the Navier–Stokes equations with degenerate diffusion coefficients, it is the balance between the vortex stretching and the degenerate diffusion coefficients that selects a length scale for $Z(t)$. Without the viscous regularization, we may not be able to select a length scale for $Z(t)$.

To overcome this difficulty, we have designed a first order numerical viscosity to regularize the solution of the 3D Euler equation. The first order numerical viscosity is based on our local adaptive mesh. We only apply the numerical viscosity in the near field corresponding to length scale $Z(t)$ and the intermediate field corresponding to length scale $R(t)$, which covers the tail region. But we turn off the numerical viscosity in the far field corresponding to the $O(1)$ length scale. Our adaptive mesh strategy is designed to resolve the smaller length scale $Z(t)$ in the near field. Thus, the numerical viscosity in the most singular region is very weak and is proportional to $Z(t)$. But the numerical viscosity is relatively large in the tail region due to the relatively coarse grid there. The numerical viscosity plays a role similar to that of the degenerate variable diffusion coefficients in the Navier–Stokes equations. We observed a locally self-similar blowup solution with blowup rates similar to those that we obtained for the Navier–Stokes equations with degenerate variable diffusion coefficients.

To gain further understanding the Euler blowup scenario, we have applied a similar scaling analysis to the incompressible Euler equations with first order numerical viscosity. The balance between the vortex stretching term and the numerical diffusion term also gives $Z(t) = O(R(t)^2)$. Thus, the numerical viscosity is of the same order as that of the degenerate variable diffusion coefficients of the Navier–Stokes equations in the most singular region. This explains why we obtained the same scaling

properties for the Euler equations as those for the Navier–Stokes equations with degenerate variable diffusion coefficients. In some sense, by adding a first order numerical viscosity to the incompressible Euler equations, we actually compute the solution of the Euler equations in the vanishing viscosity limit. We will report these findings in our upcoming paper.

Our current computation still suffers from two limitations. The first one is that our adaptive mesh strategy would break down in the limit of $R(t)/Z(t) \rightarrow \infty$. We need to develop a more effective adaptive mesh strategy to overcome this difficulty. The second one is that as we approach the singularity time, the shearing induced oscillations in the tail region become more severe. We need to apply stronger filtering in the tail region to control these oscillations in the tail region, which compromises the accuracy of our computation unless we use a very fine mesh.

As we discussed in our paper, the vacuum region effectively generates a “two-phase” flow. If we can approximate the solution of the Navier–Stokes equations with degenerate variable diffusion coefficients by a single phase flow with a moving boundary, then we do not need to resolve the sharp front that separates the vacuum phase from the fluid phase. This will save us a lot of computational effort to resolve the sharp front in u_1 and the regularized 1D delta function in ω_1 along the “moving boundary”. By modeling the flow as a single phase flow with a moving boundary, we may be able to develop a dynamic rescaling formulation with appropriately designed normalization conditions to eliminate a few dynamically unstable modes that are responsible for the dynamic generation of the oscillations in the tail region. We will pursue this line of research in our future work.

Acknowledgments. The research was in part supported by NSF Grants DMS-1907977 and DMS-1912654. DH gratefully acknowledges the supports from the Choi Family Postdoc Gift Fund.

APPENDIX A. THE NUMERICAL METHODS

In this appendix, we describe the numerical method that we use to compute the potential finite-time singularity of the initial-boundary value problem (2.3)–(2.6). In our scenario, the solution profiles shrink in space and quickly develop complex geometric structures, which makes it extremely challenging to compute the numerical solution accurately. In order to overcome this difficulty, we have designed in Appendix A.1 a special adaptive mesh strategy to resolve the singularity formation near the origin $(r, z) = (0, 0)$. Based on the adaptive mesh, a B-spline based Galerkin Poisson solver is introduced in Appendix A.2 for solving the Poisson problem (2.3c). In Section A.4, we introduce the numerical regularization techniques that we use to control the mild oscillations in the solution, especially in the late stage of our computation. The overall numerical algorithm is outlined in Appendix A.5.

A.1. The adaptive (moving) mesh algorithm. To effectively and accurately compute the potential blowup, we have carefully designed a special meshing strategy that is dynamically adaptive to the more and more singular structure of the solution. The adaptive mesh covering the half-period computational domain $\mathcal{D}_1 = \{(r, z) : 0 \leq r \leq 1, 0 \leq z \leq 1/2\}$ is characterized by a pair of analytic mesh mapping functions

$$r = r(\rho), \quad \rho \in [0, 1]; \quad z = z(\eta), \quad \eta \in [0, 1].$$

These mesh mapping functions are both monotonically increasing and infinitely differentiable on $[0, 1]$, and satisfy

$$r(0) = 0, \quad r(1) = 1, \quad z(0) = 0, \quad z(1) = 1/2.$$

In particular, we construct these mapping functions by carefully designing their Jacobians/densities

$$r_\rho = r'(\rho), \quad z_\eta = z'(\eta),$$

using analytic functions that are even functions at 0. The even symmetries ensure that the resulting mesh can be smoothly extended to the full-period cylinder $\{(r, z) : 0 \leq r \leq 1, -1/2 \leq z \leq 1/2\}$.

The density functions contain a small number of parameters, which are dynamically adjusted to the solution. Once the mesh mapping functions are constructed, the computational domain is covered with a tensor-product mesh:

$$\mathcal{G} = \{(r_i, z_j) : 0 \leq i \leq n, 0 \leq j \leq m\}, \quad (\text{A.1})$$

where $r_i = r(ih_\rho)$, $h_\rho = 1/n$; $z_j = z(jh_\eta)$, $h_\eta = 1/m$. The precise definition and construction of the mesh mapping functions are described in Appendix B.

Figure A.1 gives an example of the densities r_ρ, z_η (in log scale) we use in the computation. As we will see in Section 3.1, the blowup solution of the initial-boundary value problem (2.3)–(2.6) develops a sharp front in the r direction and a thin profile of two spatial scales: (i) the smaller scale corresponds to the inner profile near the sharp front, and (ii) the larger scale corresponds to the outer profile of the traveling wave. Correspondingly, we design the densities r_ρ, z_η to have three phases:

- Phase 1 covers the inner profile of the smaller scale near the sharp front;
- Phase 2 covers the outer profile of the larger scale of the traveling wave;
- Phase 3 covers the (far-field) solution away from the symmetry axis $r = 0$.

Moreover, we have observed that there is a “vacuum” region between the sharp front and the symmetry axis $r = 0$ where the solutions u_1, ω_1 are smooth and extremely small. Hence, we add a phase 0 in the density r_ρ of the r direction to cover this region. In our computation, the number (percentage) of mesh points in each phase are fixed, but the physical location of each phase will change in time, dynamically adaptive to the structure of the solution. Between every two neighboring phases, there is also a smooth transition region that occupies a fixed percentage of mesh points.

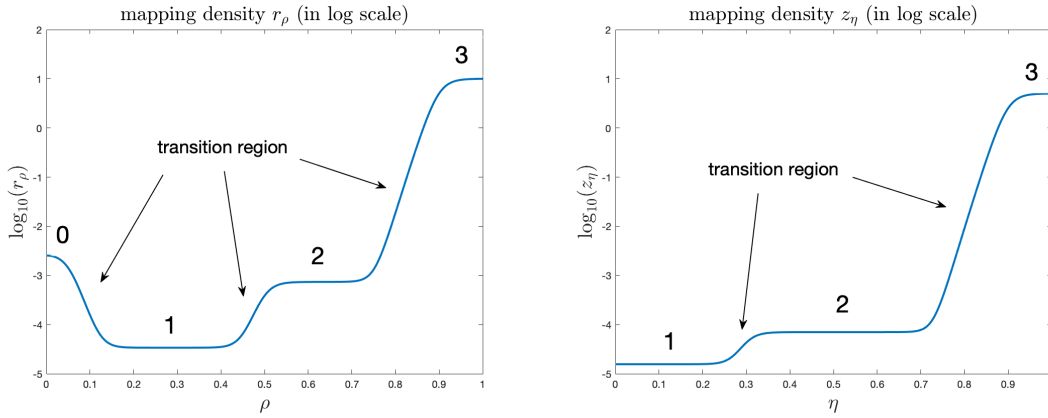


Figure A.1: The mapping densities r_ρ (left) and z_η (right) with phase numbers labeled.

The adaptive mesh is evolved using the following procedure. Given a reference time t_0 , we first use the solution at t_0 to construct an adaptive mesh \mathcal{G}_0 . To do so, we need to construct the mapping densities r_ρ, z_η that are adaptive to the reference solution. We find the maximum location $(R(t_0), Z(t_0))$ of $u_1(r, z, t_0)$ and find the coordinate $R_r(t_0)$ such that

$$u_{1,r}(R_r(t_0), Z(t_0), t_0) = \max_{0 \leq r \leq 1} u_{1,r}(r, Z(t_0), t_0).$$

We use $d_r(t_0) := R(t_0) - R_r(t_0)$ as the feature size of the smaller scale ($R(t_0)$ is always greater than $R_r(t_0)$ in our computation). Let $[\rho_1, \rho_2] \subset [0, 1]$ denote the interval of phase 1 in r_ρ , and let ρ_3 denote the right end point of phase 2. We then choose the parameters in r_ρ such that

- the most singular region $[R_r(t_0) - d_r(t_0), R(t_0) + d_r(t_0)]$ of the solution in the r direction is contained in the interval $[r(\rho_1), r(\rho_2)]$, and
- the larger scale $[0, 3R(t_0)]$ is within the outer boundary of phase 2, i.e. $3R(t_0) \leq r(\rho_3)$.

Let $[0, \eta_2] \subset [0, 1]$ denote the interval of phase 1 in z_η , and let η_3 denote the right end point of phase 2. Similar, we choose the parameters in z_η such that

- the most singular region $[0, (3/2)Z(t_0)]$ of the solution in the z direction is contained in the interval $[0, z(\eta_2)]$, and
- the larger scale $[0, 15Z(t_0)]$ is within the outer boundary of phase 2, i.e. $15Z(t_0) \leq z(\eta_3)$.

With the adaptive mesh \mathcal{G}_0 constructed using the reference solution at time t_0 , we compute the solution of equations (2.3) forward in time, until at some time t_1 at least one of the following happens:

- (i) the region $[R_r(t_1) - s_r(t_1), R(t_1) + s_r(t_1)]$ is no longer contained in the interval $[r(\rho_1), r(\rho_2)]$;
- (ii) the region $[0, (3/2)Z(t_1)]$ is no longer contained in the interval $[0, z(\eta_2)]$;
- (iii) the number of mesh points in the region $[R_r(t_1), R(t_1)]$ drops below a certain value;
- (iv) the number of mesh points in the region $[0, Z(t_1)]$ drops below a certain value.

Then we use t_1 as the new reference time and construct a new adaptive mesh G_1 using the solution at t_1 with the same strategy. The solution is interpolated from G_0 to G_1 in the $\rho\eta$ -space using a 4th-order piecewise polynomial interpolation in both directions. We denote this interpolation operation by

$$\hat{f} = \text{IP}_4(f; \mathcal{G}_0, \mathcal{G}_1), \quad (\text{A.2})$$

where f is a discrete function on \mathcal{G}_0 while \hat{f} is a discrete function on \mathcal{G}_1 . In what follows, we will always use the 4th-order piecewise polynomial interpolation in the $\rho\eta$ -space when we need to interpolate the solution from one mesh to another. In summary, the computation is carried out on a mesh that is constructed with respect to the reference solution at the latest reference time, and the reference time is replaced by the current time when one of the mesh update criteria is satisfied.

We remark that the mesh update criteria described above are designed to ensure that the most singular part of the solution is covered and well resolved in the finest phase 1 region of the adaptive mesh. In our computation, we choose the parameters in r_ρ, z_η such that the partitioning of different phases is given by (as shown in Figure A.1)

$$\begin{aligned} r_\rho : \quad & \text{phase 0 : } [0, 0.1], \quad \text{phase 1 : } [0.1, 0.5], \quad \text{phase 2 : } [0.5, 0.85], \quad \text{phase 3 : } [0.85, 1], \\ z_\eta : \quad & \text{phase 1 : } [0, 0.3], \quad \text{phase 2 : } [0.3, 0.85], \quad \text{phase 3 : } [0.85, 1]. \end{aligned}$$

Therefore, the most singular part of the solution is covered in $[0.05, 0.5] \times [0, 0.3]$ in the $\rho\eta$ -space.

The mesh adaptation strategy described above has several advantages compared with the conventional moving mesh method. First of all, it can automatically resolve a blowup solution regardless of its spatial scalings. This is crucial to the success of our computation, because the solution evolves rapidly in time. Secondly, the method always places enough mesh points outside the most singular region, ensuring a well-behaved and stable mesh. Thirdly, the analytic representation of the mapping densities ensures accurate approximations of space derivatives, greatly improving the quality of the computation.

A.2. The B-Spline based Galerkin Poisson solver. One crucial step in our computation is to solve the Poisson problem (2.3c) accurately. The Poisson solver we use should be compatible to the our adaptive mesh setting. Moreover, the finite dimensional solver needs to be easy to construct from the mesh, as the mesh is updated frequently in our computation. For these reasons, we choose to implement the Galerkin finite element method based on a tensorization of B-spline functions. In fact, this framework has been used by Luo and Hou [LH14b] to compute the potential singularity formation of the 3D axisymmetric Euler equations on the solid boundary. The equations they computed are exactly the equations (2.3) with zero viscosity ($\nu = 0$). In their computation, an adaptive moving mesh strategy was also adopted for resolving a focusing blowup solution, and the B-Spline based Galerkin Poisson solver was found to be very effective and stable.

We will follow the framework and notations in [LH14b]. The Poisson equation (2.3c) is solved in the $\rho\eta$ -space in the following procedure. First, the equation is rewritten in the $\rho\eta$ -coordinates:

$$-\frac{1}{r^3 r_\rho} \left(r^3 \frac{\psi_\rho}{r_\rho} \right)_\rho - \frac{1}{z_\eta} \left(\frac{\psi_\eta}{z_\eta} \right)_\eta = \omega, \quad (\rho, \eta) \in [0, 1]^2,$$

where for clarity we have written ψ for ψ_1 and ω for ω_1 (only in this section). Next, the equation is multiplied by $r^3 r_\rho z_\eta \phi$ for some suitable test function $\phi \in V$ (to be defined below) and is integrated over the domain $[0, 1]^2$. After integration by part, this yields the weak formulation of the Poisson equation (2.3c): find $\psi \in V$ such that

$$\begin{aligned} a(\psi, \phi) &:= \int_{[0,1]^2} \left(\frac{\psi_\rho}{r_\rho} \frac{\psi_\rho}{r_\rho} + \frac{\psi_\eta}{z_\eta} \frac{\phi_\eta}{z_\eta} \right) r^3 r_\rho z_\eta \, d\rho \, d\eta \\ &= \int_{[0,1]^2} \omega \phi r^3 r_\rho z_\eta \, d\rho \, d\eta =: f(\phi), \quad \forall \phi \in V, \end{aligned}$$

where the function space V is given by (recall the symmetry properties of ψ)

$$\begin{aligned} V = \text{span} \left\{ \phi \in H^1([0, 1]^2) : \phi(-\rho, \eta) = \phi(\rho, \eta), \phi(1, \eta) = 0, \right. \\ \left. \phi(\rho, -\eta) = -\phi(\rho, \eta), \phi(\rho, 1 - \eta) = -\phi(\rho, 1 + \eta) \right\}. \end{aligned} \quad (\text{A.3})$$

To introduce the Galerkin approximation, we define the finite-dimensional subspace of weighted uniform B-splines (Höllig [Höl03]) of even order k :

$$V_h := V_{w,h}^k = \text{span} \left\{ w(\rho) b_{i,h_\rho}^k(\rho) b_{j,h_\eta}^k(\eta) \right\} \cap V,$$

where $w(\rho) = (1 - \rho)^2$, $\rho \in [0, 1]$ is a nonnegative weight function that is vanishing on $\rho = 1$, and

$$b_{l,h}^k(s) = b^k((s/h) - (l - k/2)), \quad s \in [0, 1], \quad l \in \mathbb{Z},$$

is the shifted and rescaled uniform B-spline of order k . Here b^k are the standard B-spline functions that satisfy the recursion ([Höl03])

$$b^1(x) = \begin{cases} 1, & x \in [0, 1] \\ 0, & x \notin [0, 1] \end{cases}; \quad b^k(x) = \int_{x-1}^x b^{k-1}(y) \, dy, \quad k \geq 2.$$

The Galerkin finite element method then finds $\psi_h \in V_h$ such that

$$a(\psi_h, \phi_h) = f(\phi_h), \quad \forall \phi_h \in V_h. \quad (\text{A.4})$$

With suitably chosen basis functions of V_h , this leads to a symmetric, positive definite linear system $Ax = b$ which can be solved to yield the Galerkin solution ψ_h . In particular, we choose the finite element basis of V_h to be

$$B_{i,j}^w(\rho, \eta) := w(\rho) B_i(\rho) B_j(\eta), \quad 0 \leq i \leq n + k/2 - 1, \quad 1 \leq j \leq m - 1,$$

where

$$B_i(\rho) = \frac{b_{i,h_\rho}^k(\rho) + b_{i,h_\rho}^k(-\rho)}{1 + \delta_{i0}}, \quad B_j(\eta) = b_{j,h_\eta}^k(\eta) - b_{j,h_\eta}^k(-\eta) - b_{j,h_\eta}^k(2 - \eta).$$

If we write the finite element solution as

$$\psi_h = \sum_{i,j} c_{ij} B_{ij}^w(\rho, \eta),$$

the variational problem (A.4) is transformed to an equivalent linear system of the coefficient $\{c_{ij}\}$:

$$\sum_{ij} a(B_{i'j'}^w, B_{ij}^w) c_{ij} = f(B_{i'j'}^w), \quad \text{for all } 0 \leq i' \leq n + k/2 - 1, 1 \leq j' \leq m - 1.$$

In our implementation, the entries $a(B_{i'j'}^w, B_{ij}^w)$ of the stiffness matrix and the entries $f(B_{i'j'}^w)$ of the load vector are approximated using the composite 6-point Gauss–Legendre quadrature rule. The resulting sparse linear system is then solved using the built-in linear solver of MATLAB R2019a.

In our computation, we choose $k = 2$. It is observed that the corresponding Poisson solver is at least 2nd-order convergent for the stream function ψ_1 . We will explain why we choose to use a 2nd-order method in Appendix A.4. For more detailed error analysis of the B-Spline based Galerkin Poisson solver, one may refer to [Hölo3, LH14b].

A.3. Spatial derivatives. To solve the equations (2.3) in time, we also need to approximate the spatial derivatives of the solution. For the reason to be explained in Appendix A.4, we choose to use 2nd-order centered difference schemes with respect to the $\rho\eta$ -coordinates. Let v be some solution variable. For example, the first and the second derivatives of v in r are approximated as

$$(v_r)_{i,j} = \frac{(v_\rho)_{i,j}}{(r_\rho)_i} \approx \frac{1}{(r_\rho)_i} \cdot \frac{v_{i+1,j} - v_{i-1,j}}{2h_\rho}, \quad (\text{A.5a})$$

$$(v_{rr})_{i,j} = \frac{(v_{\rho\rho})_{i,j}}{(r_\rho)_i^2} - \frac{(r_{\rho\rho})_{i,j}(v_\rho)_{i,j}}{(r_\rho)_i^3} \approx \frac{1}{(r_\rho)_i^2} \cdot \frac{v_{i+1,j} - 2v_{i,j} + v_{i-1,j}}{h_\rho^2} - \frac{(r_{\rho\rho})_{i,j}}{(r_\rho)_i^3} \cdot \frac{v_{i+1,j} - v_{i-1,j}}{2h_\rho}. \quad (\text{A.5b})$$

Note that $r_{\rho\rho}$ can be computed directly from our analytic formula of r_ρ without approximation. This is crucial for the accurate evaluation of v_r, v_{rr} , especially in the smaller scale regions where the mesh density r_ρ is close to 0.

The centered difference formulas described above need to be supplemented by numerical boundary conditions near $\rho, \eta = 0, 1$. In particular, we can make use of the symmetry properties (2.5) of the solution. Suppose that $v = u_1$. In the η direction, the odd symmetry conditions

$$v_{i,-1} = -v_{i,1}, \quad v_{i,m+1} = -v_{i,m-1}, \quad 0 \leq i \leq n,$$

are used at $\eta = 0$ and $\eta = 1$. In the ρ direction, the even symmetry

$$v_{-1,j} = v_{1,j}, \quad 0 \leq j \leq m,$$

is used at $\rho = 0$, and the extrapolation condition

$$v_{n+1,j} = 3v_{n,j} - 3v_{n-1,j} + v_{n-2,j}, \quad 0 \leq j \leq m,$$

is applied near the solid boundary $\rho = 1$ when necessary. The extrapolation condition is known to be GKS stable for linear hyperbolic problems (Gustafsson et al., [GKO95]), and is expected to remain stable when applied to the NSE equations as long as the underlying solution is sufficiently smooth. Moreover, the no-slip boundary condition (2.5f) will also be enforced:

$$(u_1)_{n,j} = 0, \quad (\omega_1)_{n,j} = -(\psi_{1,rr})_{n,j}, \quad 0 \leq j \leq m.$$

We remark that the function ψ_1 is very smooth in the $\rho\eta$ -coordinates since it is recovered from ω_1 through the Poisson equation (2.3c). Correspondingly, the numerical solution of ψ_1 obtained from the 2nd-order finite element method in Appendix A.2 will have a smooth error expansion. The expected order of accuracy thus will not be compromised when computing the derivatives of ψ_1 using the 2nd-order centered difference schemes (A.5). In particular, the computation of the velocities u^r, u^z (via formulas (2.3d)) should also be 2nd-order accurate, which has been verified in Section 4.2.

A.4. Numerical regularization. The potential blowup solution we compute develops a long thin tail structure, stretching from the sharp front to the far field. This tail structure develops some mild oscillations in the late stage of the computation, and may affect the blowup mechanism. Therefore, we have chosen to apply some numerical regularization techniques to stabilize the solution, especially the tail part of the solution.

Consider the computational mesh \mathcal{G} (A.1) that is constructed with respect to the latest reference time. Let $f = (f_{i,j})$ be the discretization of some solution variable. The first numerical regularization technique we use is a local smoothing operation:

$$\begin{aligned}\tilde{f}_{i,j} &= f_{i,j} + \frac{c(\rho_i, \eta_j)}{4} (f_{i-1,j} + f_{i+1,j} - 2f_{i,j}), \\ (\text{LPF}_c(f))_{i,j} &= \tilde{f}_{i,j} + \frac{c(\rho_i, \eta_j)}{4} (\tilde{f}_{i,j-1} + \tilde{f}_{i,j+1} - 2\tilde{f}_{i,j}),\end{aligned}\tag{A.6}$$

where $c(\rho, \eta) : [0, 1]^2 \mapsto [0, 1]$ is a nonnegative weight functions. To define $(\text{LPF}_c(f))_{i,j}$ near the boundaries $\rho, \eta = 0, 1$, we need to use numerical boundary conditions discussed in Appendix A.1. This smoothing operation can be seen as a low-pass filtering in the $\rho\eta$ -space. It can also be viewed as solving a heat equation for one step in the $\rho\eta$ -space. The weight function $c(\rho, \eta)$ measures how strong the smoothing effect is; the smoothing effect can have different strength at different part of the solution, depending on the value of $c(\rho, \eta)$. We will use $\text{LPF}_c^k(\cdot)$ to denote the operation of applying k times of LPF_c . Note that this low-pass filtering will introduce a 2nd-order error of size $O(h_\rho^2 + h_\eta^2)$.

The second numerical regularization technique is a variant of LPF_c . The low-pass filtering LPF_c is sometimes too weak to control the mild oscillations occurring in the tail part of the solution. We therefore design a stronger smoothing operation. Instead of directly applying the low-pass filtering on the mesh \mathcal{G} , we first interpolate a solution variable f at the current time t to a coarse mesh

$$\mathcal{G}^c = \{(\hat{r}_i, \hat{z}_j) : 0 \leq i \leq N, 0 \leq j \leq M\},$$

where

$$\hat{r}_i = \hat{r}(i\hat{h}_\rho), \quad \hat{h}_\rho = 1/N; \quad \hat{z}_j = \hat{z}(j\hat{h}_\eta), \quad \hat{h}_\eta = 1/M.$$

This mesh \mathcal{G}^c is constructed with respect to the solution at the current time t (not with respect to the latest reference time), and thus the mesh maps \hat{r}, \hat{z} are adaptive to the current solution. We say that \mathcal{G}^c is coarser than \mathcal{G} in the sense that $N \leq n, M \leq m$. Then we perform k times of the low-pass filtering LPF_c on the coarser mesh \mathcal{G}^c . Here k is a parameter. Afterwards, we interpolate the smoothed variable back to the finer computational mesh \mathcal{G} . This smoothing procedure, named as re-meshed low-pass filtering, can be summarized as follows:

$$\hat{f} = \text{IP}_4(f, \mathcal{G}, \mathcal{G}^c), \quad \tilde{f} = \text{LPF}_c^k(\hat{f}), \quad \text{RLPF}_c^k(f) = \text{IP}_4(\tilde{f}, \mathcal{G}^c, \mathcal{G}).\tag{A.7}$$

This procedure will introduce an error of size $O(\hat{h}_\rho^2 + \hat{h}_\eta^2)$.

In our computations, we will use $n = 2m$ and $N = M = m$. Therefore, the overall error introduced by the re-meshed low-pass filtering is still second order in (h_ρ, h_η) .

A.5. The overall algorithm. Given an adaptive mesh \mathcal{G} and the data (u_1, ω_1) defined on it, the numerical solution of equations (2.3) is advanced in time via the following procedure.

- (1) The Poisson equation (2.3c) is solved for ψ_1 using the 2nd-order B-spline based Galerkin method introduced in Appendix A.2.
- (2) The spacial derivatives are computed using the 2nd-order centered difference schemes introduced in Appendix A.3 and (u^r, u^z) is evaluated at the grid points using (2.3d).
- (3) An adaptive time step size δ_t is computed on \mathcal{G} so that the CFL condition is satisfied with a suitably small CFL number (e.g. 0.1):

$$\begin{aligned}\delta_{t,1} &= 0.1 \min \left\{ \min_{\rho, \eta} \frac{h_\rho r_\rho}{u^r}, \min_{\rho, \eta} \frac{h_\eta z_\eta}{u^z} \right\}, \quad (\text{stability for the convection}) \\ \delta_{t,2} &= 0.1 \min \left\{ \min_{\rho, \eta} \frac{(h_\rho r_\rho)^2}{\nu^r}, \min_{\rho, \eta} \frac{(h_\eta z_\eta)^2}{\nu^z} \right\}, \quad (\text{stability for the diffusion}) \\ \delta_t &= \min\{\delta_{t,1}, \delta_{t,2}\}.\end{aligned}$$

We remark that with this choice of δ_t , the relative growth of the maximum value of the solution in one step is observed to remain below 1%.

- (4) The solution (u_1, ω_1) is advanced in time by δ_t using a 2nd-order explicit Runge–Kutta method.
- (5) The mesh \mathcal{G} is updated if necessary (Appendix A.1).

It can be shown that the overall algorithm without numerical regularization is formally 2nd-order accurate in space and in time.

To control the mild oscillations in the tail region in the late stage of the computation, we will apply numerical regularizations in our computations as described in Appendix A.4. In particular, we will do the following each time when we update the *time derivatives* of u_1, ω_1 in equations (2.3). At the beginning of each iteration, we apply to the solution variables u_1, ω_1 one time low-pass filtering (A.7) with uniform strength $c(\rho, \eta) = 0.1$ and then one time low-pass filtering with strength function $c(\rho, \eta) = c_L(\rho, \eta)$:

$$\tilde{u}_1 = \text{LPF}_{c_L}(\text{LPF}_{0.1}(u_1)), \quad \tilde{\omega}_1 = \text{LPF}_{c_L}(\text{LPF}_{0.1}(\omega_1)).$$

The strength function $c_L(\rho, \eta)$ is given by

$$c_L(\rho, \eta) = \bar{f}_{sc}(\rho, 0.8, 0.05) \cdot \bar{f}_{sc}(\eta, 0.8, 0.05) \cdot (1 - \bar{f}_{sc}(\rho, 0.45, 0.05) \cdot \bar{f}_{sc}(\eta, 0.45, 0.05)), \quad (\text{A.8})$$

where $\bar{f}_{sc} = 1 - f_{sc}$ and the soft-cutoff function f_{sc} is given by (2.7). Figure A.2 shows the shape of the strength function $c(\rho, \eta)$. The point of using this “L” shape function $c(\rho, \eta)$ is to suppress the oscillations occurring at the tail part of the solution. We will use $\tilde{u}_1, \tilde{\omega}_1$ to compute the stream function ψ_1 and all the spatial derivatives. But when advancing the solution using the 2nd-order Runge–Kutta method, we still use the original u_1, ω_1 for solution evolution. That is,

$$(u_1(t + \delta_t), \omega_1(t + \delta_t)) = (u_1(t), \omega_1(t)) + F(\tilde{u}_1(t), \tilde{\omega}_1(t), \delta_t),$$

where $F(\tilde{u}_1(t), \tilde{\omega}_1(t), \delta_t)$ is the update of the solution in one time step.

Moreover, after solving the Poisson equation for ψ_1 (using $\tilde{\omega}_1$), we regularize ψ_1 by doing one time of low-pass filtering:

$$\psi_1 \leftarrow \text{LPF}_1(\psi_{1,r}).$$

Then we compute spatial derivatives $\psi_{1,r}, \psi_{1,z}$, and we regularize them by doing

$$\psi_{1,r} \leftarrow \text{LPF}_1(\text{RLPF}_c^k(\psi_{1,r})), \quad \psi_{1,z} \leftarrow \text{LPF}_1(\text{RLPF}_c^k(\psi_{1,z})).$$

This step is meant to regularize the velocity field in the tail part region of the solution, as the velocity is computed from ψ, ψ_r, ψ_z via (2.3d). We remark that we do not apply the stronger regularization RLPF_c^k directly to the solution variables u_1, ω_1 .

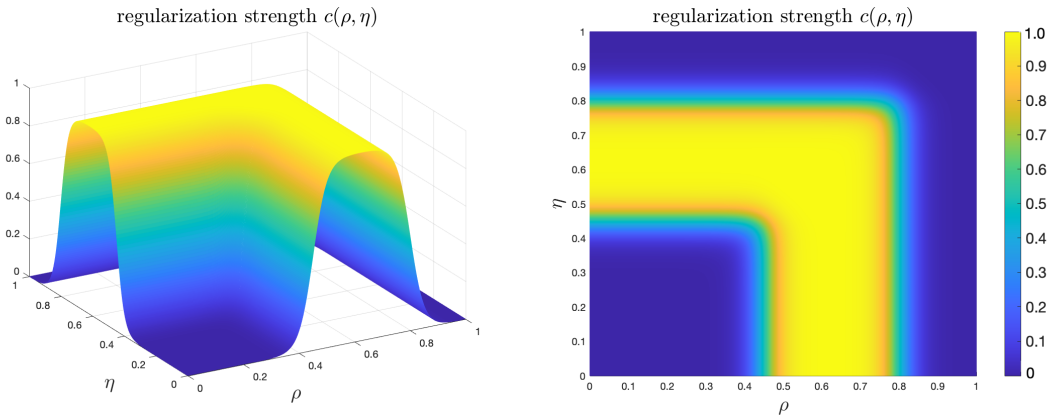


Figure A.2: The strength function $c(\rho, \eta)$ in the re-meshed low-pass filtering operation RLPF_c^k .

APPENDIX B. CONSTRUCTION OF THE ADAPTIVE MESH

In this appendix, we provide the details of the construction of our adaptive meshes. As mentioned in Appendix A.1, we will construct the mapping densities r_ρ, z_η using analytic functions. Then the mapping functions are given by

$$r(\rho) = \int_0^\rho r_\rho(s) ds, \quad z(\eta) = \int_0^\eta z_\eta(s) ds,$$

which can be computed explicitly using the analytic formulas of r_ρ, z_η . In particular, we use the following parametrized formulas for the mapping densities

$$r_\rho(s) = p(s; \mathbf{a}^\rho, \mathbf{s}^\rho), \quad z_\eta(s) = p(s; \mathbf{a}^\eta, \mathbf{s}^\eta),$$

where $\mathbf{a}^\rho = \{a_i^\rho\}_{i=0}^3, \mathbf{a}^\eta = \{a_i^\eta\}_{i=0}^3, \mathbf{s}^\rho = \{s_j^\rho\}_{j=1}^3, \mathbf{s}^\eta = \{s_j^\eta\}_{j=1}^3$ are parameters,

$$p(s; \mathbf{a}, \mathbf{s}) = a_1 + a_2 q_b(s - s_2) + a_3 q_b(s - s_3) + a_0 (q_b(s_1 - s) + q_b(s_1 + s) - 1), \quad s \in [0, 1], \quad (\text{B.1})$$

and

$$q_b(x) = \frac{(1+x)^b}{1 + (1+x)^b}, \quad x \in [-1, 1],$$

for some even integer b . We will determine the parameters by adjusting r_ρ, z_η to a reference solution. In what follows, we explain how to construct $r_\rho(s) = p(s; \mathbf{a}, \mathbf{s})$. The construction of z_η is similar.

It is not hard to see that, for a large integer b ,

$$q_b(x) \approx \mathbf{1}_{x \geq 0} := \begin{cases} 1, & x \in [0, 1], \\ 0, & x \in [-1, 0). \end{cases}$$

Therefore, we can choose b to be a large number and treat $q_b(x)$ ideally as the indicator function $\mathbf{1}_{x \geq 0}$. With this approximation, we have

$$p(s; \mathbf{a}, \mathbf{s}) \approx \hat{p}(s; \mathbf{a}, \mathbf{s}) := \begin{cases} a_0 + a_1, & s \in [0, s_1), \\ a_1, & s \in [s_1, s_2), \\ a_1 + a_2, & s \in [s_2, s_3), \\ a_1 + a_2 + a_3, & s \in (s_3, 1]. \end{cases} \quad (\text{B.2})$$

Note that $\hat{p}(s; \mathbf{a}, \mathbf{s})$ is formally an even function of s at $s = 0$ and at $s = 1$. In fact, when b is large enough, $p(s; \mathbf{a}, \mathbf{s})$ can be viewed as an even function of s at $s = 0$ and at $s = 1$ up to machine precision. In our computation, we choose $b = 60$.

The intervals $[0, s_1), [s_1, s_2), [s_2, s_3), [s_3, 1]$ stand for the 4 phases in $r_\rho(s)$. Therefore, the numbers $s_1, s_2 - s_1, s_3 - s_2, 1 - s_3$ are the percentages of mesh points that are allocated the 4 phases respectively. Throughout our computation, we choose s_1, s_2, s_3 to be some constants independent of the reference solution:

$$\begin{aligned} s_1^\rho &= 0.1, & s_2^\rho &= 0.5, & s_3^\rho &= 0.85, \\ s_1^\eta &= 0, & s_2^\eta &= 0.3, & s_3^\eta &= 0.85. \end{aligned}$$

The case of $s_1^\eta = 0$ corresponds to z_η having only three phases.

To determine the parameters \mathbf{a} , we need to use the information of the reference solution so that the mapping density $p(s; \mathbf{a}, \mathbf{s})$ is adaptive to it. This is done by determining the images of the 4 phases in the physical domain. Let $P(x; \mathbf{a}, \mathbf{s})$ be the mapping function corresponding to the density $p(s; \mathbf{a}, \mathbf{s})$,

$$P(x; \mathbf{a}, \mathbf{s}) = \int_0^x p(s; \mathbf{a}, \mathbf{s}) ds, \quad x \in [0, 1]. \quad (\text{B.3})$$

Let y denote a physical coordinate ($y = r$ or $y = z$). We will use the reference solution to determine some coordinates y_1, y_2, y_3 such that we want to make

$$P(s_1; \mathbf{a}, \mathbf{s}) = y_1, \quad P(s_2; \mathbf{a}, \mathbf{s}) = y_2, \quad P(s_3; \mathbf{a}, \mathbf{s}) = y_3, \quad P(1; \mathbf{a}, \mathbf{s}) = L. \quad (\text{B.4})$$

Here $L = 1$ for $y = r$ and $L = 1/2$ for $y = z$. That is to say, the intervals $[0, y_1)$, $[y_1, y_2)$, $[y_2, y_3)$, $[y_3, L]$ correspond to the 4 phases in the physical domain $[0, L]$. Using the approximation (B.2), the constraints (B.4) can be approximated by

$$\begin{aligned} (a_0 + a_1)s_1 &= y_1, \\ a_1(s_2 - s_1) &= y_2 - y_1, \\ (a_1 + a_2)(s_3 - s_2) &= y_3 - y_2, \\ (a_1 + a_2 + a_3)(1 - s_3) &= L - y_3. \end{aligned}$$

This gives

$$\begin{aligned} a_1 &= \frac{y_2 - y_1}{s_2 - s_1}, \quad a_0 = \frac{y_1}{s_1} - \frac{y_2 - y_1}{s_2 - s_1} \\ a_2 &= \frac{y_3 - y_2}{s_3 - s_2} - \frac{y_2 - y_1}{s_2 - s_1}, \quad a_3 = \frac{L - y_3}{1 - s_3} - \frac{y_3 - y_2}{s_3 - s_2}. \end{aligned} \quad (\text{B.5})$$

In the case $s_1 = 0$, we will choose $y_1 = 0$ and $a_0 = 0$. Then we have

$$a_1 = \frac{y_2}{s_2}, \quad a_2 = \frac{y_3 - y_2}{s_3 - s_2} - \frac{y_2}{s_2}, \quad a_3 = \frac{L - y_3}{1 - s_3} - \frac{y_3 - y_2}{s_3 - s_2}. \quad (\text{B.6})$$

Since we want $p(s; \mathbf{a}, \mathbf{s})$ to be a density function, we need a_0, a_1, a_2, a_3 to be non-negative. This yields the constraints on y_1, y_2, y_3 :

$$0 \leq y_1 \leq y_2 \leq \frac{s_2}{s_1}y_1, \quad y_2 + \frac{s_3 - s_2}{s_2 - s_1}(y_2 - y_1) \leq y_3 \leq \frac{s_3 - s_2}{1 - s_2}L + \frac{1 - s_3}{1 - s_2}y_2.$$

In our computation, since the blowup is focusing near the origin, the most interesting region is far away from the boundary L . Therefore, we always have $y_3 \ll L$, and we do not need to worry about the last constraint $y_3 \leq L(s_3 - s_2)/(1 - s_2) + y_2(1 - s_3)/(1 - s_2)$.

After a_0, a_1, a_2 and a_3 have been computed, we then construct the mapping density $p(s; \mathbf{a}, \mathbf{s})$ using (B.1) and the mapping function $P(x; \mathbf{a}, \mathbf{s})$ using (B.3). However, since the approximation (B.2) is not exact, the right boundary condition of $P(x; \mathbf{a}, \mathbf{s})$ is only approximately satisfied: $P(1; \mathbf{a}, \mathbf{s}) \approx L$. To make sure that $P(1) = L$ exactly, we need to rescale $p(s; \mathbf{a}, \mathbf{s})$ by a factor $L/P(1; \mathbf{a}, \mathbf{s}) \approx 1$, i.e.

$$\tilde{a}_i = \frac{L}{P(1; \mathbf{a}, \mathbf{s})} a_i, \quad i = 0, 1, 2, 3,$$

and then use $p(s; \tilde{\mathbf{a}}, \mathbf{s})$ and $P(x; \tilde{\mathbf{a}}, \mathbf{s})$ in the real computation.

Next, we explain how to choose y_1, y_2, y_3 for r_ρ and z_η . Again, let (R, Z) denote the maximum location of the reference solution $u_1(r, z)$. This coordinate locates the most singular part of the solution. We first consider r_ρ , i.e. $y = r$. Since we want the most singular part of the solution to be covered in phase 1, we should choose r_1, r_2 such that $[r_1, r_2]$ is a local neighborhood of the smaller scale around $R(t)$. In particular, we choose

$$r_2 = R + 3d_r, \quad r_1 = \max \left\{ R_r - 4d_r, \frac{s_1^\rho}{s_2^\rho} r_2 \right\},$$

where $d_r = R(t) - R_r(t)$ is the feature size of the smaller scale, and

$$R_r = \arg \max_{0 \leq r \leq 1} u_{1,r}(r, Z, t)$$

is the point where the r derivative $u_{1,r}$ achieves its maximum on the cross section $\{(r, Z) : 0 \leq r \leq 1\}$. Moreover, we impose the constraint that the outer part of solution of the larger scale does not go beyond phase 2. Note that the larger scale of the solution is characterized by the coordinate R , and the tail part of the solution mainly lies in $[0, 3R]$. Therefore, we choose

$$r_3 = \max \left\{ 3R, r_2 + \frac{s_3^\rho - s_2^\rho}{s_2^\rho - s_1^\rho} (r_2 - r_1) \right\}.$$

In the z direction, the smaller scale is characterized by Z . Then in order for the most singular region of the smaller scale to be covered in phase 1, we choose $z_1 = 3Z/2$. We have observed that the outer part of the solution in the z direction mainly lie in the range $[0, 10Z]$. Therefore, for the outer part to be covered in phase 2, we choose $z_2 = 15Z$. This completes the construction of the mapping functions $r(\rho)$ and $z(\eta)$.

REFERENCES

- [BHP16] M. Brenner, S. Hormoz, and A. Pumir. Potential singularity mechanism for the Euler equations. *Phys. Rev. Fluids*, 1:084503, 2016.
- [BKM84] J. Beale, T. Kato, and A. Majda. Remarks on the breakdown of smooth solutions for the 3-D Euler equations. *Commun. Math. Phys.*, 94(1):61–66, 1984.
- [BP94] O. N. Boratav and R. B. Pelz. Direct numerical simulation of transition to turbulence from a high-symmetry initial condition. *Phys. Fluids*, 6:2757–2784, 1994.
- [CFM96] P. Constantin, C. Fefferman, and A. Majda. Geometric constraints on potentially singular solutions for the 3-D Euler equations. *Commun. PDEs*, 21:559–571, 1996.
- [CH19] J. Chen and T. Y. Hou. Finite time blowup of 2D Boussinesq and 3D Euler equations with $C^{1,\alpha}$ velocity and boundary. *arXiv:1910.00173*, 2019.
- [CHH19] J. Chen, T. Y. Hou, and D. Huang. On the finite time blowup of the De Gregorio model for the 3D Euler equation. *To appear in CPAM*, *arXiv:1905.06387*, 2019.
- [CHK⁺17] K. Choi, T. Y. Hou, A. Kiselev, G. Luo, V. Sverak, and Y. Yao. On the finite-time blowup of a 1D model for the 3D axisymmetric Euler equations. *CPAM*, 70(11):2218–2243, 2017.
- [CKN82] L. Caffarelli, R. Kohn, and L. Nirenberg. Partial regularity of suitable weak solutions of the Navier–Stokes equations. *CPAM*, 35(6):771–831, 1982.
- [CSTY09] C. Chen, R. Strain, T. Tsai, and H. Yau. Lower bounds on the blow-up rate of the axisymmetric Navier–Stokes equations ii. *Commun. PDEs*, 34(3):203–232, 2009.
- [CSYTo8] C. Chen, R. Strain, H. Yau, and T. Tsai. Lower bound on the blow-up rate of the axisymmetric Navier–Stokes equations. *International Mathematics Research Notices*, 2008:rnn016, 2008.
- [DHY05] J. Deng, T. Y. Hou, and X. Yu. Geometric properties and non-blowup of 3D incompressible Euler flow. *Commun. PDEs*, 30:225–243, 2005.
- [EGM19] T. Elgindi, T. Ghoul, and N. Masmoudi. Stable self-similar blowup for a family of nonlocal transport equations. *arXiv:1906.05811*, 2019.
- [Elg19] T. M. Elgindi. Finite-time singularity formation for $C^{1,\alpha}$ solutions to the incompressible Euler equations on \mathbb{R}^3 . *arXiv:1904.04795*, 2019.
- [ES94] W. E and C.-W. Shu. Small-scale structures in Boussinesq convection. *Phys. Fluids*, 6:49–58, 1994.
- [Fef06] C. Fefferman. Existence and smoothness of the Navier–Stokes equation. *The millennium prize problems*, pages 57–67, 2006.
- [Gib08] J. Gibbon. The three-dimensional Euler equations: Where do we stand? *Physica D*, 237:1894–1904, 2008.
- [GKO95] B. Gustafsson, H.-O. Kreiss, and J. Oliger. *Time dependent problems and difference methods*, volume 24. John Wiley & Sons, 1995.

- [GS91] R. Grauer and T. C. Sideris. Numerical computation of 3D incompressible ideal fluids with swirl. *Phys. Rev. Lett.*, 67:3511–3514, 1991.
- [HLo6] T. Y. Hou and R. Li. Dynamic depletion of vortex stretching and non-blowup of the 3-D incompressible Euler equations. *J. Nonlinear Sci.*, 16:639–664, 2006.
- [HLo8a] T. Y. Hou and C. Li. Dynamic stability of the three-dimensional axisymmetric Navier–Stokes equations with swirl. *CPAM*, 61(5):661–697, 2008.
- [HLo8b] T. Y. Hou and R. Li. Blowup or no blowup? the interplay between theory and numerics. *Physica D.*, 237:1937–1944, 2008.
- [HLo9] T. Y. Hou and Z. Lei. On the stabilizing effect of convection in three-dimensional incompressible flows. *CPAM*, 62(4):501–564, 2009.
- [Hölo3] K. Höllig. *Finite element methods with B-splines*. SIAM, 2003.
- [Ker93] R. M. Kerr. Evidence for a singularity of the three-dimensional incompressible Euler equations. *Phys. Fluids A*, 5:1725–1746, 1993.
- [Kis18] A. Kiselev. Small scales and singularity formation in fluid dynamics. In *Proceedings of the International Congress of Mathematicians*, volume 3, 2018.
- [KNSSo9] G. Koch, N. Nadirashvili, G. Seregin, and V. Sverak. Liouville theorems for the Navier–Stokes equations and applications. *Acta Mathematica*, 203(1):83–105, 2009.
- [KRYZ16] A. Kiselev, L. Ryzhik, Y. Yao, and A. Zlatos. Finite time singularity for the modified SQG patch equation. *Ann. Math.*, 184:909–948, 2016.
- [KS14] A. Kiselev and V. Sverak. Small scale creation for solutions of the incompressible two dimensional Euler equation. *Annals of Mathematics*, 180:1205–1220, 2014.
- [LH14a] G. Luo and T. Y. Hou. Potentially singular solutions of the 3D axisymmetric Euler equations. *Proceedings of the National Academy of Sciences*, 111(36):12968–12973, 2014.
- [LH14b] G. Luo and T. Y. Hou. Toward the finite-time blowup of the 3D axisymmetric Euler equations: a numerical investigation. *Multiscale Modeling & Simulation*, 12(4):1722–1776, 2014.
- [Lin98] F. Lin. A new proof of the Caffarelli–Kohn–Nirenberg theorem. *CPAM*, 51(3):241–257, 1998.
- [LWo6] J. Liu and W. Wang. Convergence analysis of the energy and helicity preserving scheme for axisymmetric flows. *SINUM*, 44(6):2456–2480, 2006.
- [LZ17] Z. Lei and Q. Zhang. Criticality of the axially symmetric Navier–Stokes equations. *Pacific Journal of Mathematics*, 289(1):169–187, 2017.
- [MBo2] A. Majda and A. Bertozzi. *Vorticity and incompressible flow*, volume 27. Cambridge University Press, 2002.
- [PS92] A. Pumir and E. D. Siggia. Development of singular solutions to the axisymmetric Euler equations. *Phys. Fluids A*, 4:1472–1491, 1992.
- [Tao16] T. Tao. Finite time blowup for an averaged three-dimensional Navier–Stokes equation. *J. Amer. Math. Soc.*, 29:601–674, 2016.